ERNEST ORLANDO LAWRENCE BERKELEY NATIONAL LABORATORY
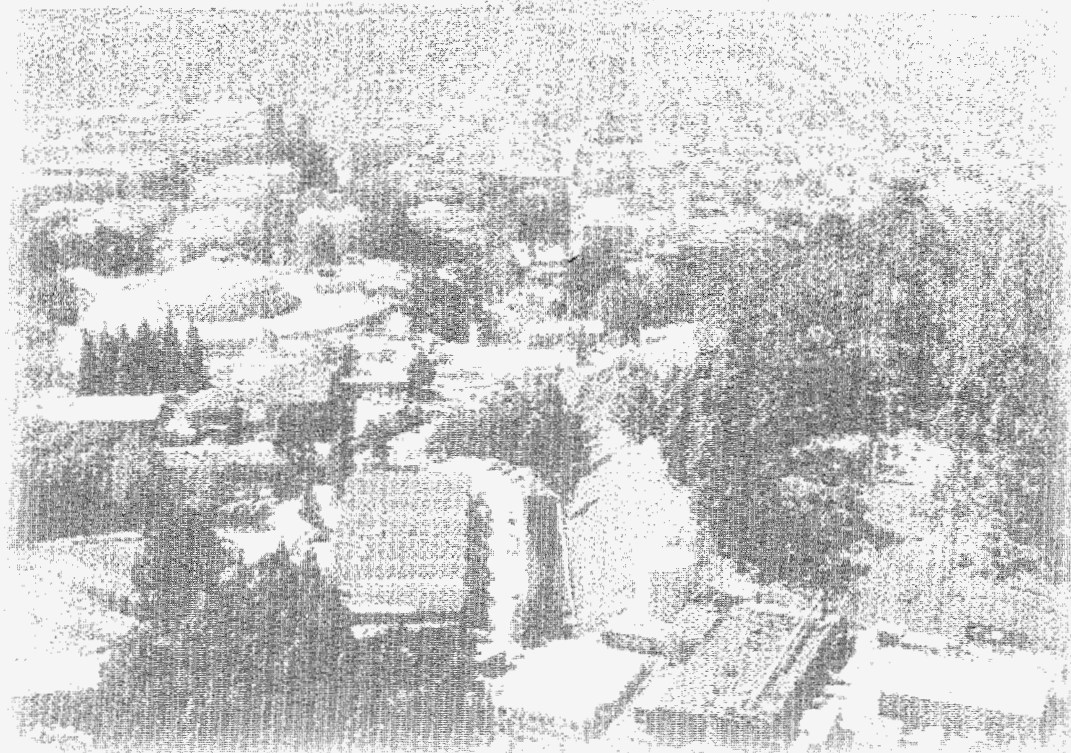
BERKELEY LAB

Processes Controlling the Migration and Biodegradation of Non-aqueous Phase Liquids (NAPLs) within Fractured Rocks in the Vadose Zone FY96 Annual Report

RECEIVED
JUN 12 1997
OSTI

Jil T. Geller, Grace Su, Hoi-Ying Holman, Mark Conrad, Karsten Pruess, and Jennie C. Hunter-Cevera
Earth Sciences Division

MASTER

February 1997

DISCLAIMER

Processes Controlling the Migration and Biodegradation of

Non-aqueous Phase Liquids (NAPLs) within Fractured Rocks in the Vadose Zone

FY96 Annual Report

Jil T. Geller[1], Grace Su[2], Hoi-Ying Holman[1], Mark Conrad[1], Karsten Pruess[1] and Jennie C. Hunter-Cevera[1]

1. Earth Sciences Division, E. O. Lawrence Berkeley National Laboratory
2. Department of Civil Engineering, University of California at Berkeley

February 1997

Table of Contents

Table of Contents

1. Executive Summary

Background

Subsurface contamination from volatile organic compounds (VOCs) has been found at many DOE, DoD and industrial sites due to the widespread use of organic solvents and hydrocarbon fuels. At ambient pressures and temperatures in the shallow subsurface, these substances are liquids that are immiscible with water; hence they are commonly designated as non-aqueous phase liquids (NAPLs). At some DOE sites, NAPLs are the presumed source of groundwater contamination in fractured rocks, such as basalts (at Hanford and INEL), shales (Oak Ridge Y-12 Plant), and welded tuffs (LANL).

The flow, transport and biodegradation processes controlling NAPL behavior in the vadose zone must be understood in order to establish the extent of contamination, the risk to groundwater supplies and appropriate remediation action. This is particularly important in arid sites with deep water tables (such as at Hanford, INEL and LANL). In fractured rock aquifers, NAPL migration is likely to be dominated by the highly permeable pathways provided by rock fractures and joints. Two- and three- phase fluid mixtures may be present in vadose zone fractures, including NAPL-gas, NAPL-water (in regions of perched water) and NAPL-water-gas. Fluid flow and distribution may be significant factors in the ability of microorganisms to degrade NAPL contaminants, as they affect the availability of substrate, moisture and nutrients. Biological activity can produce changes in liquid surface tensions and generate biofilms that may change the wettability of surfaces, locally altering fracture permeability and redirecting infiltrating liquids.

Focus of current project

To address the strong coupling between fluid distribution and the potential for biodegradation, this project investigates both flow dynamics and microbial processes affecting NAPLs in fractured rock in a closely coupled, integrated manner. Our objective is to develop a qualitative and quantitative understanding of the behavior of two and three immiscible fluid phases, microbial transformation and/or degradation of NAPL contaminants, and to provide a scientific basis for field investigations, site characterization, and remedial action for NAPL contamination in fractured rocks. To achieve this, our program combines laboratory and theoretical investigations, coupled with the evaluation of conditions at relevant field sites.

1. Executive Summary

Since inception of the project in April 1996, through the end of FY96, our activities have built a strong foundation for this research. We have conducted site visits and collected available reports from INEL to establish the essential field context for our experimental and theoretical investigations. At INEL's Surface Disposal Site, an estimated 88,000 gallons of carbon tetrachloride, TCE, TCA and PCE leaked from buried trenches into the vadose zone. The geology is fractured basalt with sedimentary interbeds, and perched water. The site is currently undergoing vacuum vapor extraction to prevent the migration of VOCs to the groundwater table. VOC concentrations have been observed to rebound after cessation of vacuum, which strongly suggests the presence of NAPL (as opposed to just vapor or aqueous phase VOCs). The detection of chloroform indicates that there may be significant biological activity.

Sample Acquisition Activities

We participated in ongoing drilling operations at the Test Area North (TAN) site at INEL, funded by the Subsurface Sciences Program, to obtain both defensible samples for microbiological work and samples for abiotic flow dynamics studies from just above the water table. We also obtained fractured rock samples for abiotic flow dynamics studies from the USGS core library at the INEL and an outcrop sample from Box Canyon, a clean site .

Flow Dynamics Accomplishments

Flow visualization experiments of water seepage in a transparent replica of a granite fracture were conducted for a range of angles of inclination and inlet pressures. We produced an LBL report describing these experiments in detail (Geller et al., 1996). Under all conditions, water flowed in one or two narrow channels that underwent cycles of snapping and reforming, despite the constant pressure maintained at the inlet. Seepage patterns were consistent with the aperture distribution measured from light transmission through the replica. Water spread transverse to flow direction in the tightest aperture regions, while narrow channels formed in the larger aperture regions. Also conducted was a preliminary seepage experiment in a rock-replica combination. By fabricating an epoxy cast of one side of a vesicular basalt fracture from the USGS core library and mating it with the actual rock of the other side, it was observed that the degree of matrix flow in the rock-half was sensitive to the angle of fracture inclination and the presence or absence of no-flow boundaries on the rock surfaces.

1. Executive Summary

A detailed study of water seepage in parallel glass plates revealed that an aperture sequence of medium to large to fine openings produced the same cyclic behavior of thread snapping and reforming as in the fracture replicas. We also found that the mode of snapping depends upon the flow rate to the plates and their angle of inclination. For very low flow rates, water drips, as opposed to continuous threads, formed and snapped, in a manner analogous to the dripping faucet (i.e. independent of downstream conditions). At somewhat higher flow rates, cycles of continuous thread formation, flow and snapping were observed. Above a threshold flow rate, no snapping occurred. We derived discrete flow rates in and out of a region of the glass plates from image analysis, and found evidence that snapping of liquid threads may be controlled by changing liquid saturation above and below the section of thread.

Preliminary experiments of NAPL flow and trapping in the same fracture replica used for water seepage experiments were conducted. The NAPL was introduced into the fracture containing residual water. A low volatility LNAPL (n-dodecane) and a high volatility DNAPL (Freon 113) were used in separate experiments. The NAPL flowed both through the dry portions of the fracture, getting trapped in the tight apertures as was the case for water, as well as along the water-air surfaces, where it was also trapped. When the NAPL encountered a small segment of residual water, it flowed around the water-air-solid contact, thereby "wrapping" itself around the water. This behavior is driven by the zero contact angle of the NAPL on the solid relative to air and not by the tendency, or lack of, to spontaneously spread along the air-water surface. The Freon 113 rapidly volatilized after entering the fracture; sealing the sides of the fracture did not reduce the volatilization rate, indicating significant air flow through the top and bottom of the fracture. These experiments illustrated the variety of phase interfaces (liquid/liquid, liquid/vapor, liquid/solid and solid vapor) and their complexity, occurring in two and three fluid phase systems.

Multi-phase flow simulations of water seepage in unsaturated fractures were performed to (a) examine whether standard macro-scale continuum concepts can describe the behavior and (b) investigate space-and-time scaling relationships which may aid in relating laboratory and field scale phenomena. An LBNL report of this work was published (Pruess, 1996a). A single fracture plane was modeled as a two-dimensional heterogeneous porous medium, with a stochastically-generated aperture distribution

1. Executive Summary

designed to capture essential features of the fracture plane geometry. The TOUGH2 simulator was used with the EOS9 fluid property module to implement Richards' equation for saturated-unsaturated flow. The simulated seepage patterns reproduced many of the features observed in the laboratory flow visualization experiments, such as flow fingering, bypassing and ponding, with the exception of cyclic flow intermittence. An approximate invariance of seepage under simultaneous space-and-time scaling was theoretically derived, where the vertical length scale and the time scale are equal to the square of the horizontal length scale. This invariance was tested with numerical simulations and was validated for upscaling by a horizontal scale factor of 5. Theoretical analysis showed that scaling invariance would break down at a sufficiently small scale; this was confirmed by numerical simulation results.

Microbiological Accomplishments

Biotransformation studies focused on developing microbial ecology sampling techniques, designing the geocosm for natural fractured- rock samples, and measurement of isotope ratios of compounds to be used both in abiotic flow dynamics experiments and in the geocosm. Culturing techniques were modified to measure the distribution of organisms on the rock fracture surfaces by imprinting onto agar discs. A washing-off technique was used to sample the microorganisms from the inner pore-spaces of the same sample that are inaccessible to the agar imprints. These techniques were tested on available vesicular and dense basalt samples from the USGS core library at INEL. Despite the fact that these samples were not obtained or preserved in a manner that would maintain their biological integrity, they were useful for methods development in that they represented the character of defensible samples that we expected to receive from coring operations by R. Colwell at INEL. A comparison of microbial distributions between the vesicular and dense basalt revealed that the pits and pores of the vesicular basalt fracture surface provide vastly different environments for microorganisms compared to the comparatively smoother dense basalt fractures. Microorganisms were cultured from sedimentary interbeds from the SDA site. Again, these samples were not obtained with methodology for defensible microbiological work, however they revealed some characteristics distinct from the basalt rock samples.

Moisture stimulation experiments were initiated by using thin sections of dense and vesicular basalt to determine whether the growth of micro-organisms is sensitive to

1. Executive Summary

changes in relative humidity. The results of these experiments will determine the vapor phase conditions to be used in the geocosm. A flexible wall permeameter was modified to hold the geocosm. This will prevent fast path fluid flow along the column walls and control the loading of the fracture halves.

The isotopic ratios of contaminants and metabolic byproducts of their degradation will be measured in the geocosm to develop this technique for field monitoring of biological processes. Analytical methods were developed and employed to determine the isotopic ratios of organic liquids that will be used in either the geocosm or in the flow dynamics experiments, specifically toluene, iso-octane, n-dodecane, carbon tetratchloride and perchloroethene. The chlorinated compounds had significantly lower $\delta^{13}C$ than the hydrocarbon compounds. We are also interested in determining the fractionating effects of physical processes on the isotopic ratios of NAPL contaminants at ambient temperatures, such as vaporization and dissolution into water, on the isotope ratios of the organic compounds. Our preliminary experiments with toluene suggest that the large shifts towards higher $\delta^{13}C$ measured at extreme temperatures do not occur at moderate temperatures.

Plans for FY97

In FY97 we will focus our efforts on integrating the flow dynamics and biological transformation studies. An "open" geocosm will serve as our integration platform, where we will directly observe flow and potentially biomass growth on an open fracture surface exposed to trickling liquids (water and NAPL). More detailed studies will continue of flow dynamics in single fractures with replicas and rocks. We will pursue opportunities to obtain larger fracture samples for seepage studies from INEL. Biotransformation processes and monitoring techniques will be studied in geocosms in the defensible samples obtained in October of 1996. Theoretical studies will aim at developing conceptual and mathematical models for multiphase fluid behavior in fractured rock. Laboratory-scale investigations will be developed to simulate and relate to actual field problems. We will continue to obtain information on VOC-contaminated fractured vadose zone sites. Additionally, all of the researchers in this project participate in other projects with field activities, which reveal the multitude of characterization, monitoring and remediation challenges of understanding flow and contaminant fate in the shallow subsurface.

2. Introduction

Subsurface contamination from volatile organic compounds (VOCs), such as organic solvents or hydrocarbon fuels, is a common occurrence at many DOE, DoD, and industrial sites throughout the U.S. Under ambient conditions of pressure and temperature, these substances are liquids that are immiscible with water; hence they are commonly designated as "non-aqueous phase liquids" (NAPLs). At some DOE sites, NAPLs are the presumed source of groundwater contamination in fractured rocks, such as basalts (at Hanford and INEL), shales (Oak Ridge Y-12 Plant), and welded tuffs (LANL).

When NAPLs are introduced into fractured rock, their migration is likely to be dominated by the highly permeable pathways provided by rock fractures and joints. From the fluid dynamics standpoint, the presence of NAPLs in the vadose zone will give rise to three-phase flow of water, (soil) gas, and NAPL. In arid environments, very little water may be present in fractures, so that the flow problem simplifies into two-phase flow of NAPL and gas. In regions of perched water, or beneath the water table, there is two-phase flow of NAPL and water. The different fluid phases - aqueous, gaseous, and NAPL - will flow under the combined action of gravity, capillary, and pressure forces. Commonly encountered NAPL contaminants, such as organic solvents and hydrocarbon fuels, tend to be volatile as well as having a (generally) small solubility in the aqueous phase. Thus, upon descending in partially saturated fractures, NAPL plumes partially vaporize, and partially dissolve as they contact ambient or percolating groundwater. A general discussion of physical proesses during NAPL migration in subsurface environments is given by Pruess (1992).

Complex as the fluid dynamics problem is, it is insufficient to provide an understanding of the behavior of NAPLs in natural environments. The existence of microorganisms in the subsurface has been noted for decades, and viable microorganisms were isolated at depths as great as several thousand meters below the surface in broadly variable physical and chemical settings (Pedersen, 1993; Herrick et al., 1993). Fractured rock systems, however, have long been considered to be an unfavorable condition for intrinsic bioremediation of organic contaminants (Vogel, 1994). Little is known about the microbial communities of deep subsurface environments (Amy et al., 1993), and understanding of microbial transport, fate, physiology, and community dynamics is still very sketchy. New exciting developments in biofilm research have brought additional

2. Introduction

revelations about structure and function of microbial micro-colonies and how they regulate their effective contact with the fluid phases (Costerton, 1995).

This project investigates both flow dynamics and microbial processes affecting NAPLs in fractured rock in a closely coupled, integrated manner. Our objective is to develop a qualitative and quantitative understanding of the behavior of two and three immiscible fluid phases, microbial transformation and/or degradation, and to provide a scientific basis for field investigations, site characterization, and remedial action for NAPL contamination in fractured rocks. To achieve this, our program combines laboratory and theoretical investigations, coupled with the evaluation of conditions at relevant field sites. This report summarizes the work accomplished since inception of the project in April 1996.

3. Summary of FY96 milestones

This project is divided into the following tasks:

1. **Phenomenological studies** to explore and visualize two- and three-phase flow and microbial activity in natural rock fractures, and in transparent replicas of natural fractures.

2. **Measurement of two- and three-phase flow in fractures** to quantify the relationships between rock and fluid properties that determine (a) the spatial and temporal distribution of immiscible infiltrating liquids in fractures, and (b) the hydrogeochemical environment for microbial activity.

3. **Biotransformation of volatile NAPL organic contaminants** to measure the extent of biotransformation and/or degradation occurring in NAPL-contaminated fractured rock and assess monitoring tools.

4. **Theoretical analysis** to develop and test modeling paradigms that encompass the physical, chemical and biological processes relevant to the fate of NAPLs in fractures.

Following is the list of FY96 milestones outlined in our proposal, annotated with a brief description of accomplishments during the term of this report. More detailed descriptions are provided in the referenced sections.

- *Task 1.1: Phenomenological flow studies in abiotic systems (Section 6)*

  Water seepage patterns in an initially dry fracture replica show strong correspondence to the measured aperture distribution. NAPL infiltration into a partially saturated fracture replica resulted in significant NAPL trapping around water-saturated regions and regions of greater surface roughness. Controlling factors in time-varying (intermittent) flow behavior were studied in a detailed examination of liquid thread snap-off and reformation in a medium-coarse-fine aperture sequence.

- *Task 2: Acquisition of samples (Section 5)*

  The major effort this year was to obtain samples for the geocosm experiments, due to the longer time required for the biodegradation studies compared to the flow dynamics studies. "Defensible" (controlled) core samples of intact and fractured basalt were acquired from the TAN site at INEL. Additional samples for preliminary studies and methods development include drilling chips from the SDA and cores from the SDA and Box Canyon which were obtained through the USGS core library at the INEL.

3. Task descriptions and milestone summary

- *Task 3.1 Design and construction of the geocosm (Section 8.4)*
  A flexible wall permeameter has been modified to perform as a geocosm and is currently under testing.

- *Task 3.2 Biotransformation of volatile organic contaminants (VOC's) in fractured rock (Sections 8.1-8.4)*
  Preliminary samples were used to test modifications of microbial ecology techniques to study microorganisms inside fracture basalt and sedimentary interbeds. Agar discs imprinted by thin sections of dense and vesicular basalt produced distinctly different colonies.

- *Task 3.3 Determination of the isotopic ratios of all potential substrates (Section 8.5)*
  The isotopic ratios of toluene, iso-octane, n-dodecane, carbon tetrachloride and perchloroethylene were determined in preparation for monitoring biological degradation of the NAPLs in the geocosm. Additional tests to determine the effects of physical processes in the isotope ratios (vaporization, dissolution into water) are in progress.

- *Task 4: Theoretical analysis (Section 7) and detailed evaluation of field data (Section 4)*
  Water seepage in heterogeneous fractures was studied by means of numerical simulation. High-resolution simulations of spatially correlated heterogeneity produced similar seepage features as were seen in the laboratory experiments, including flow fingering, bypassing and ponding. Site visits to the INEL and discussions with LANL provided a general description of the field conditions, and available data where NAPL contamination occurred in fractured rock.

4

4. Evaluation of field cases

(J. T. Geller, lead author)

4.1 Sites at the Idaho National Engineering Laboratory (INEL)

4.1.1 General Geological Features

This discussion is limited to a simplified description of the basalt flows of the Eastern Snake River Plain (ESRP) and their features which have implications for local fluid migration and contaminant transport, mostly extracted from Sorenson et al. (1996). Knutson et al. (1990) define four layered elements of a typical basalt flow, from bottom to top: (1) a substratum; (2) a lower vesicular element; (3) a coarse-grained, massive, generally nonvesicular central element; and (4) an upper vesicular element. The substratum generally accounts for about 5% of the flow thickness and may consist of a ropey pahoehoe surface, fractured and fissued surfaces, and rubble zones. The lower vesicular element contributes about 11% of the total flow thickness, generally fractured into polygons. The massive central element comprises about 49% of the thickness, generally quite dense with few fractures except for vertical columnar joints. Lava tubes and collapsed lava tubes, although very rare, can be found in the central element. Finally, the upper vesicular element typically accounts for about 35% of the total flow thickness. This element may have a parting parallel to the upper surface as well as fissures and broken basalt most likely due to the viscous drag of the interior mobile lava beneath the cooled crust as well as the stresses caused by elongation when the crust falls into collapsed areas. The broken basalt may contribute to rubble zones in the substratum of the overlying flow. In general, basalt flows in the ESRP can be thought of as lobes extending out from the source vent, overlapping and building on the undulating topography of previous flows. A 1,000 ft long lobe may have an average width ranging from 100 to 400 ft while the average thickness might range from 10 to 30 ft. Sedimentary interbeds of clay, silt, sand and gravel may occur between the basalt flows, formed during periods of quiescence.

A preliminary description of the geology of the Box Canyon site (Long et al., 1995) notes the presence of vesicular lenses from 1 to 20 cm thick below the upper vesicular zone. Many of the lenses support horizontal fractures and large voids. The detailed site

5

4. Evaluation of field cases

investigation by Long et al., including core and well logs and interpretation from a cliff exposure, illustrates the complexity of the fracture distribution and the range of fracture types that may be expected, and particularly the difficulty in characterizing the extent and continuity of fractures.

4.1.2 Surface Disposal Area of the Radioactive Waste Management Complex

The "Organic Chemicals in the Vadose Zone" (OCVZ) project at the Surface Disposal Area (SDA) of the Radioactive Waste Management Complex (RWMC) is an active vacuum vapor extraction (VVE) operation underlying a historic solvent disposal area. This is an 88 acre landfill area with 33 trenches and 19 pits that began operation in 1952. In parts of this area, barrels were dumped into trenches and buried. The barrels contained volatile organic chemicals (VOCs) including carbon tetrachloride (CCl_4), tri-chloroethene (TCE), tri-chloroethane (TCA) and perchloroethene (PCE), along with some mixed waste,perhaps biological contaminants, nitrates and metals. As is typical for these kinds of sites, the source term is not well known, but the total volume is estimated to be 88,000 gallons. The top 30 feet is soil, underlain by basalt down to 110 feet, then a sedimentary interbed, then more fractured basalt, another sedimentary interbed at 240 feet overlying fractured basalt which continues through the groundwater table at 585 feet below the surface. The sedimentary interbeds range from 0 to 30 feet thick. Their descriptions in the core logs from the vapor monitoring wells in the SDA range from silty-clay, clayey-silt , sand, and coarse sand. Core logs indicate the presence of non-fractured and fractured basalt, and rubble zones. Some of the fractures are noted as sand-filled. Sequences of dense and vesicular basalt are also noted. This area has flooded three times since 1962. The Big Lost River, which only flows about every 10 years, is flowing through the area this year and did last year,which suggests more than average water seepage through the vadose zone.

Following the results of a treatability study (Lodman et al., 1994), the vapor extraction operation began in January 1996, and has extracted the equivalent of 11 barrels of VOCs. The treatability study located the zone for VVE near the 110 foot interbed, which had the highest measured permeability, vacuum extraction rates and VOC concentrations. Three vapor extraction wells intercept the 110 foot interbed. Data from

6

4. Evaluation of field cases

many monitoring wells with vapor sampling ports at multiple levels, and barometric pressure are also collected. The VOCs that are monitored are CCl_4, TCE, TCA, PCE and choroform ($CHCl_3$). The $CHCl_3$ is presumed to be a degradation product as it is not documented as being a waste source. The 110 foot interbed is hypothesized to be a barrier to downward VOC migration, however CCl_4 has been detected in the groundwater below the site (which may not necessarily be from the SDA). During extraction, VOC concentrations decrease in many (but not all) of the sampling ports, and after stopping extraction, VOC concentrations rebound in some of the sampling ports. They are currently running cycles of vapor extraction followed by quiescent periods to try to understand the source term and the controls on the rebounding of VOC concentrations. The VVE produces alot of water vapor along with the VOCs. The plots of barometric pressure vs time at various depths show three distinct patterns, each of which is exhibited by several sample ports. However, there is no clear relationship between the elevation of the sample port or borehole and the barometric pressure record.

This project is in the clean-up phase, however there is a need to understand the transport processes at this site in order to ensure that VOCs won't reach the groundwater aquifer. The presence or absence of NAPLs has not been confirmed. The rebound of VOC concentrations indicates that the source has not been removed and may be DNAPL. Perched water at the sedimentary interbeds may also promote DNAPL trapping and inhibit the rate of volatilization of the DNAPL.

4.1.3 Test Area North

The Test Area North (TAN) site is located approximately 50 km NNE from the RWMC. Except where noted, the following information is summarized from the 1995 Record of Decision for remediation of this site (Record of Decision, 1995). The principal source of groundwater contamination at TAN is the TSF-05 Injection Well, located within the Technical Support Facility (TSF). TSF-05 was used from 1953 to 1972 to dispose of TAN liquid wastes into the fractured basalt of the Snake River Plain Aquifer. After 1972, wastewater was disposed in the TAN disposal pond. These wastes included organic, inorganic and low-level radioactive wastewaters added to industrial and sanitary wastewater. Contaminants present at concentrations above risk-based levels in the groundwater are TCE, 1,2-dichloroethene (DCE), PCE, strontium-90, tritium, cesium-137

7

4. Evaluation of field cases

and uranium 234. Only TCE, DCE and tritium have been detected beyond the immediate vicinity of the Injection Well, or within the TSF-05 hotspot, defined by the 5 mg/L TCE isopleth. Estimates of the liquid volume of TCE disposed in the well during its period of operation range from 1325 to 97,161 L. Sludge removed from the bottom 17 m of the well in 1990 contained 2% TCE and radionuclides (note that the aqueous solubility of TCE is approximately 0.1%). The bulk of the TCE is hypothesized to be in the TSF-05 hotspot either entrained in the sludge, as water-sludge TCE emulsions and/or as NAPLs in dead-end fractures or on basalt flowtops. Figure 4.3.1 is reproduced from Sorenson et al. (1996) and shows TCE isopleths in cross-section in the direction of the groundwater gradient. The injection well extends to a depth of 310 ft below land surface (bls) and is perforated from 180 to 244 ft and from 269 to 305 ft bls, consequently there was some vadose zone contamination within the hot spot where the waste was injected slightly above the water table. The P-Q sedimentary interbed occurs at about 200 ft bls and is discontinuous. The Q-R interbed occurs at approximately 440 ft bls and is continuous. These interbeds consist of silt and clays and have low permeabilities. The approximately 12 m thick Q-R interbed appears to be a barrier to vertical contaminant transport. The depth the groundwater is about 206 ft bls. Water level elevations in a well located at the 1 ppm TCE isopleth (GS24 shown in gigure 4.1.1), downgradient from TSF-05, indicate annual fluctuations of about only 3 feet, but there has been a long-term decline of approximately 15 feet from 1985 through 1995 (Sorenson et al., 1996).

4.2 Los Alamos National Laboratory, Material Disposal Area L

(The information presented here for this site is based on private communications with Donathon J. Krier of the Earth and Environmental Sciences, Geology and Geochemistry Group of Los Alamos National Laboratory (LANL). A report written this summer for the EPA by LANL describing this site has been requested, but was not received at the time of this writing.) Material Disposal Area L (MDAL) was a liquid hazardous waste disposal site, located on top of a mesa, in the Bandalier tuff unit. The MDAL did not receive radioactive waste. The top layer is moderately welded, 40-50 ft thick, and is highly fractured as a result of cooling processes. An ash-flow tuff unit with extensive near-vertical fractures can be seen at the bottom of the disposal pits. The fractures are interconnected, with openings 1-5 mm wide near the surface that appear to close farther

8

4. Evaluation of field cases

down. Deeper down the fractures are filled with clay or pulverized, wind-blown tuff. Fractures die out in the next lower unit, which is a series of ash flows of friable, non-welded, highly porous tuff (porosity close to 50%) that does not support cooling fractures, with the exception of the upper part of this unit that was heated from above. Gas permeability measurements indicate 2-10 darcy permeability in the non-welded unit.

Thirty-two, six foot diameter waste disposal shafts penetrate the upper fractured unit into the non-welded unit to a depth of sixty feet. These shafts are filled with drums and capped. In the early 50's and 60's there was probably free liquid disposal. More careful operations began in the mid-70's, where only barrels with adsorbant materials were disposed. In addition, there are four pits, one of which was a free liquid disposal pit for waste evaporation; the three others are surface impoundments. The largest contaminant source term is presumed to be from the liquid disposal pit. The disposal shafts are expected to continue to release contamination from shafts as barrels rupture. Currently, the entire area is covered over, with current waste-handling operations conducted on the surface.

The gas-phase contaminant plume is approximately 1000 ft long by 200-300 ft wide, extending the width of mesa. The highest gas concentrations of 1000 ppmv TCA and TCE have been measured at 120 ft depth, and decrease at larger depths. Site sampling has not revealed any NAPL, or staining of rock by solvents. Fifty foot-long monitoring wells have been drilled at a 30° angle off the vertical, extending under the disposal pits. These wells are entirely within the upper unit. GCMS analysis of pore-gas sampled during the drilling detected 15 to 16 analytes, including Freon 11, Freon 113, and PCE. The relative humidity of the gas phase is 100%. The water table elevation is 960 ft below surface. The volumetric moisture content ranges from 1-8%, measured gravimetrically, with occasional spikes of 20%. A total of 18 boreholes in addition to the monitoring wells have been drilled and produced 800 samples. They have attempted to locate gas sampling probes near fractures, but most of sampling is within the rock matrix. The core samples are very clean, with little contaminant sorption. Other holes, extending to a depth of 300 ft, penetrate the contact between volcanic tuff and underlying basalt flows which are highly fractured. They are beginning to drill into the basalt flow below MDAL and have detected 2 to 3 analytes at 10 ppmv or less (TCA, PCA), but no free product. The only radionuclide

4. Evaluation of field cases

detected is tritium, at 11 pCi/L. Some effort has been made to look for biological activity, suggested by the occurrence of large CO_2 contents, on the order of 40,000-50,000 ppm.

Currently, this site is in a monitoring phase with no remedial action required, due to the fact that the contaminant plume has not reached the groundwater table. If remedial action is required, they will consider barometric pumping as a passive remediation technique. The basalt appears well-connected to atmosphere, via basalt outcrops. This feature may help keep VOCs from getting to water table, and volatize any NAPL that may have penetrated that deep.

4.3 Summary of transport issues in fractured rock as indicated by site evaluations

At the fractured rock vadose zone sites, NAPLs were the original contamination source. Source term volumes are unknown, as well as the extent of migration and phase transformation. As the NAPL itself is rarely directly encountered, its presence or absence cannot be established on the basis of site sampling. This is a key issue driving the need for a basic understanding of NAPL migration and transformation processes in fractured rock, to determine if and where there is NAPL, what remediation is required, and what will be the effect of the remediation activities.

The persistence of the VOC contamination in the vadose zone needs to be examined, including the conditions that determine the extent to which it can volatize, and the effect of liquid water and water vapor on NAPL migration and volatization. Although the vadose sites we have studied are arid, they are subjected to water-infiltration events, perched water occurs in locations of geologic discontinuities, and the relative humidity of extracted vapor from the vadose zone at the SDA is 100%.

The presence of $CHCl_3$ at INEL and of large CO_2 concentrations at LANL suggests naturally occurring biodegradation. A major issue is to identify where in the fracture systems the microbial activity occurs and what environmental factors, such as presence of water, mineralogy, surface roughness, are conducive to microbial growth. The matrix permeability of rocks at these sites varies greatly, such that a range from impermeable to permeable must be considered. Although vesicular basalt is often thought of has having large porosity of isolated vesicles, and therefore low permeability, this is not necessarily the case and its permeability can approach a Darcy. Micro-spheres have been observed to flow

4. Evaluation of field cases

through an intact sample of vesicular basalt, indicating well-connected porosity (R. Colwell, INEL, personal communication).

Data from vadose zone sites currently under remediation or monitoring should be analyzed in more detail for information regarding VOC transport and transformations. The rebound in VOC concentrations when active remediation is stopped may potentially reveal the nature of the contaminant source and its composition. The multi-component nature of most NAPL contaminants introduces additional complexity due to the range in vapor pressure and solubility of the individual components and consequently changing mass transfer rates of the NAPL components to the other fluid phases.

TCE (ppm)
Nov. - Dec. 1994
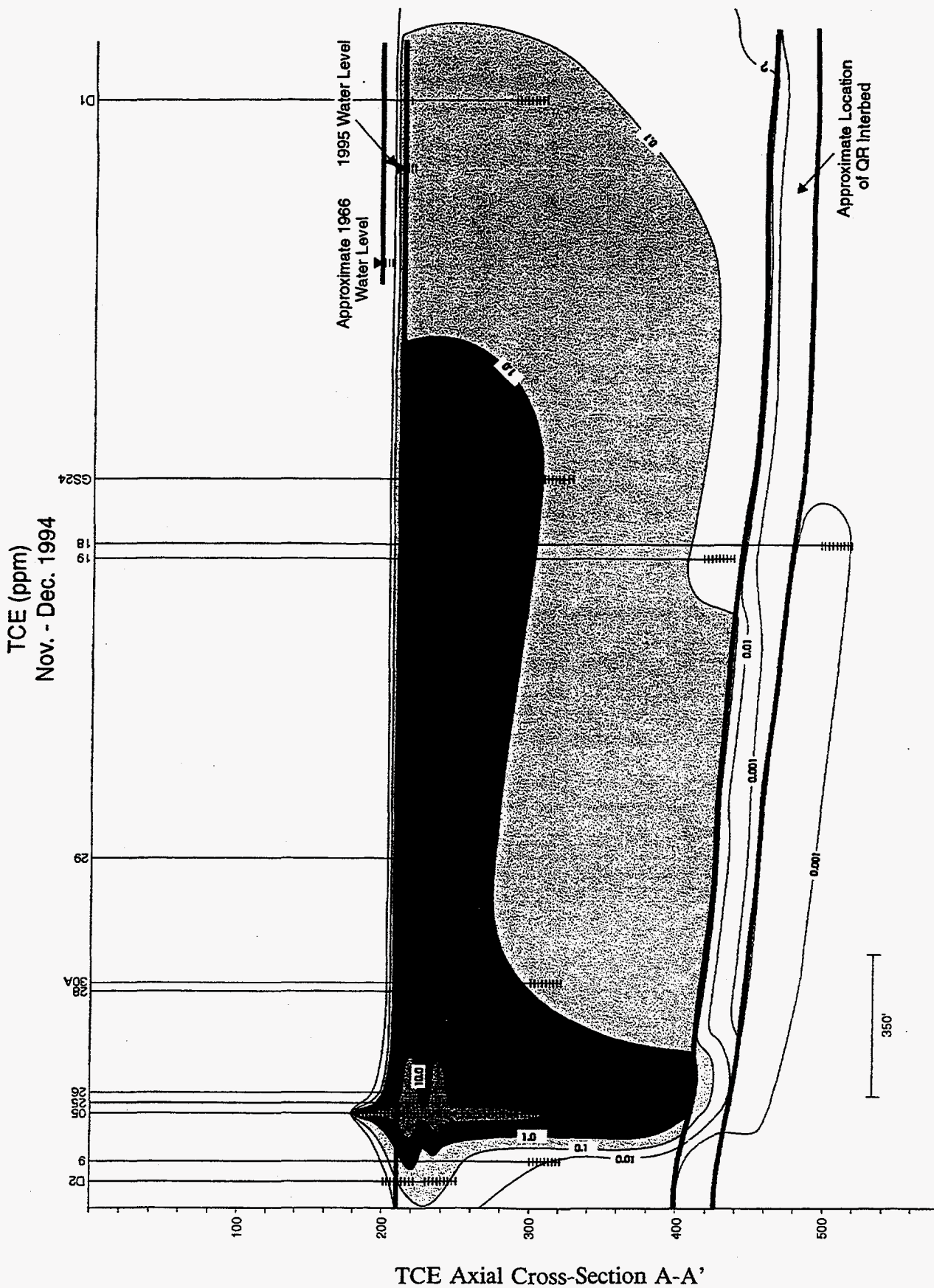
TCE Axial Cross-Section A-A'

Approximate 1966 Water Level

1995 Water Level

Approximate Location of QR Interbed

350'

TAN Hydro. Studies, OU 1-07B
INEL-96/0105

Revision 0
March 1996

Figure 4.1.1 TCE concentrations at the Test Area North site of the INEL (from Sorensen et al., 1996).

12

5. Sample acquisition

(J.T. Geller, lead author)

5.1 Samples for microbiological and geocosm work

FY96 sampling efforts focused on the early acquisition of samples for microbiological work, due to the longer time-frame for the geocosm experiments, as compared to the flow dynamics experiments. At the time of writing, we are obtaining "defensible subsurface materials" according to protocol developed by F. S. Colwell of INEL, within the framework of ongoing Subsurface Science Program coring operations at the Test Area North (TAN) site at the INEL. A 3.35" diameter borehole is being drilled near the 1 ppm TCE isopleth, down-gradient of the waste-injection well. LBNL issued a subcontract to the INEL to provide up to three feet of core selected from an interval beginning at the current water table elevation, extending ten feet above (at approximately 225 ft below ground level). Both fractured and intact core may be selected, depending upon what is encountered. Cores are drilled with cleaned equipment, filtered air and local groundwater for cooling. The air is spiked with a perfluorocarbon tracer to mark the extent of contamination of the core material by the drilling fluid and microspheres to simulate potential contamination by foreign micro-organisms. The groundwater is chlorinated to prevent the introduction of bacteria via the cooling water. The core barrel is opened in a glove box under an argon environment, and selected core is sealed in argon for shipment. Further details of the sampling can be found in the sample acquisition report in Appendix A.

It is important to note that only intact rock samples can be obtained without contamination by drilling fluid, because fractures will be exposed to the drilling fluid. Consequently, we expect that the microbial ecology will be assessed from the intact cores, and compared to the distributions found on fractured surfaces.

13

5. Sample acquisition

Contamination at TAN resulted from waste injection at and below the water table, so there was no direct NAPL contamination of the vadose zone beyond the hot spot area described in section 4.1.3. However, given the seasonal water table fluctuations, the time of sampling being near the end of the dry season, and the presence of aqueous phase TCE in the groundwater, it is likely that the rock samples obtained above the water table have been exposed to either vapor or aqueous phase TCE. This exposure may have allowed indigenous micro-organisms to acclimate to degrade TCE.

Vapor monitoring ports have been installed in the borehole at 200 ft below ground surface level, so that the actual levels of vadose zone contaminants very close to our sample location will be known.

Several samples were obtained for preliminary studies. Although these samples were not obtained aseptically, or preserved in any special manner after drilling, they were useful for the development of experimental protocol and design of the geocosm. Drilling chips from the SDA were obtained approximately one month after drilling, during which time they were stored in plastic bags. Two sections of 2" diameter cores from a vertical borehole (II-5) in Box Canyon were taken from the core library, approximately two months after drilling (see description in next section). During this time, the samples had been stored in core boxes without any precautions in terms of preserving their in-situ properties. These sections are approximately 8" long; one sample is a dense basalt from a depth of 28.7 feet below ground surface, with a fracture running parallel to the core axis, the second sample is a fractured vesicular basalt from a depth of 38.7 feet.

In FY97, more sampling opportunities will be pursued, such as possible core-drilling at the SDA.

5.2 Samples for flow dynamics

Fractured rock samples for the flow visualization and dynamics experiments must be relatively planar and have an areal extent of approximately 20 cm by 30 cm to allow the

5. Sample acquisition

formation and observation of seepage patterns away from the fracture boundaries, while being a manageable size and competence for casting and machining. Opportunities for obtaining such samples have been pursued at the INEL. For FY97, the most practical option is to obtain samples at Box Canyon, which is in a basalt flow similar to the INEL sites, but outside the boundaries of the INEL. This site is uncontaminated and large diameter (greater than 6") samples can be cored from the surface using local contractors at a much lower cost than working within the boundaries of the INEL. Additional advantages to obtaining samples from the Box Canyon site are the absence of sedimentary overburden, so that fracture traces can be seen at the surface, as well as the presence of ongoing field infiltration tests by researchers at the INEL and LBNL (e.g. Long et al., 1995), which provide a context for the laboratory investigations.

Two- and three-inch diameter core from many sites at the INEL can be obtained from the USGS core library. At the core library we inspected cores from Box Canyon and the SDA, and acquired a few samples of fractured basalt, both dense and vesicular. These samples represent endpoints for flow conditions in the basalt. The dense basalt matrix has sub-milli-Darcy permeability, while the vesicular basalt matrix can be up to three orders of magnitude more permeable (Boris Faybishenko, LBNL, personal communication). Another notable difference is in the topography of the fracture surface; the dense basalt exhibits a smooth surface, similar to the granite fracture samples we have on hand, while fractures in the vesicular basalt have extremely rough surfaces created by their intersection of spheroidal vesicles at various cords. These differences will have strong implications for liquid flow and trapping within the fractures. Figure 5.2.1 is a photograph of core from Box Canyon, borehole II-5, 28.7'-38.1', where 28.7' is the lower right hand side of the box. The left half and last section of the box are cut-off from view. The upper right hand side of the frame shows an abrupt transition between the dense and the vesicular basalt. The long fracture along the length of the core through the dense basalt appears smooth and continuous. These cores were drilled with water only, so the tan-colored coatings seen on the fracture surfaces may have been deposited from

15

5. Sample acquisition

sediments mobilized by the drilling water, or may be "native". The drilling log from this borehole notes the presence of light tan silt in fractures at other elevations. A full description of the core log and photos of core boxes from borehole II-5 can be found in Long et al. (1995). A fracture in an outcrop sample of vesicular basalt from Box Canyon, shown in Figure 5.2.4 shows the occurrence of vesicles in the fracture plane which create a much more complex geometry compared to the dense basalt fractures .

Core samples of 3.35" diameter with fractures in dense and vesicular basalt may also be obtained from ongoing drilling at the Test Area North (TAN) site, described in the previous section.
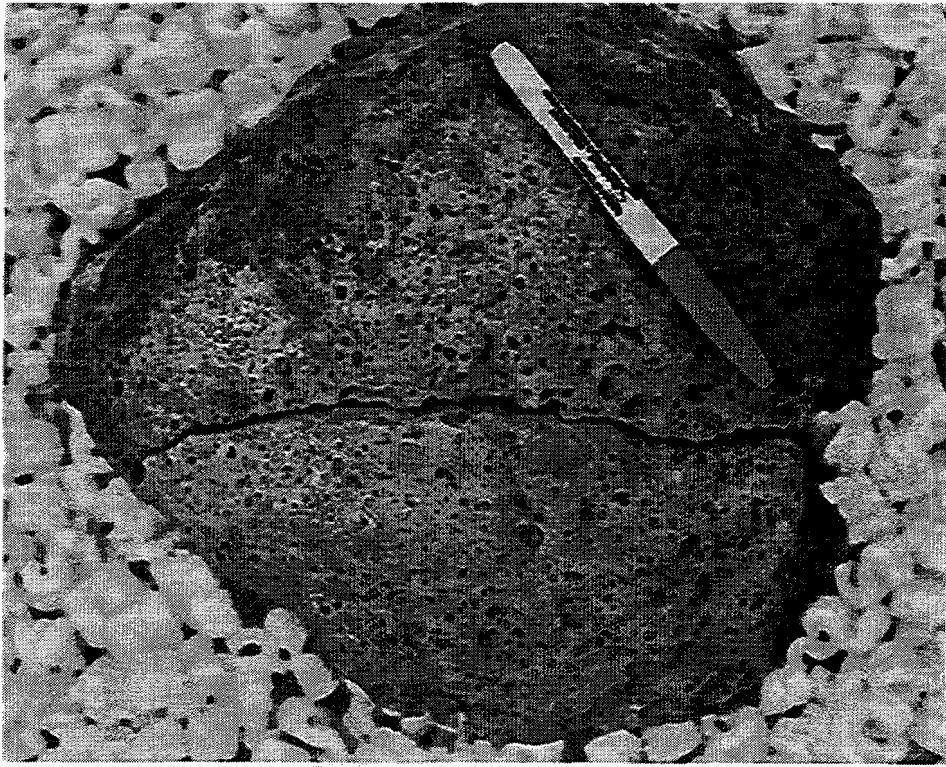
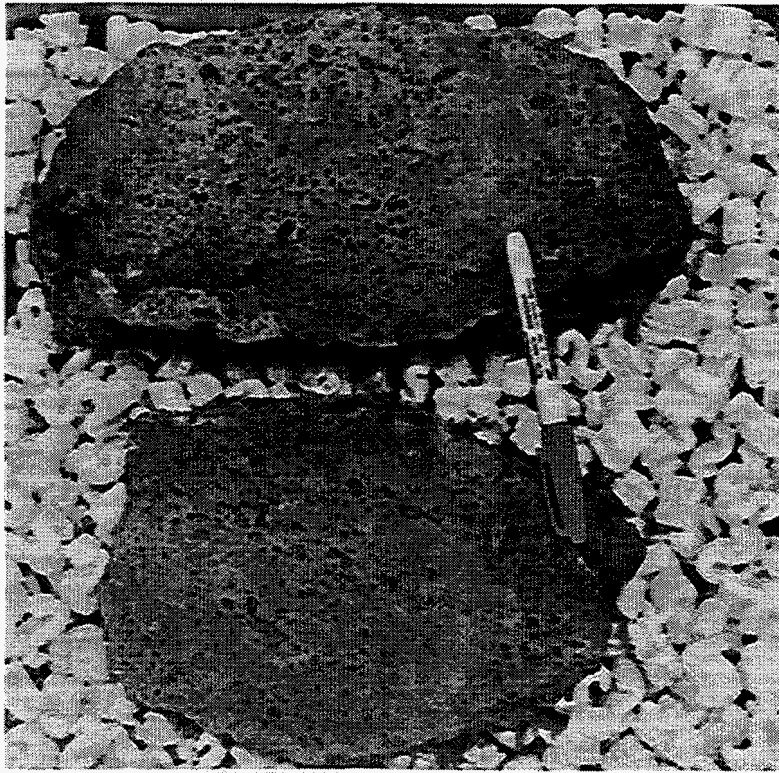(a) Transition from dense to vesicular basalt

(b) Fractures in dense basalt

Figure 5.2.1 Core II-5 from Box Canyon, INEL, 28.7'-38.1' bgs.

(a) Top view of fracture trace

(b) Fracture surfaces

Figure 5.2.2 Fracture outcrop sample from Box Canyon, INEL

6. Flow dynamic studies

6.1 Water-air studies

6.1.1 Seepage patterns in a transparent fracture replica

(J.T. Geller and G. Su, lead authors)

Flow visualization experiments of water seepage through a transparent replica of a natural rock fracture were performed with the objectives of (a) identifying important physical flow mechanisms by means of direct observation, and, (b) developing techniques for qualitative and quantitative laboratory-scale measurement of liquid seepage behavior in fractures. Following is a summary of these experiments. Further details can be found in Geller et al. (1996).

Our experiments are designed to observe water flow behavior at partially saturated conditions for constant, negative inlet water pressure, i.e., without external pressure forces. The purpose of the inlet condition is to eliminate flow instabilities arising from the inlet conditions (such as ponding). Water is delivered to the flow cell by means of a capillary siphon that draws water from a reservoir of constant water-level below the elevation of the flow cell inlet, shown in Figure 6.1.1.1. Changing the angle of flow-cell inclination allows us to vary the relative strength of capillary vs. gravity forces. Capillary forces induce spreading independent of flow direction and dampen flow instabilities, while gravity forces promote flow instabilities, increasing at higher angles.

Flow visualization experiments were performed in a 21.5 cm x 33 cm sized transparent replica of a natural granite fracture obtained within the context of an earlier project from the Stripa Mine, Sweden,. The transparent replica is an epoxy cast (Eccobond 27, W. R. Grace Co., Canton, MA) made from a silicone mold (Rhodorsil RTV 1556, Rhone-Poulec, Inc., Monmouth Junction, NJ) of the fracture surface. Both the silicone mold and epoxy cast are cured at room temperature. Details of the casting procedure, originally developed by Gentier (1986), are described in Su (1995) and Persoff and Pruess (1995a).

The advantages of using epoxy casts are that they allow the direct observation of

6.1.1 Seepage patterns in fracture replicas

liquid flow behavior and provide an accurate reproduction of the fracture surface topography, as was demonstrated in a comparison of profilometry measurements with a 10μm resolution of a rock and its epoxy cast (Persoff and Pruess, 1993). The epoxy replicas differ from natural rock fractures in several respects. The stress-state and mating of the fracture replica halves is different from the in-situ rock conditions, which may affect the aperture and asperity contact distributions. Note that this problem also exists for laboratory testing of actual rock fractures where the stress state has changed from in-situ conditions. Persoff and Pruess (1995b) compared fluid flow behavior between a fractured rock sample and its epoxy replica and noted larger absolute permeabilities in the replica relative to the rock. The casts do provide the general geometric features of the fracture surface, and results must be interpreted based upon the laboratory-measured aperture distributions.

The difference in surface chemistry of the epoxy compared to the natural rock and the impermeability of the epoxy cast affect the wettability of the surfaces to water. The replica may not reproduce small-scale surface roughness that is below the resolution of the profilometer. The contact angle of water on epoxy ranges from 57° to 65° (Geller et al., 1996), which falls in the range of intermediate or neutral wettability, as defined by Dullien (1988) for fluids with contact angles between 50° and 90°. For conditions of neutral wettability, capillary forces and trapping of the non-wetting phase are reduced compared to the strongly water-wet systems. Most common aquifer minerals, such as quartz, carbonates and sulfates, are strongly water-wet, however natural hydrophobic organic materials on the mineral surface, such as humic acids, as well as anthropogenic organic compounds, may change the wettability of the surface (Bradford and Leij, 1995a), creating conditions of neutral wettability. We observed that water wetted a smooth granite surface relative to air with a contact angle closer to that of water on the smooth epoxy surface, than water on glass (Geller et al., 1996), which is commonly used as an analog for natural rock surfaces (e.g. Nicholl et al., 1994). A water drop on the fracture surface of the same rock spread spontaneously, illustrating the important role that near-surface porosity in natural rock may have on wetting behavior. Although the porosity of granite is very small (less than 1%), weathering near the fracture surface and fracture coating materials may cause porosity near the fracture surface to be larger than in the bulk rock.

6.1.1 Seepage patterns in fracture replicas

The fracture replica is held together with steel flanges. The flanges may also contain a gasket on the edges of the outside surfaces of the replica overlain by transparent lexan plates to load the fracture by gas pressure, shown in Figure 6.1.1.2, modified from the design used by Nicholl et al. (1994). This assembly is placed over a light table with an adjustable angle and observations are photographed with a 35 mm SLR camera (Nikon, model N8008) or video camera (JVC KY-F55BU with lens JVC TY-10x6 MDPU) to obtain better resolution of time-dependent behavior. The video recorder (Sony SVHS no. SVO-5800) has time coding, which provides a temporal resolution of 1/30 s. Digital images are acquired from the video tape after the experiment with a frame grabber (Truevision, Targa 16/32 +F with Diaquest software controller) and measurements on the images are made with Adobe Photoshop® 3.0 for Windows.

A ceramic end-cap designed for two-phase flow experiments (Persoff and Pruess, 1995a, Persoff et al. 1995) is placed in the center third of the fracture inlet to deliver water to the fracture edge (Figure 6.1.1.3). The ceramic (Soil Moisture Corporation, Santa Barbara, CA) has a 50 kPa air entry pressure such that it remains saturated for capillary pressures below that value. The endcap allows ambient air to freely flow in and out of the fracture edge through grooves milled into sides and bottom of the end-cap, maintaining atmospheric air pressure at the fracture inlet. Inlet capillary pressure is then calculated from atmospheric pressure, minus the water pressure measured at the inlet fracture edge

Dyed water (0.2% Liquitint in deionized water by volume) is supplied with a constant head Mariotte bottle, shown in Figure 6.1.1.1, allowing the inlet pressure to be varied by adjusting the height of the Mariotte bottle. The addition of the dye results in a lowering of the water's surface tension and contact angle on the epoxy. For 0.4% Liquitint in deionized water, Geller et al. (1996) measured a surface tension of 64.4 mN/m and a contact angle on a sample of cast epoxy of 48°. Flow rates to the inlet end-cap are measured using a variable area flow-meter (Gilmont, shielded flow-meter, micro, Cole Parmer, IL). The fracture inlet pressure (P_w) is equal to the difference in elevation between the point of atmospheric pressure in the Mariotte bottle and the point of contact between the ceramic plate and the fracture inlet (h_w), minus the head loss through the ceramic plate (dP), or

$$\frac{P_w}{\rho g} = h_w - \frac{dP(Q, P_w)}{\rho g} \qquad (6.1.1.1)$$

21

where ρ is the density of water and g is the acceleration of gravity. The value of h_w is measured to a precision of ± 0.5 cm. The following discussion presents flow behavior in the current experiment as a function of h_w. Subsequent calibrations revealed that dP is on the order of one to two centimeters of water head for the flow rates in this experiment. This is large relative to the values of h_w therefore the pressure at the fracture inlet should be directly measured in future experiments.

The fracture replica, denoted ST-L-1-A&B, was inclined at angle of 70 degrees and was loaded by a confining gas pressure of 35 kPa. Filter paper was placed at the outlet of the fracture to promote drainage of the water and the sides of the fracture were sealed with gummed tape. The ceramic plate was saturated with water, placed into the opening in the fracture edge, and then h_w was set to -3.5 cm relative to the plate bottom. The value of h_w was increased from -3.5 cm to -1.5 cm in increments of 1 cm each day, followed by an increase from -1.5 cm to 2 cm in increments of 0.5 cm on consecutive days. The resulting fingering patterns were videotaped for 45 minutes at each value of h_w.

Water quickly entered the fracture after the saturated ceramic plate was placed at the inlet. The left-hand channel in Figure 6.1.1.4(a) formed after a few minutes, and the right-hand channel completely formed after approximately half an hour. A relatively broad, water-filled region formed above the right channel and below the inlet plate, but no such region formed above the left channel. The distribution reflects the presence of smaller apertures above the right channel compared to the left channel. After flow had equilibrated at h_w = -3.5 cm (approximately 24 hours) water only continued to flow through the right channel. Residual water from the initial invasion was held by capillary forces along what had been the left channel. The initial infiltrating finger is typically broader than the flowing channel behind the infiltration front, which creates a residual film of water along-side the flowing channel.

Although great care was taken to maintain uniform and steady boundary conditions at the fracture inlet, water flow generally proceeded in an unsteady manner through a given channel. The channels in Figure 6.1.1.4(a) have wider regions connected by thin

6.1.1 Seepage patterns in fracture replicas

threads, some of which are so thin that it is difficult to actually see the connections between the larger water-filled regions. All of the flow passes through these threads which go through cycles of breaking and reforming. These cycles occur sporadically, typically following a longer period of no observable changes in liquid distribution. Experiments at lower angles of fracture inclination also exhibit this behavior (Geller et al., 1966).

The four sequential images in Figure 6.1.1.4 show an intermittent flow event through the right-hand channel. The advancing finger (within the box in 6.1.1.4 (a)) merges with a segment of residual water in its flow path (6.1.1.4 (b)), then snaps after merging into a small pond of water held by capillary forces several centimeters down-gradient (6.1.1.4 (c)). After snapping, a slug of water quickly flows down the rest of the right channel (6.1.1.4 (d)), leaving residual water in its path. The average flow rate measured at this inlet condition was 1.3 mL/hr. Direct observation of the flow meter indicated that flow rates fluctuated as the water progressed through the flow channels, generally increasing after the thread snaps and then decreasing to a nearly constant flow rate as the channel reformed. Three to eight values of flow rates are noted at each value of h_w, as the flow meter does not provide continuous recording. The average and standard deviation of the noted flow rates at each value of h_w are shown in Table 6.1.1.1. The magnitude of the flow rate deviations do not indicate a dependence upon inlet conditions or flow rate.

The flow rate to the inlet of the fracture increased slightly at $h_w = -2.5$ cm. Under these conditions, water began flowing through both the left and right channels in an unsteady manner and the water entered the right channel at a faster rate than the left channel. This was evident from observations of the rate of finger growth after the thread had snapped in each channel. When h_w was changed to -1 cm several days later, water began flowing through the left channel at a faster rate than the right channel. The rate of flow through the left channel continued to be greater than the right channel as h_w was increased. The water continued to flow intermittently through both channels until h_w was increased to 2 cm. At this head, only the right channel exhibited intermittent behavior, and the left channel appeared to remain steady.

23

6.1.1 Seepage patterns in fracture replicas

Figures 6.1.1.5 and 6.1.1.6 summarize the observations of flow behavior as a function of h_w. The flow rate plotted in Figure 6.1.1.5 (a) increases non-linearly with h_w above a value of -1 cm. At lower pressures, water only flows through the teeth of the end-caps and the grooves are occupied by air. At higher pressures, water fills the grooves in the ceramic endcap, thereby providing a greater cross-section of flow for the water and allowing higher flow rates. This is evident from an estimate of the air entry pressure of the grooves in the ceramic endcap from the Young-Laplace equation:

$$P_c = P_{nw} - P_w = \sigma\left(\frac{1}{r_1} + \frac{1}{r_2}\right) \qquad (6.1.1.2)$$

where P_c is the capillary pressure, P_{nw} is the pressure of the non-wetting phase, P_w is the pressure of the wetting phase, σ is the surface tension of the liquid, and r_1 and r_2 are the principal radii of curvature of the air-water meniscus. For a groove geometry, r_1 is equal to $b(2cos\theta)^{-1}$, where b is the groove width, and θ is the contact angle. Assuming that r_2 is infinite, Equation (6.1.1.2) reduces to the following:

$$P_c = P_{nw} - P_w \approx \frac{2\sigma}{b}\cos\theta \qquad (6.1.1.3)$$

The surface tension of the water dyed with 0.4% Liquitint by volume is 0.0644 N/m, the contact angle is assumed to be zero, and $P_c = - P_w$ since the non-wetting fluid, air, is at atmospheric pressure. Substituting -1 cm for $P_w(\rho g)^{-1}$ and solving Equation (6.1.1.3) for b gives 0.12 cm , which is within an order of magnitude of the measured 0.07 cm groove width.

Figures 6.1.1.5 (b) and (c) show the location where the finger first snapped in the right and left channels, respectively, relative to the fracture inlet. In the right channel, the location is nearly constant at all values of h_w. In the left channel, the location of the snapping is constant for the three lowest values of h_w, then moves away from the fracture inlet as the inlet conditions change; this distance appears to increase with h_w, corresponding to the change in flow rates in 6.1.1.5 (a). The presence of the capillary-controlled region above the right hand channel and its absence above the left hand channel may be responsible for the different behavior of the 2 channels. The location of the thread snapping at a given pressure during the 45 minutes for which the experiments were recorded was constant, with the exception of $h_w = 0$ cm. The left channel broke 1.9 cm

24

6.1.1 Seepage patterns in fracture replicas

rather than 6.6 cm from the inlet boundary three times during this time interval. This other snapping location occurred sporadically during the 45 minute interval. The first of these events occurred about 13 minutes into this 45 minute interval, the second around 2 minutes after the first event, and the last about 6 minutes after the second event.

The time interval between intermittent flow events was noted from inspection of the video recordings over a 45 minute period at each value of h_w to determine whether or not this behavior was periodic. Plots of the accumulated number of snapping events versus time in Geller et al. (1996) show that in most cases, the number of snap-off events grows linearly with time, suggestive of periodic behavior. The slopes of these lines provide a quantitative measure of the frequency of flow intermittence, which are tabulated in Table 6.1.1.1, and plotted in Figure 6.1.1.6 (a) as a function of h_w. It is interesting to note that the frequency of snapping events increased and then decreased considerably in the left channel as the pressure was increased. The total snap-off rate, or the sum of snap-off rates in the left and right channels, is low at the negative values of h_w, increasing as h_w approaches zero. For h_w greater than zero, the total snap-off rate is higher than at the lowest two values of h_w (-3.5 and -2.5 cm) but there is no evident correlation with flow rate or h_w.

Alternatively, the volume of liquid metered through the fracture between snap-off events appears to exhibit more stable behavior as a function of flow rate. This value is estimated from the average flow rate divided by the total snap-off rate, shown in Table 6.1.1.1. The volume of liquid per snap-off is fairly constant at pressure heads less than and equal to zero and then increases at h_w greater than zero. This trend is clearly seen in Figure 6.1.1.6 (b), which plots the total snap-off rate and liquid volume/snap-off as a function of flow rate. The different behavior at the higher flow rates reflects the change in flow regime as inlet pressure heads move from negative to positive. The change in location of thread snapping in the left channel at higher flow rates is also consistent with a change in flow regime. Section 6.1.4 explores the dynamics of thread snapping for a sequence of parallel plates designed to capture the fracture geometry that controls this behavior.

6.1.1 Seepage patterns in fracture replicas

Table 6.1.1.1. Intermittent flow behavior in fracture replica

h_w	Average flow rate	Standard deviation	Snap-off rate (events/min)			Liquid volume/ snap-off
(cm)	(mL hr^{-1})	(mL hr^{-1})	left channel	right channel	total	(mL)
-3.5	1.331	0.451	no snapping	0.134	0.134	0.166
-2.5	1.445	0.086	0.081	0.079	0.160	0.151
-1.5	2.117	0.107	0.126	0.178	0.304	0.116
-1.0	2.381	0.145	0.155	0.094	0.249	0.159
-0.5	4.043	0.306	0.063	0.332	0.395	0.171
0.0	4.589	0.274	0.374 [1] 0.133 [2]	0.043	0.550	0.139
0.5	5.749	0.194	0.234	0.058	0.292	0.328
1.0	6.075	0.184	0.215	0.045	0.260	0.389
2.0	not measured	not measured	no snapping	0.392	0.392	--

(1) snap-off occurred 6.6 cm from fracture inlet
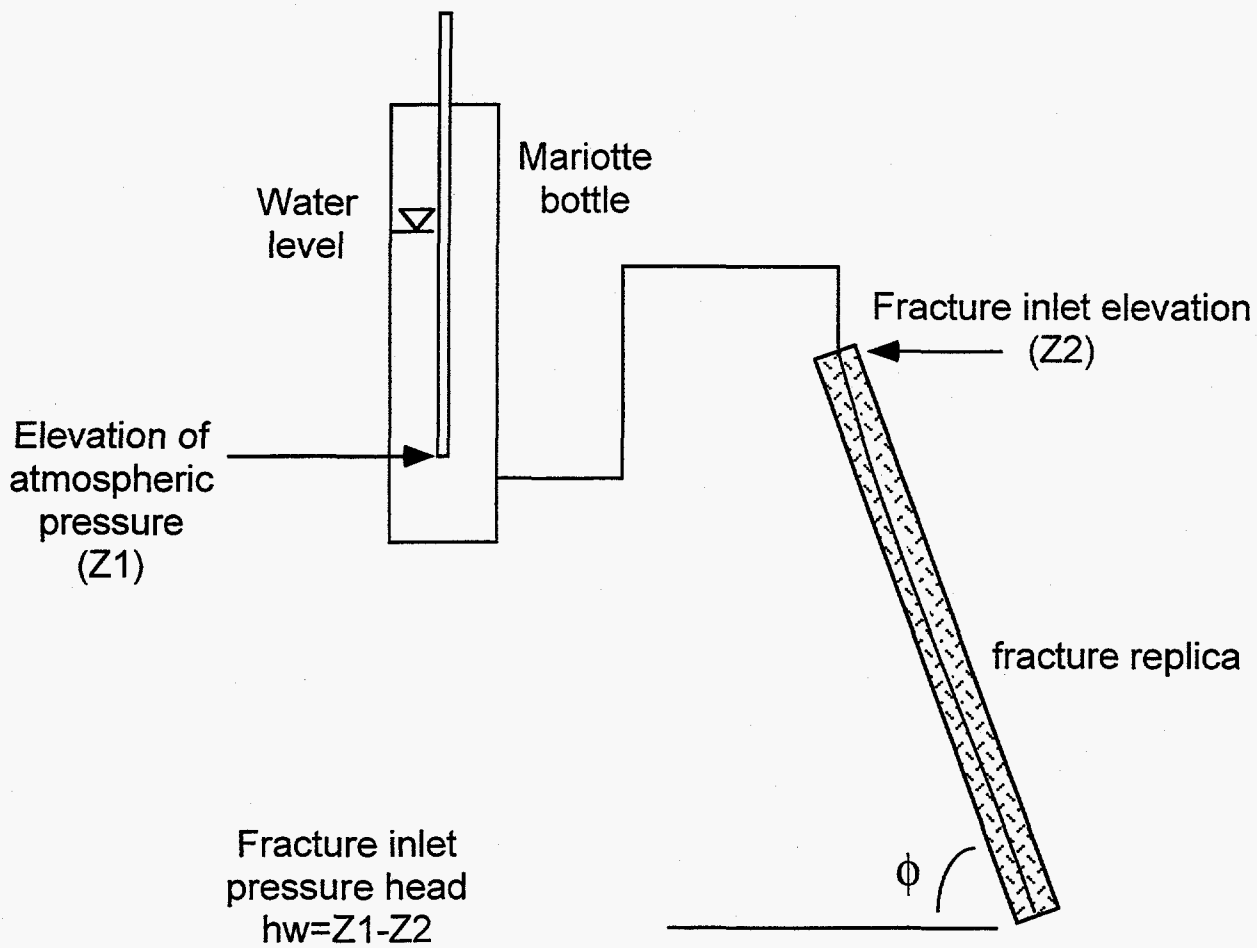(2) snap-off occurred 1.9 cm from fracture inlet
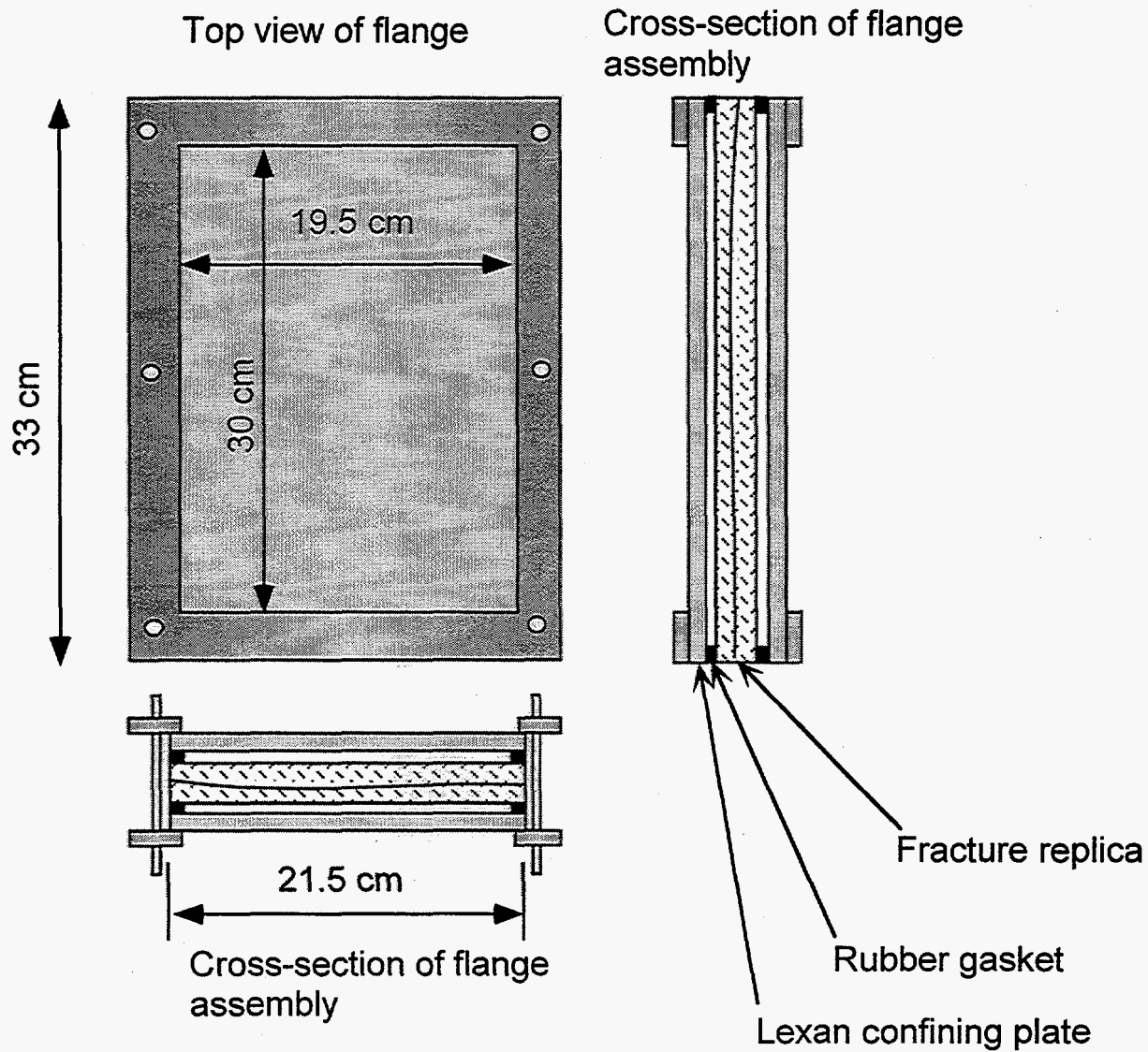
Figure 6.1.1.1 Water delivery to fracture replica

Top view of flange

Cross-section of flange assembly

19.5 cm

30 cm

33 cm

21.5 cm

Cross-section of flange assembly

Fracture replica

Rubber gasket

Lexan confining plate

Figure 6.1.1.2 Replica-flange assembly
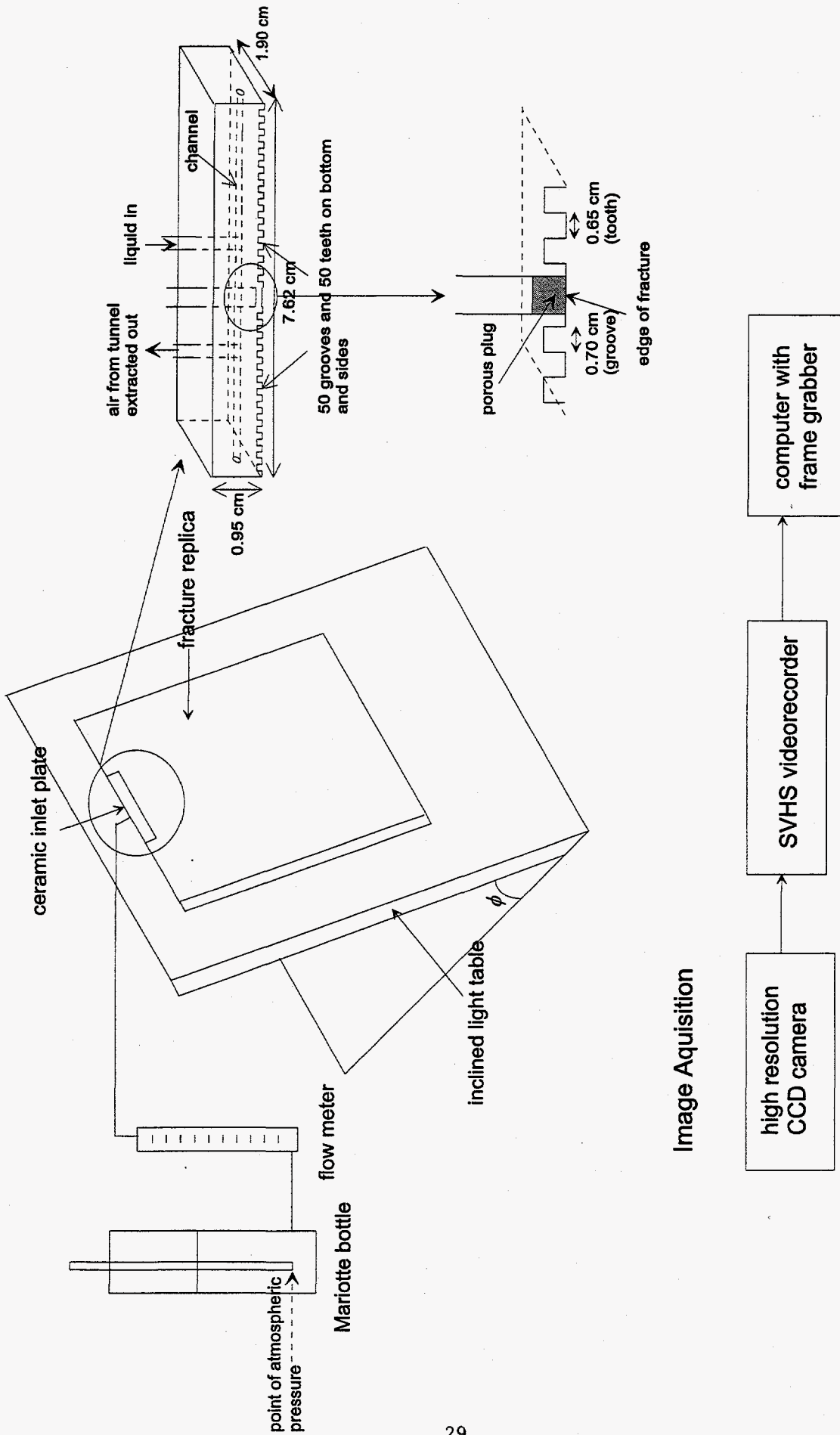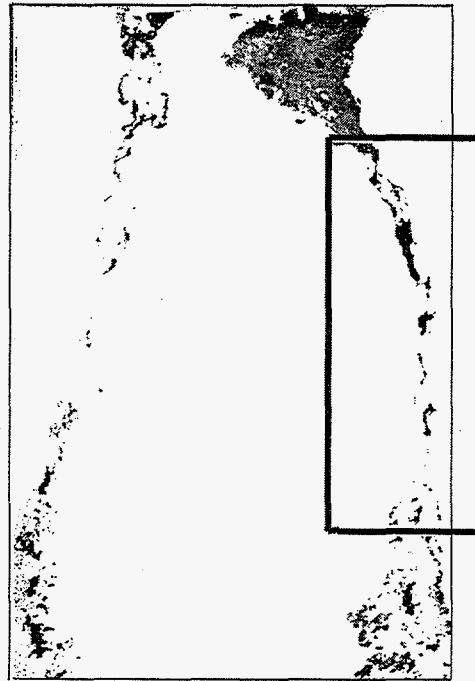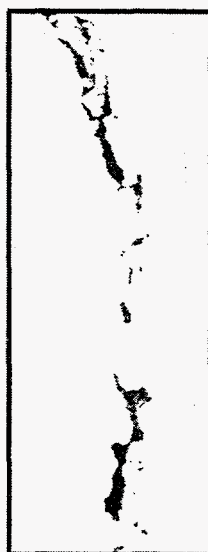
Image Aquisition

Figure 6.1.1.3: Schematic of Apparatus for Water Seepage Experiments
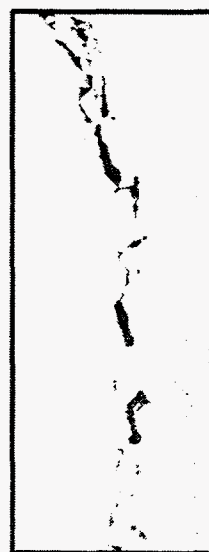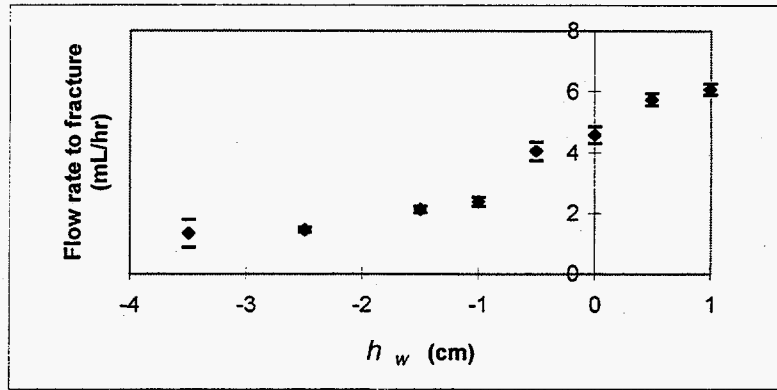
29

(a) t=12:39-1

(b) t=12:39-2   (c) t=12:39-3   (d) t=12:39-4

Figure 6.1.1.4 Liquid distribution during percolation, $\theta = 70^o$, $h_w = -3.5$ cm. Liquid channels appear disconnected, but water is flowing through the right channel as indicated by the change in distribution with time. Images are within seconds of one another. (b)-(d) are enlargements of boxed are in (a).

(a) Flowrate into fracture (bars are plus and minus
one standard deviation)
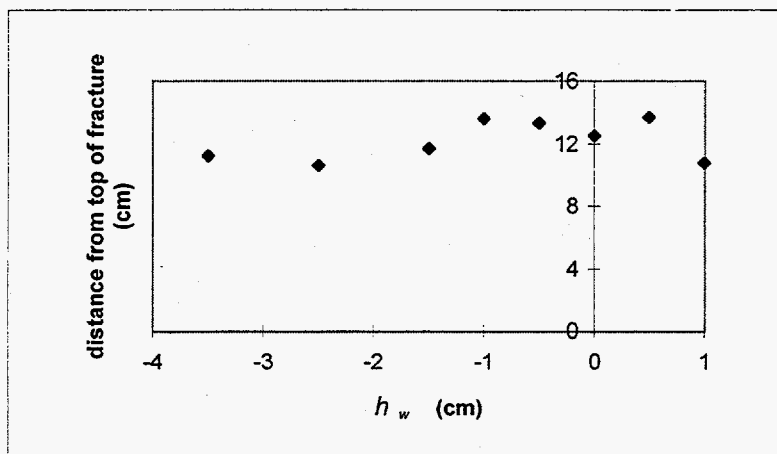
(b) Location of thread-snapping in right channel
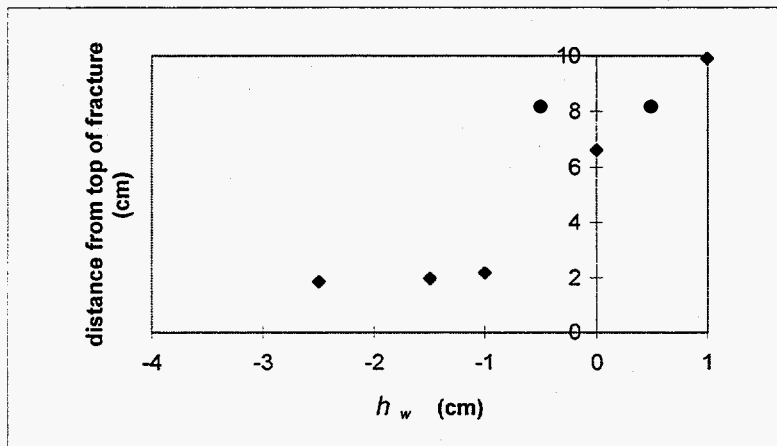
(c) Location of thread-snapping in left channel

Figure 6.1.1.5 Flow behavior in fracture replica
as a function of inlet conditions, $\theta = 70°$

31

(a) Total snap-off rate

(b) Liquid volume/snap-off

Figure 6.1.1.6. Snap-off rates and liquid volume/snap-off in fracture replica

6.1.2 Aperture maps in a fracture replica

(J. T. Geller and G. Su, lead authors)

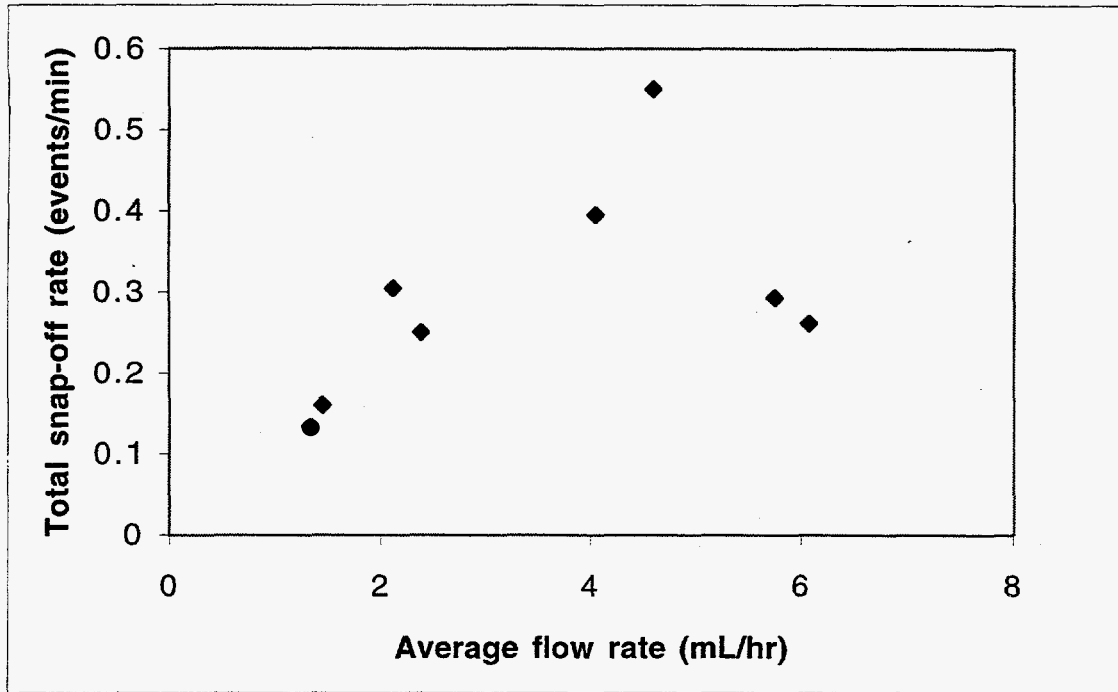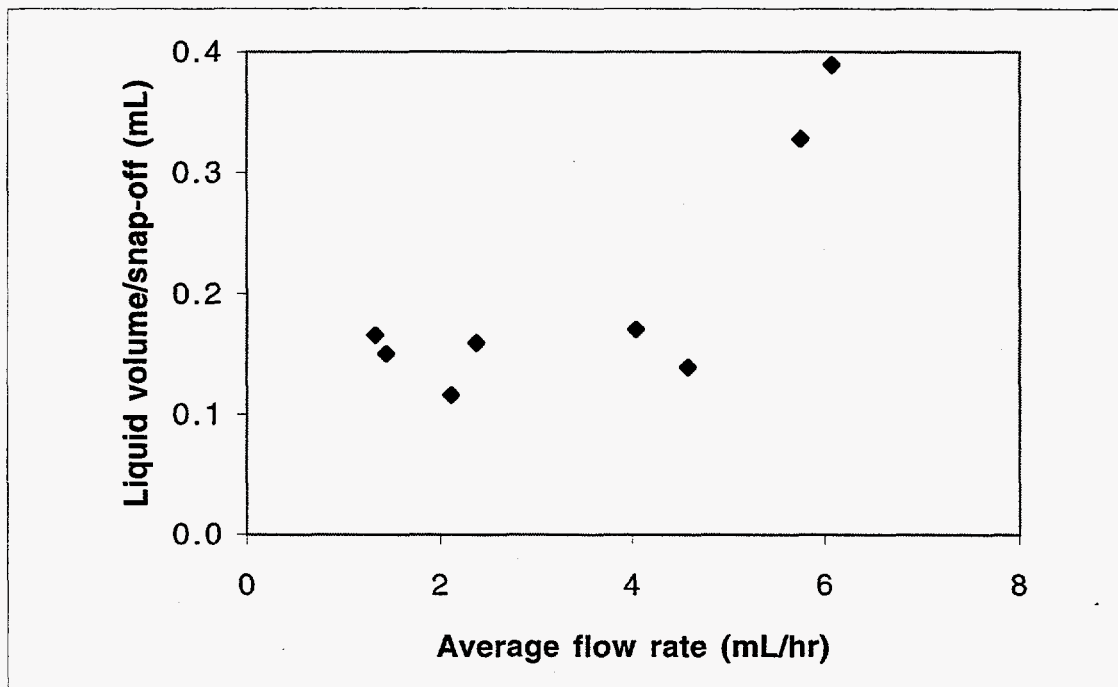The aperture distribution of the fracture replica denoted as STL-1-A&B was measured using light attenuation to examine the relationship between the aperture distribution and the resulting flow patterns. Measurements of the apertures were made with and without a gas confining pressure of 34.5 kPa applied to the fracture to determine the sensitivity of the aperture distribution to the loading placed on it. The hydraulic aperture of the fracture was also measured to compare it with the results from the light attenuation measurements.

Procedure

The aperture distribution was derived from the light intensity map of the image of the fracture saturated with water dyed with Liquitint Patent Blue (Milliken Chemical, Inman, SC), normalized by the image of the fracture saturated with clear water. Normalization of the dyed image by the clear water image compensates for light refraction at the solid-liquid interface. The dye concentration was set to 0.2% to establish the best resolution of the estimated aperture range. The attenuation of light is a function of the distance the light travels, and is correlated to the width of open space of the fracture by calibration to the intensity of light transmitted through known apertures filled with the same liquids. This technique has been used by Persoff and Pruess (1993, 1995a), Nicholl et al. (1994), and Glass and Nicholl (1995).

The calibration apertures were constructed with glass plates separated by shims of known thickness. Images were acquired with a 1024x1024 pixel by 12 bit grey-scale digital camera (SpectraSource Instruments, MCD1200, Westlake Village, CA), with a 35 mm f2 AF Nikon lens and an ND2 filter. The fracture was mounted over a halogen light table (VP 400 Floor Illuma, Bencher, Wood Dale, IL). The height of the camera was adjusted so the length of the fracture fills the field of view; this determined a spatial resolution of 0.31 mm for this fracture. Eight images were averaged for each measurement. The images of the fracture saturated with dyed water were normalized by dividing them by the clear water-saturated images, using the software that drives the camera and further processed with Global Lab Image (Data Translation, Marlboro, MA). A FORTRAN program was written to compute the total pore volume of the fracture from the binary image file, using the calibration curve of aperture width to light intensity.

The sides of the fracture replica were sealed and end-caps with fittings for injecting water through the fracture were placed at the inlet and outlet, shown in Figure 6.1.3.1. The top and bottom of the fracture were loaded using the Lucite confining plates and the metal

frame used in the water seepage experiments (Section 6.1.1 and Geller et. al., (1996)). Carbon dioxide was injected into the fracture inclined at 10 degrees for approximately 15 minutes to flush out the air. De-aired water was then injected into the fracture using a syringe pump (Model 33, Harvard Apparatus, South Natick, MA) at a rate of 3 mL/min until the water broke through at the outlet of the fracture. The flow rate was then decreased to 0.5 mL/min and water was continuously injected into the fracture at this rate until it became fully saturated. Full saturation took about two weeks, during which time approximately 650 L of water were pumped through the fracture. Images of the fracture saturated with clear water were made of the fracture without, and then with, gas confining pressure. Afterwards, the gas confinement was relieved and the fracture was saturated with dyed water. The fracture was determined to be saturated with dyed water by comparing consecutive measurements of light intensity as a function of the volume of dyed water injected, until there was not detectable difference. This took two days at a flow rate of 0.5 mL/min, for a total volume of approximately 1.5 L.

Fracture transmissivity was also measured with and without a gas confining pressure. The pressure drop was measured across the fracture using a differential pressure transducer (DP15-20, Validyne Engineering Corp., Northridge, CA) for a range of flow rates delivered with a syringe pump. The transmissivity was calculated from the linear regression of flow rate vs. pressure drop. The hydraulic aperture, b, was calculated using the cubic law for saturated flow through parallel plates and the measured transmissivity, T:

$$b = (\frac{12\mu T}{\rho g})^{1/3} \tag{6.1.3.1}$$

where μ is the viscosity of the water, ρ is the density, and g is the gravitational acceleration constant.

Discussion

The aperture maps of the fracture replica are shown in Figure 6.1.2.2. These aperture maps are aligned in the same position as the fracture replica was for the water seepage experiments described in Section 6.1.1 and in Geller et al. (1996). The general structure of the aperture distribution consists of a region of small apertures in the top and middle of the fracture that form a gently swirling region down the center of the fracture and to the lower edges. These smaller apertures, which presumably include asperity contacts, support the more open regions on the left and right sides of the fracture. The apertures are larger under gas confining pressure except along the edges near the rubber gasket, indicating that the gas confinement caused some buckling of the fracture. The mean aperture computed from the light intensity image for the unconfined fracture is 0.071 mm

± 0.051 mm (standard deviation), giving a total pore volume of 4.1 mL, and with confining pressure was 0.074 ± 0.030 mm (standard deviation), giving a total pore volume of 4.3 mL. These small differences reflect the fact that the smallest apertures changed more significantly between the unconfined and confined fracture. These values are for the exposed fracture only, and do not account for the fracture space obscured by the top and bottom flanges.

The region of small apertures distributed near the top agreed with observations from the preliminary water seepage experiments (Section 6.1.1 and Geller et al. (1996)). Water consistently filled this region due to the strong capillary forces produced by the small apertures. In a fully saturated fracture, the water preferentially entered the regions with the large apertures, as shown in a sequence of images of dyed water injected at 1 mL/min into the fracture saturated with clear water (Figure 6.1.2.3) without confining pressure. The dyed water broke through to the fracture outlet after 21 minutes, or 21 mL of injected volume. This is much greater than the pore volume of the fracture measured from the light intensity image because of the additional inlet volume and fracture pore volume outside of the image, noted in the previous paragraph.

The transmissivity of the fracture was measured to be 0.258 cm^2/s without confining pressure and 0.207 cm^2/s with the gas confining pressure. The corresponding hydraulic apertures calculated from the transmissivities were 0.31 mm and 0.29 mm, respectively. The hydraulic apertures are close to the values of the largest apertures in the fracture, because the apertures on the sides of the fracture controlled the flow of liquids through the fracture when it was saturated. The hydraulic aperture measured under gas confining pressure was less than the value measured without the confining pressure, which is contrary to the aperture distribution seen in Figure 6.1.2.2. The gas confinement compressed the inlet and outlet edges of the fracture, which apparently controlled the pressure drop across the fracture and resulted in a lower transmissivity.

Summary

Aperture maps and hydraulic aperture measurements were made of the fracture replica STL-1-A&B. The general aperture distribution consisted of a region of small apertures in the top and middle of the fracture with large apertures on the left and right sides. The small aperture region located at the top of the fracture agreed with observations from the water seepage patterns discussed in Section 6.1.1 and in Geller et al. (1996). In the water-saturated fracture, the two large aperture regions along the left and right side of the fracture controlled the flow of the water. This was evident from observations of the flow of dyed water into the fracture saturated with clear water and from the calculations of

the hydraulic aperture. The hydraulic aperture of the fracture with and without 34.5 kPa gas confining pressure was measured to be 0.29 mm and 0.31 mm, respectively. The aperture map and computation of the mean fracture aperture showed that the apertures actually increased under the gas confining pressure, however. The increase in the apertures was the result of a slight bulging of the fracture replica due to the compression of the edges of the fracture.

Top view of flange
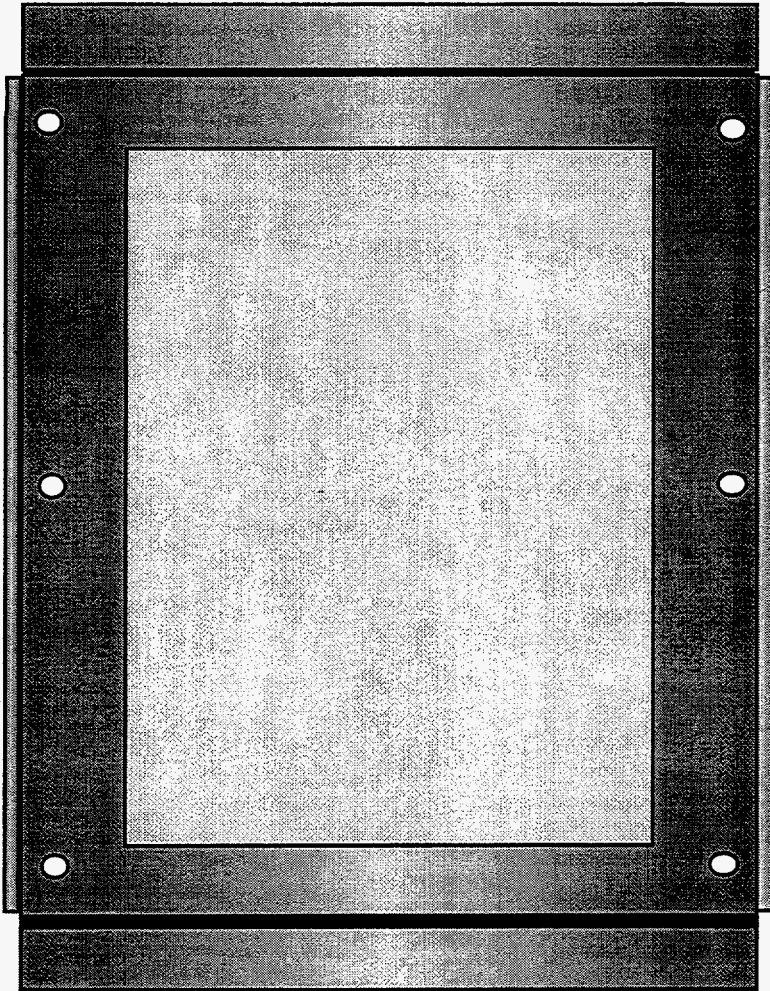
Cross-section of flange assembly
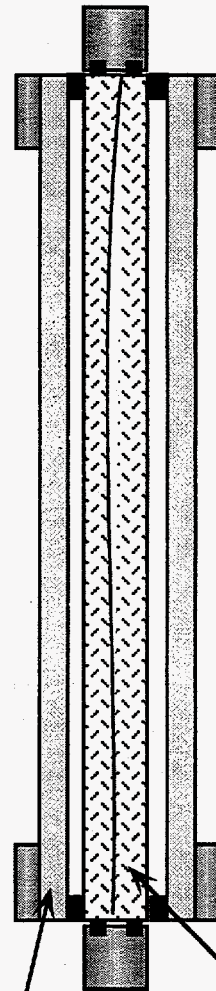
Fracture replica

Lexan confining plate
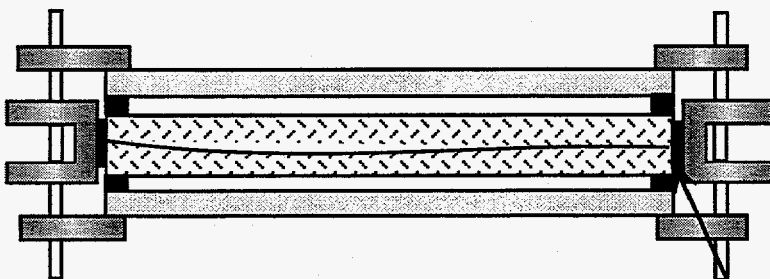
Cross-section of flange assembly

Rubber gasket

Figure 6.1.2.1 Fracture replica assembly for liquid-saturated conditions
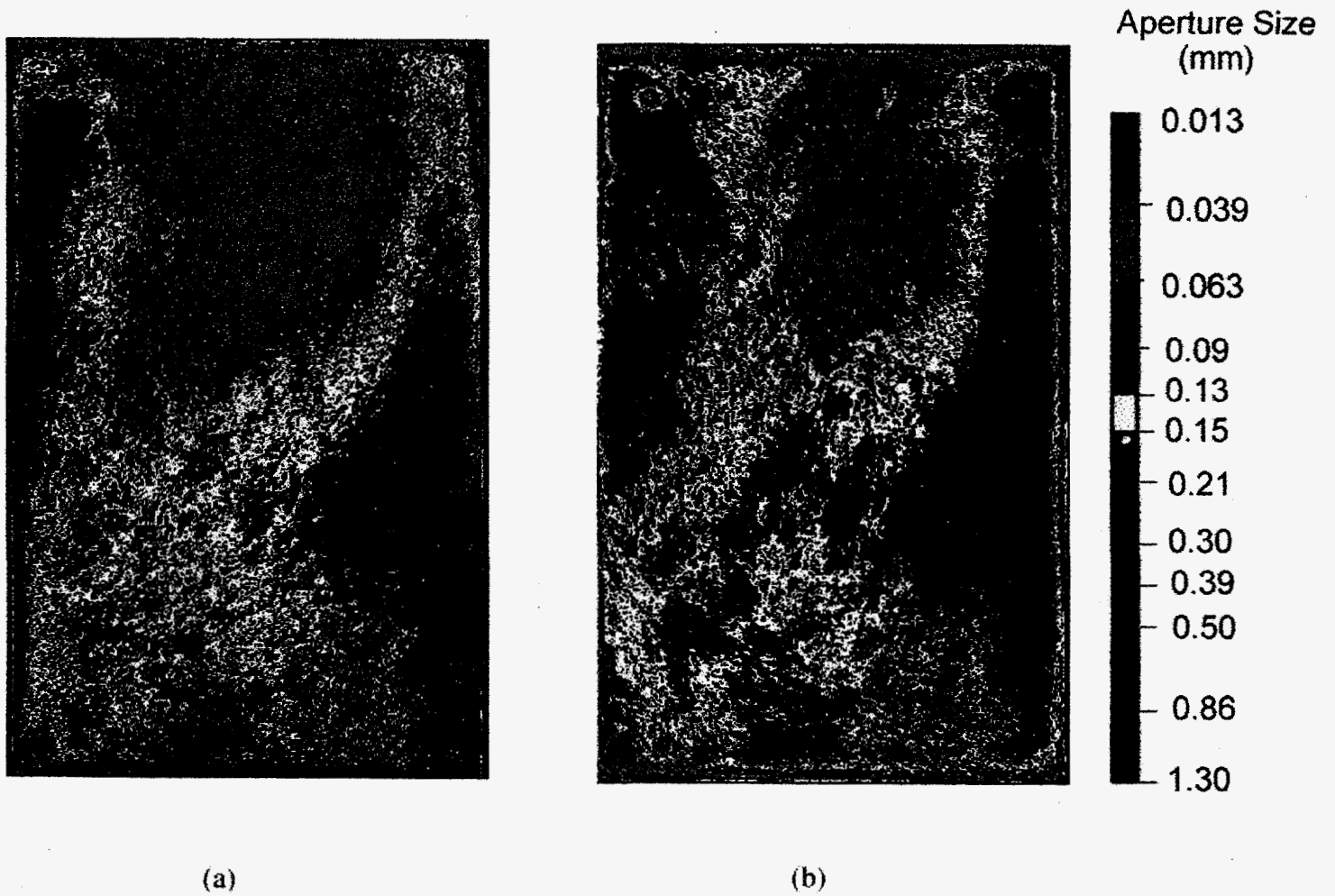
Figure 6.1.2.2 Aperture distribution maps of transparent fracture
replica. (a) no confining pressure (b) 5 psi confining pressure
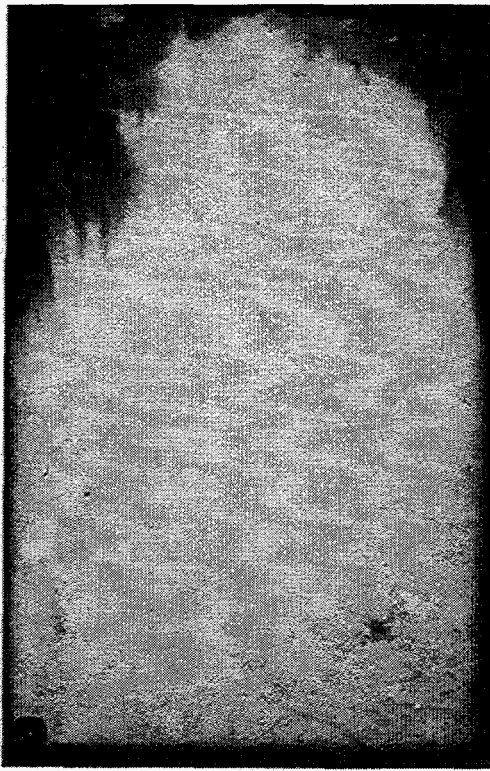
(a) 4 minutes

(b) 21 minutes

(c) 45 minutes

(d) 55 minutes

Figure 6.1.2.3 Injection of dyed water into water-saturated fracture.
(a)-(d) Time after beginning injection of dyed water at 1 mL/min.

6.1.3 Flow intermittence in controlled aperture sequence cells

(G. Su and J. T. Geller, lead authors)

Parallel plate experiments were conducted to further investigate the intermittent flow behavior observed in the water seepage experiments. Some preliminary experiments discussed in Geller et al. (1996) were performed using Lucite and glass plates with a medium-large-small aperture sequence. Those experiments demonstrated that the cyclic formation and snapping of liquid threads could be reproduced using this type of aperture sequence, shown in Figure 6.1.3.1. Water advances under gravity through the medium section until it encounters a capillary barrier at the interface of the medium and large aperture sections which allows the formation of a thread through the large aperture section. When the thread reaches the small aperture, the strong capillary force provided by the small aperture section pulls the thread through at a faster rate than the supply of water through the top section, thereby causing it to snap. The flow capacity, or permeability of the small aperture section must be sufficient to pull the liquid away. A comparison of the liquid distribution in Figure 6.1.1.4 and the fracture aperture distribution in Figure 6.1.2.2 shows that the location of the flow channels follows the medium-large-small aperture sequence, indicated by yellow-green/blue- red regions on the aperture map.

Additional experiments were conducted to better characterize the time intervals between snapping events as the flow rate and angle of inclination were varied. Flow rates of the thread entering and draining from the middle section of the plates were also made to investigate the relationship between these flow rates and the time interval measured between the snapping events.

Procedure

For a detailed study of the thread-snapping dynamics, glass plates with an aperture sequence of 0.25 mm, 0.66 mm, and 0.10 mm for the top, middle, and bottom sections, respectively were assembled as described in Geller et al. (1996). The schematic of the experimental apparatus is shown in Figure 6.1.3.2. Water was introduced to these plates using a Mariotte bottle with felt placed in the end of the tubing where it contacted the plates. Water was

supplied only to the top middle third of the plates, allowing the top section to become partially saturated. A needle valve was used to control the flow rate to the plates and a variable area flow meter was used to measure the inlet flow rate. Filter paper was placed in the lower 6.5 cm of the bottom section to avoid capillary end effects when the water encountered the outlet of the plates. The sides of the cell were left open to the atmosphere. The cell had an overall dimension of 21.6 cm wide by 33 cm long and was mounted over an inclined light table.

Experiments were conducted at two angles, 58° and 70°. Three flow rates were applied to the plates inclined at 58° and four flow rates were applied to the plates inclined at 70°. The experiments were videotaped for approximately 30 minutes at each flow rate using a high resolution video camera (JVC KY-F55BU with lens JVC TY-10x6 MDPU) and recorded on a time-coded videotape recorder with a temporal resolution of 1/30 s (Sony SVHS no. SVO-5800). The time between snapping events was measured by reviewing the videotape and recording the time of each snapping event. Digital images from the videotape were acquired using a frame grabber (Truevision, Targa 16/32 +F with Diaquest software controller). Measurements of the images were made with Adobe Photoshop® 3.0 for Windows to obtain velocities and flow rates of the thread formation and drainage.

Observations

Three types of thread formation patterns were observed in the experiments:

(1) a thread formed in the middle section and snapped before reaching the interface between the middle and bottom plates

(2) a complete thread formed in the middle section and snapped after a period of connected flow

(3) a steady thread formed in the middle section that did not snap

Pattern 1 is similar to the phenomenon of the dripping faucet. This occurs when the weight of the fluid overcomes the surface tension force and a certain volume of water breaks off from the liquid supply. This pattern dominated when the flow rate to the plates was below approximately 8 mL/hr at both angles of inclination. Since pattern 2 is hypothesized to occur in

the fracture replica experiments, the flow rates supplied to the plates were maintained high enough so that this pattern was observed. The range of flow rates where pattern 2 was observed in these experiments occurred roughly between 8-12 mL/hr at 58° and 8-24 mL/hr at 70°. The range of flow rates where pattern 2 occurred increased at 70° due to the increase in the gravitational force, which makes the thread more unstable and more likely to break at higher flow rates. Pattern 3 occurred at flow rates above the maximum value of the range for pattern 2.

The various stages of pattern 2 are shown in Figure 6.1.3.3, which is a schematic representation of the actual captured images from the videotape shown in Figure 6.1.3.4. The advancing front of the thread formed at the interface between the top and middle plates. After advancing about 2 cm into the middle section, the width of the thread at the top of the middle section began to decrease. The thread continued to advance through the middle section leaving an extremely thin "tail", while the "head" of the thread continued to increase in size until it reached the bottom section. The head of the thread then drained into the bottom section, and after some time the tail of the thread snapped at the top of the middle section. A piece of the head of the thread would generally remain near the bottom of the middle section upon snapping (as shown in Figures 6.1.3.3 and 4) when the plates were inclined at 70°. At 58°, the head of the thread would generally drain completely into the bottom section, leaving behind a tail the length of the middle section, and after some time the tail would snap at the top of the middle section. Residual water from the thread remained on the plates after each snapping event. A new thread immediately began to form at the top of the middle section after snapping. Pattern 1 also proceeded in the same manner, except that the thread snapped before reaching the bottom of the middle section. Changing the flow rate or angle of inclination did not appear to change the width of the head or tail of the thread.

Plots of the distance vs. time for a thread entering the middle section are shown in Figure 6.1.3.5. The distance is measured from the top of the middle section. The corresponding width of the thread measured at the top of the middle section (w_t) plotted as a function of time, is also shown in Figure 6.1.3.5. The definition of w_t is shown in Figure 6.1.3.3. Plots of only two flow rates, one at each angle, are shown in this figure since the plots are very similar regardless of the

flow rate or angle of inclination. A distinct change in the slope occurs in all of the plots when the thread reaches a distance of 2 cm. This distance corresponds to the time when the width of the thread begins to thin (thereby decreasing the cross sectional area available for flow). In order to maintain continuity, the velocity of the thread increases, which accounts for the change in the slope in these plots.

Time Intervals Between Snapping Events

Plots of the cumulative snapping event number as a function of time are shown in Figures 6.1.3.6 and 7 for the plates inclined at 58° and 70°, respectively. The slopes of these lines provide a measure of the average frequency of the snapping events (snaps/min), which is summarized below in Table 6.1.3.1. The inverse of this frequency is the average time between each snapping event (dt_{ave}), which generally increased as the flow rate increased. The time for the thread formation (dt_{form}), measured at the first appearance of water at the top of the middle section to the time it reached the bottom of the middle section, was also averaged for all the snapping events measured at a particular flow rate and is given in the Table 6.1.3.1. The difference between dt_{ave} and dt_{form} is the average time for the thread to drain into the bottom section before it snapped (dt_{drain}). Definition sketches of dt_{form} and dt_{drain} are shown in Figure 6.1.3.3. As the flow rate increased, the average value of dt_{drain} increased presumably because the ratio of the applied flow rate to the flow capacity of the bottom section became larger. The average value of dt_{drain} was also larger at 58° compared to 70° when the same flow rate was applied due to the decrease in the magnitude of the gravitational force. The large difference in dt_{drain} relative to the small difference in gravitational force (sin 70/sin 58 ~ 1.3) and dt_{form} suggests that gravity strongly affects the rate at which the bottom section pulls in the water.

43

Table 6.1.3.1: Average frequencies and time intervals between snapping events

φ	flow rate (mL/hr)	freq. from slope (snaps/min)	dt_{ave} (sec)	dt_{form} (sec) (average)	dt_{drain} (sec) (average)
58	8.8 ± 0.7	0.7123	84.2	43.1	41.1
	10.6 ± 0.7	0.6592	91.0	38.7	52.3
	11.8 ± 0.3	0.6892	87.1	31.4	55.7
70	8.6 ± 0.4	1.4000	42.9	35.9	7.0
	10.1 ± 0.5	1.3835	43.4	35.9	7.5
	14.5 ± 0.5	1.0794	55.6	27.5	28.1
	23.7 ± 1.2	0.8862	67.7	24.4	43.3

The cumulative number of snapping in Figures 6.1.3.6 and 7 grew nearly linearly with time, indicating that to a first order, the frequency of the snapping events is periodic. Variations in the time interval between snapping events are apparent in most of the plots presented in Figures 6.1.3.6 and 7. The points deviate from the straight line in a repetitive pattern, suggesting that the time interval between snapping events may be quasi-periodic and that more than one frequency may occur at a particular flow rate.

Flow Rates of Thread Formation and Drainage

Flow rates of threads forming and draining in the middle section were made to investigate the possible relationship between these flow rates and the variations in the time intervals between snapping events. These flow rates were measured using captured images from videotaped experiments at 58° and then analyzed using Adobe Photoshop®. The flow rate of the thread entering the middle section (Q_{in}) was obtained by measuring the change in the volume of the thread over time before it reached the bottom of the middle section. The volume of water was calculated by measuring the number of pixels of the thread, multiplying by a conversion factor to obtain the area of water corresponding to the number of pixels, and then multiplying by the aperture of the middle section:

$$V_{water} = (\# \text{ of pixels})(0.00124 \text{ cm}^2/\text{pixel})(0.066 \text{ cm}) \tag{6.1.4.1}$$

Plots of V_{water} as a function of time are shown in Figure 6.1.3.8. A linear regression was performed on this data to obtain Q_{in} from the slope.

Since the flow rate of the thread draining (Q_{out}) could not be measured directly, a mass balance of the water was performed across the middle section of the plates to obtain the drainage flow rate as follows (neglecting evaporation):

$$Q_{out} = Q_{in} - \frac{dV_{water}}{dt} \qquad (6.1.3.2)$$

where dV_{water}/dt is the change in storage of the water over time in the middle section. The value of dV_{water}/dt was determined in the same manner as Q_{in}. The number of pixels was measured after the head of the thread had reached the bottom of the middle section and V_{water} was calculated from equation (6.1.3.1). V_{water} was then plotted over time to obtain dV_{water}/dt from the slope of the linear regression. Figure 6.1.3.9 are plots V_{water} as a function of time for one thread at each of the flow rates at 58°. A new value of dV/dt was calculated if the slope from these plots changed (e.g. Figure 6.1.3.9(c)). Assuming Q_{in} was constant during the time the thread drained into the bottom section, Q_{out} was calculated using equation (6.1.3.2). Definition diagrams of Q_{in} and Q_{out} are shown in Figure 6.1.3.10.

Table 6.1.3.2 below summarizes the flow rates of the thread entering and draining from the middle section and the change in storage of the thread. Two different cycles of the thread formation and snapping were analyzed at each of the three flow rates applied to the plates inclined at 58°. The time indicated in the table equals zero at the time a different flow rate (Q) was applied.

Table 6.1.3.2: Flow rates of the thread entering and draining
from the middle section; $\phi = 58°$

	time (sec)	Qin (mL/hr)	dV/dt (mL/hr)	Qout (mL/hr)	Qin/Qout
Q = 8.8 mL/hr thread 1 dt = 72.3 sec dt$_{drain}$ = 33.8 sec	396.5 - 414.5 420.5 - 432.5 437.2 - 451.9	14.270	 -17.366 0	 33.210 NA	 0.430 NA
thread 2 dt = 68.8 sec dt$_{drain}$ = 22.7 sec	535.5 - 553.5 556.5 - 576.3	14.418	 -16.495	 30.913	 0.466
Q = 10.6 mL/hr thread 1 dt = 51.7 sec dt$_{drain}$ = 11.8 sec	522.5 - 537.5 546.5 - 556.0	12.960	 -19.080	 32.04	 0.404
thread 2 dt = 97.0 sec dt$_{drain}$ = 57.3 sec	570.5 - 588.5 597.5 - 615.5 615.5 - 653.0	13.687	 -17.168 0	 30.856 NA	 0.444 NA
Q = 11.8 mL/hr thread 1 dt = 159.1 sec dt$_{drain}$ = 128.6 sec	59.3 - 74.3 80.3 - 92.3 98.3 - 108.3 108.3 - 200.6	20.520	 -11.880 -6.120 0	 32.400 26.640 NA	 0.633 0.770 NA
thread 2 dt = 47.2 sec dt$_{drain}$ = 15.0 sec	215.5 - 233.5 233.5 - 245.5 245.5 - 248.5	20.160	 -6.775 0	 26.935 41.400	 0.748 0.487

Table 6.1.3.2 shows several instances when dV/dt equals zero. According to equation 6.1.3.2, Q_{in} equals Q_{out} for dV/dt equal to zero. This is not physically plausible because the magnitude of the two flow rates must differ for the thread to eventually snap. Storage changes in the top and/or bottom sections must therefore occur in this period, however they could not be measured from the images since the video camera was positioned in such a way that it cropped off approximately half of the top and bottom sections. The camera was placed in this position to produce images with a high enough resolution to measure the thread volume. The drainage flow rates that could be measured at Q = 8.8 and 10.6 mL/hr had nearly the same values for the threads that were analyzed. The drainage flow rates for the two threads analyzed at Q = 11.8 mL/hr changed over time and not in a consistent manner.

The relationship between the ratio of Q_{in} to Q_{out} and dt$_{drain}$ is not apparent from the results in Table 6.1.3.2 since some of the values of Q_{out} could not be measured. Without knowing liquid storage changes in the top and bottom sections, we cannot check the assumption that Q_{in}

46

during thread drainage is equal to the value calculated for thread formation, and consequently whether Q_{out} is accurate. However, one would expect that an increase in the ratio between Q_{in} to Q_{out} would result in an increase in dt_{drain} and dt.

Changes in the water saturation in the top and bottom sections may cause variations in Q_{in} and Q_{out}, and consequently result in erratic time intervals between snapping events. Saturation is related to the relative permeability, where a larger relative permeability occurs at higher saturations. The flow rate of water, Q_w, which is shown below in the form of the multi-phase extension of Darcy's Law, is dependent on the magnitude of the relative permeability ($k_{r,w}$):

$$Q_w = -kA\frac{k_{r,w}}{\mu_w}(\frac{dP}{dz} - \rho_w g \sin\phi) \qquad (6.1.3.3)$$

where k is the absolute permeability, A is the cross-sectional area available for flow, μ is the viscosity of the water, ρ is the density, dP/dz is the pressure gradient, g is the acceleration of gravity, and ϕ is the angle of inclination. Therefore, one can infer from equation (6.1.4.3) that Q_{in} and Q_{out} should change as $k_{r,w}$ (and water saturation) changes in the top and bottom sections, respectively. Measurements of the change in saturation in these sections should be performed in future experiments to determine the relationship between the saturation and the time interval between snapping events. Geller et al. (1996) conducted a parallel plate experiment where the top and bottom sections were fully saturated throughout the experiment. This experiment produced constant time intervals between the snapping events, again suggesting that changes in saturation in the top and/or bottom control the variations in time intervals between the snapping events.

Temperature may have also played a role in the variability of the time interval between snapping events. The apparatus for these experiments was not insulated from the room temperature fluctuations. The viscosity of water varies by approximately 7% for the range of temperature variations measured in the room (20-23°C). Changes in the surface tension and density of water are not as significant for this range of temperatures (~1% and 0.1%, respectively). Evaporation may also become more important as the temperature increases. The time interval between snapping events would decrease if evaporation became significant.

6.1.3 Flow intermittence in controlled aperture seqeunce cells

Summary and Conclusions

Parallel plate experiments with a medium-large-small aperture sequence were conducted to quantitatively investigate the intermittent flow behavior for a range of flow rates (8-24 mL/hr) and two angles of inclination, 58° and 70°. This geometry produced a liquid thread in the middle section that went through cycles of snapping and reforming. Three types of thread formation patterns were observed as a function of flow rate. At the lowest flow rates, a thread formed in the middle section and snapped before reaching the bottom section with the small aperture. At intermediate flow rates, the thread reached the bottom section, remained connected for some time, then snapped and reformed. At higher flow rates a stable thread formed. The flow rate required to maintain a stable thread was greater at the higher angle of the inclination. More detailed experiments were performed for the intermediate flow rates since this was the pattern of thread formation observed in the fracture replica experiments.

The frequency of the snapping events was examined by performing a linear regression on the time data where the threads were recorded to snap. The data points grew almost linearly for all the cases, suggesting that to a first order, the snapping events occurred periodically. In many of the plots, the data points deviated from the straight line in a repetitive pattern, indicating that more than one frequency of snapping events may exist at a particular flow rate. Fourier analysis can be performed on this data to determine the magnitude of possible additional frequencies.

Flow rates of thread formation and drainage were calculated at discrete time intervals from an analysis of the video images. The average time for the thread to drain before snapping increased as the flow rate increased (Table 6.1.3.1) and was also larger at 58° compared to 70° for the same applied flow rates due to the decrease in the magnitude of the gravitational force. The flow rates of the thread entering and draining from the middle section were only measured for the experiments conducted at 58°. The drainage flow rates that could be measured were approximately the same for all of the threads analyzed at $Q = 8.8$ and 10.6 mL/hr, but changed over time for the threads analyzed at $Q = 11.8$ mL/hr. The data suggests that changes in the liquid storage in the top and bottom sections of the plates drives the erratic nature of the thread

snapping. Temperature fluctuations in the room could have also contributed to the variations in the time interval between snapping events.

Intermittent flow behavior also occurred when non-aqueous phase liquids (NAPLs) were introduced into the fracture replicas (Section 6.2). Investigating NAPLs in the parallel plates will be important for understanding how changes in the chemical and physical properties of liquids affect the time intervals between the snapping events.
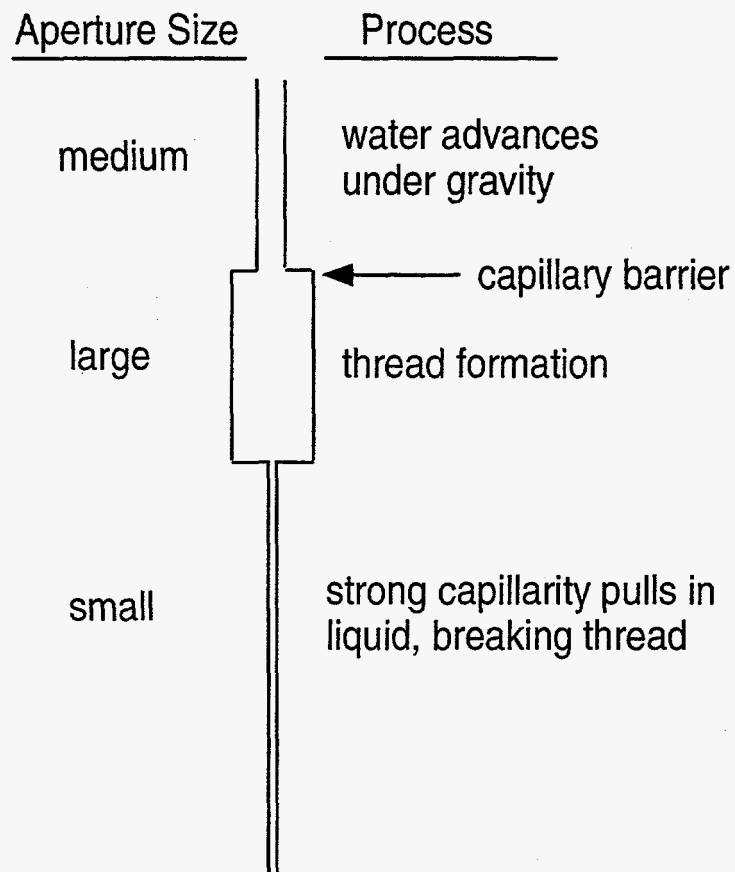
Aperture Size   Process

medium   water advances
                     under gravity

                                  ◄———— capillary barrier

large   thread formation

small   strong capillarity pulls in
                     liquid, breaking thread

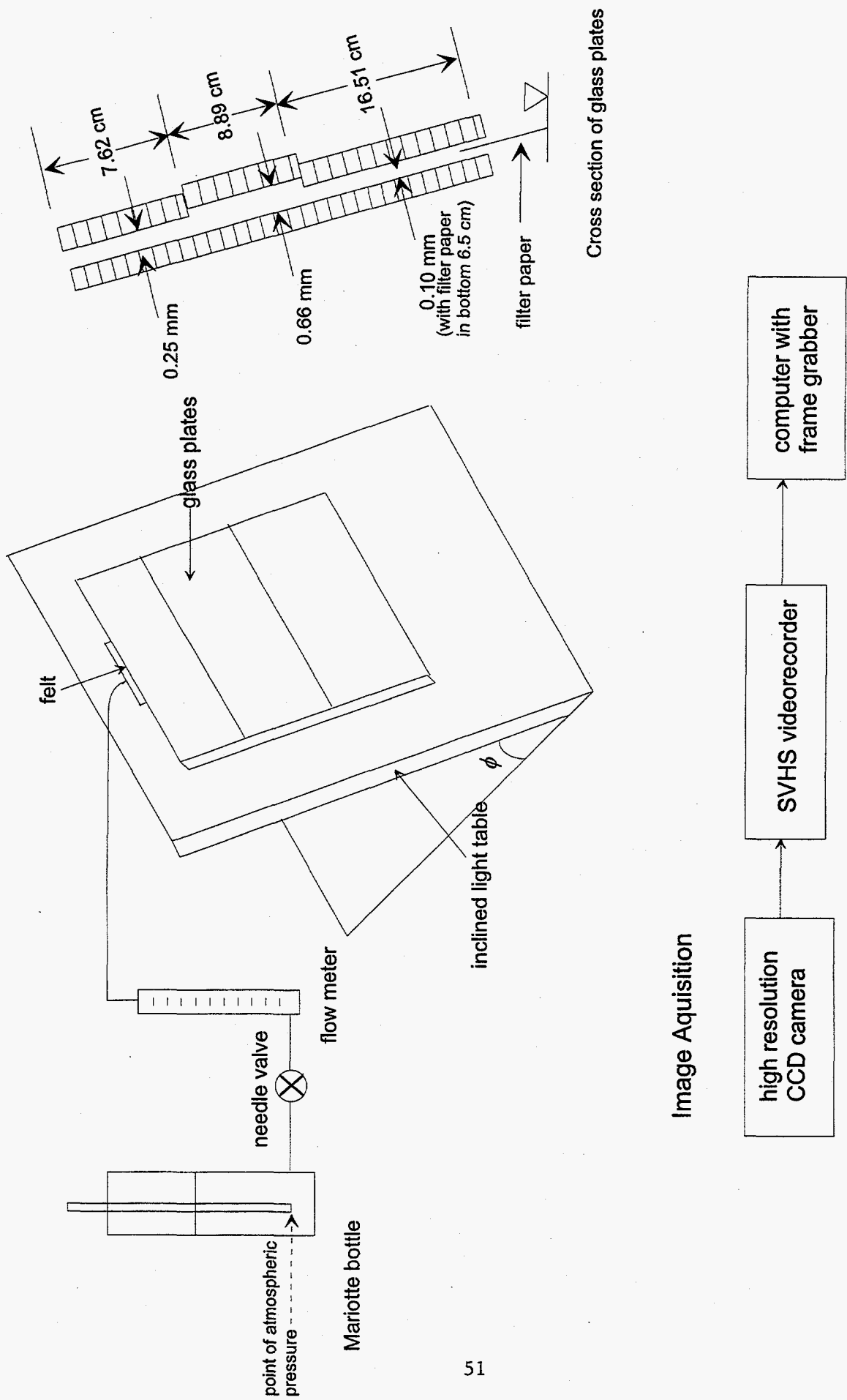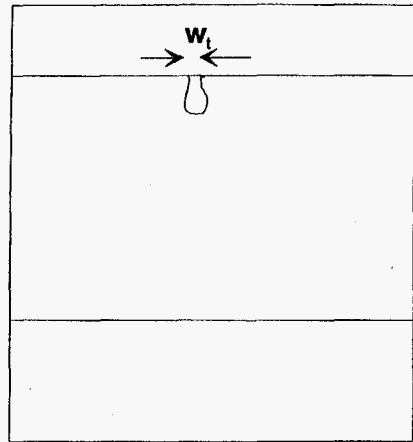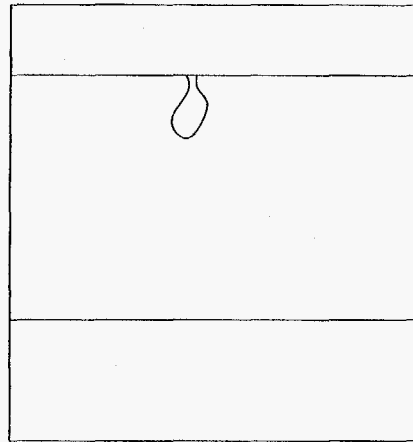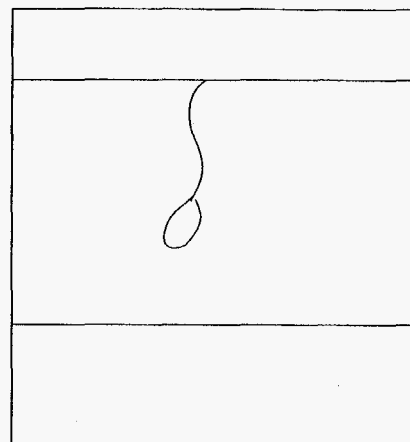Figure 6.1.3.1 Aperture sequence hypothesized as giving rise to flow intermittency.

Figure 6.1.3.2: Schematic of Apparatus for Parallel Plate Experiments

advancing front or "head" of thread

formation of "tail" of thread behind the advancing front

thread advancing in middle section

thread reaches the bottom of the middle section

$dt_{interface}$

increasing time
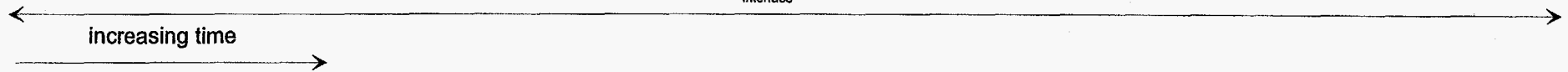
thread reaches the bottom of the middle section
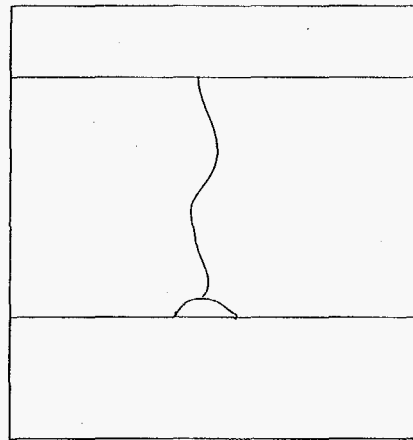
head of thread draining into the bottom section
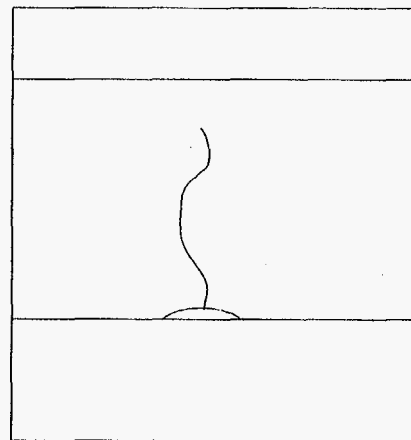
thread snaps at top of the middle section

$dt = dt_{interface} + dt_{drain}$

dt_{drain}

increasing time

Figure 6.1.3.3: Various stages of thread formation to snapping and definitions of the different time intervals
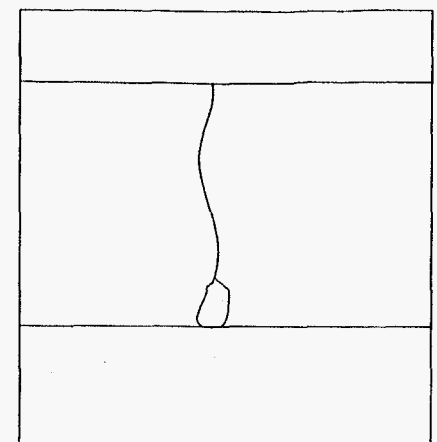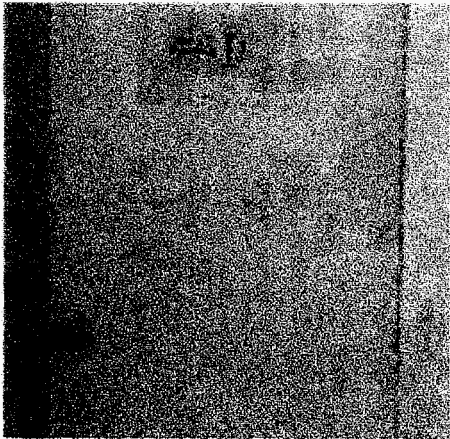
(a) formation of advancing
front or "head" of the thread
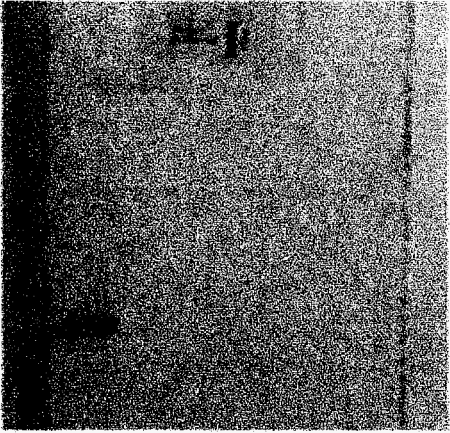
(b) formation of "tail" of thread
behind the advancing front
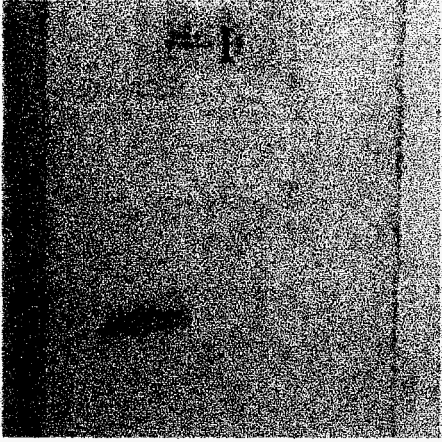
(c) thread advancing in
the middle section

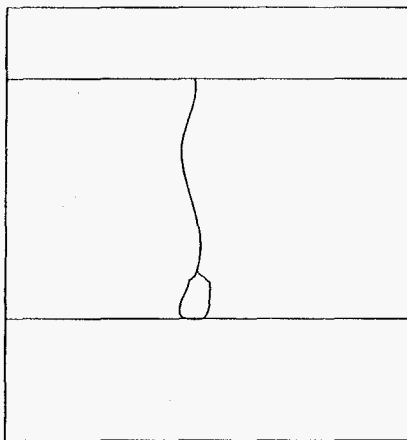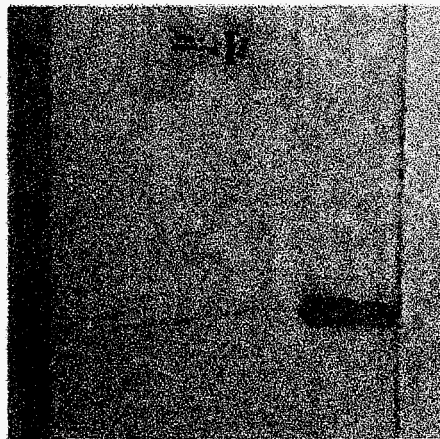(d) thread reaching bottom
of the middle section
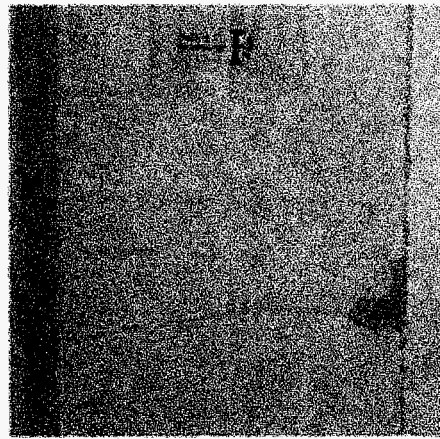
(d) head of thread draining
in the bottom section
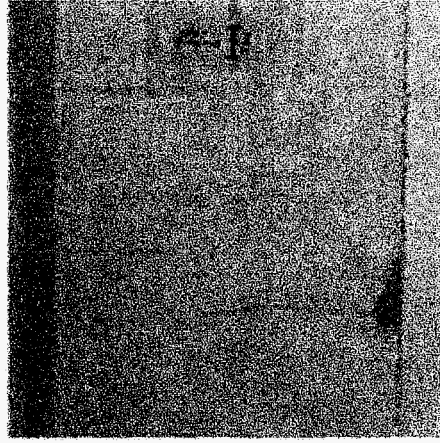
(f) thread snapping at the
top of the middle section

Figure 6.1.3.4: Various stages of thread formation to snapping

53
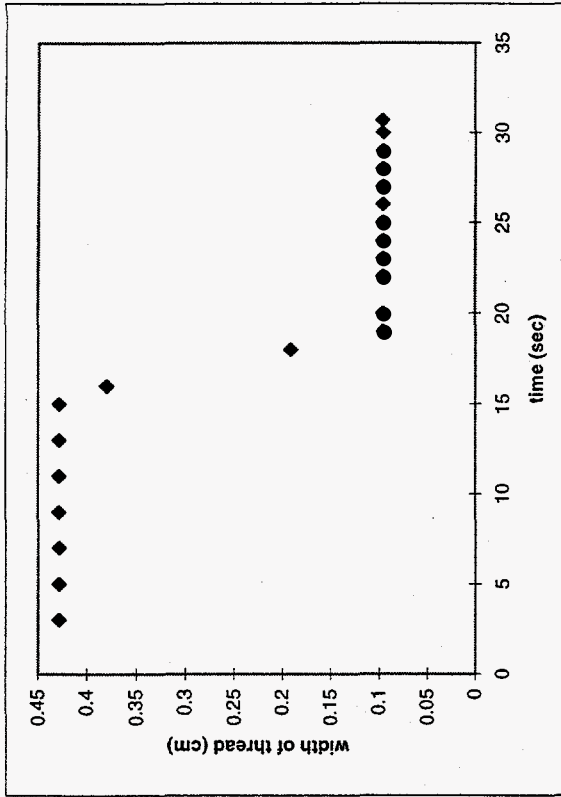
(a) θ = 58; Q = 11.7 ml/hr
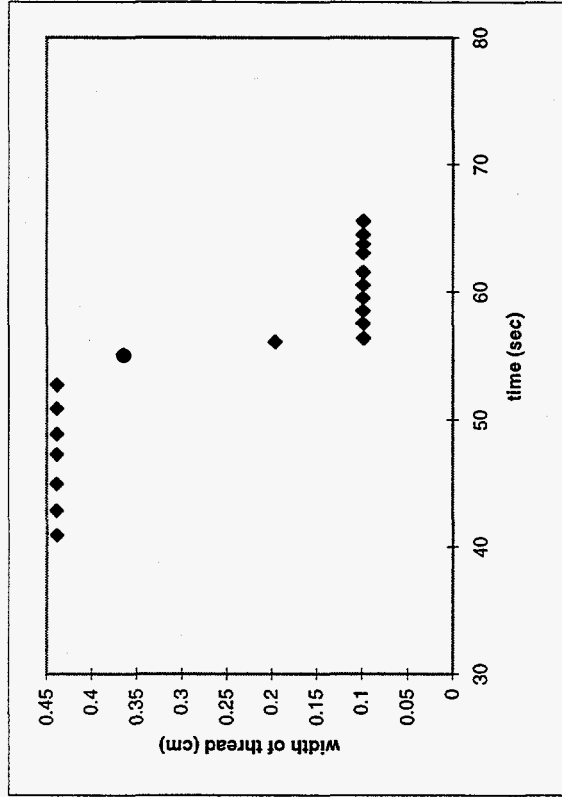
(b) θ = 70; Q = 8.6 ml/hr
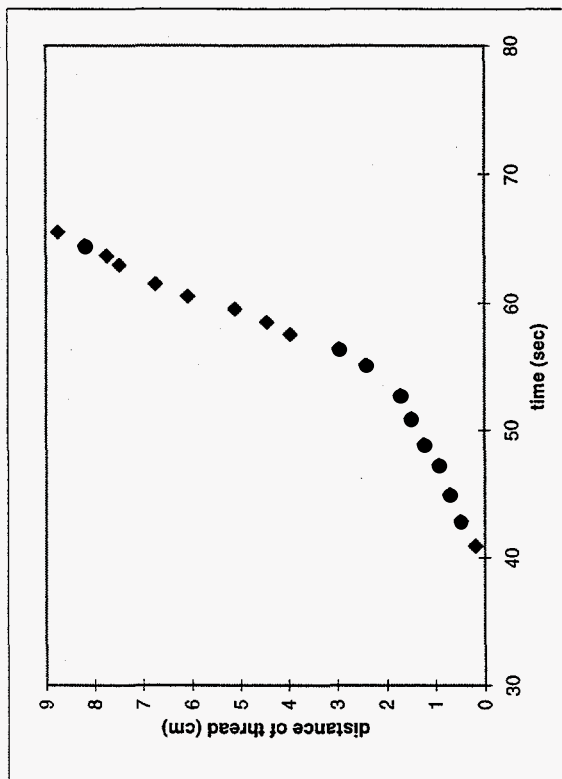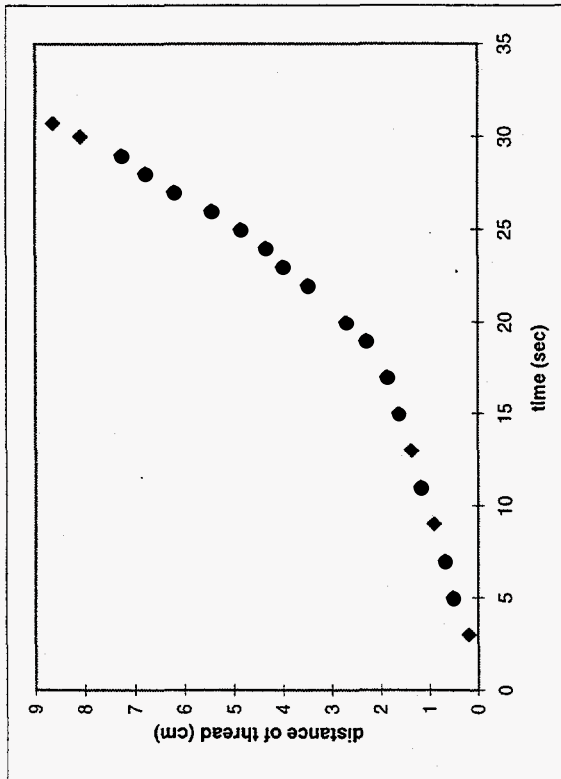
Figure 6.1.3.5: Distance as a function of time for a thread entering the middle section

54

(a) Q = 8.8 ml/hr

y = 0.7123x + 0.6233
R² = 0.9855

(b) Q = 10.6 ml/hr

y = 0.6592x + 1.2456
R² = 0.9914

(c) 11.7 ml/hr

y = 0.68892x + 2.6394
R² = 0.9863
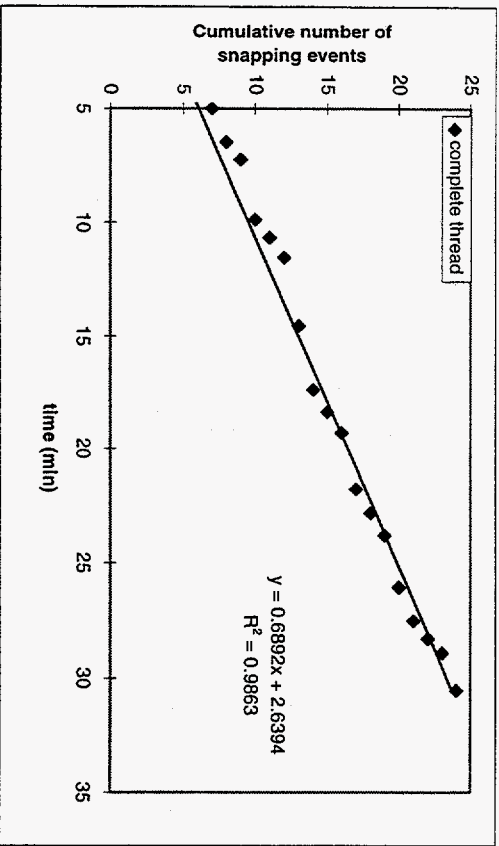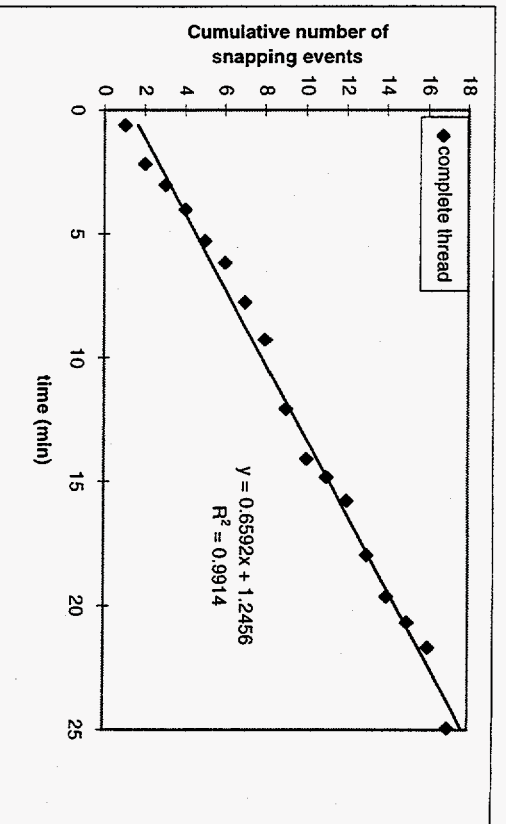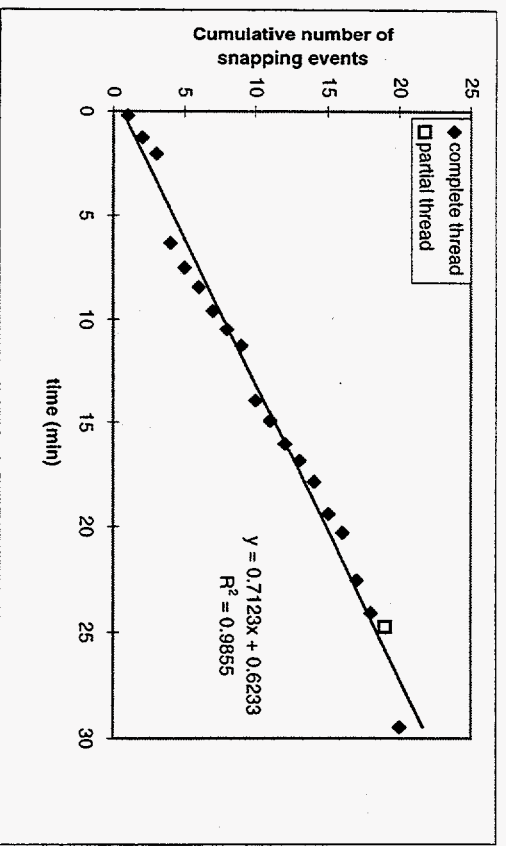
Figure 6.1.3.6: Frequency of thread-snapping, θ = 58°

(a) Q = 8.6 ml/hr

y = 1.3999x + 0.4094
R² = 0.9993

(b) Q = 10.1 ml/hr

y = 1.3835x + 0.8218
R² = 0.999

(c) Q = 14.5 ml/hr

y = 1.0694x + 1.8127
R² = 0.9923

(d) Q = 23.7 ml/hr

y = 0.8862x - 0.6169
R² = 0.9841
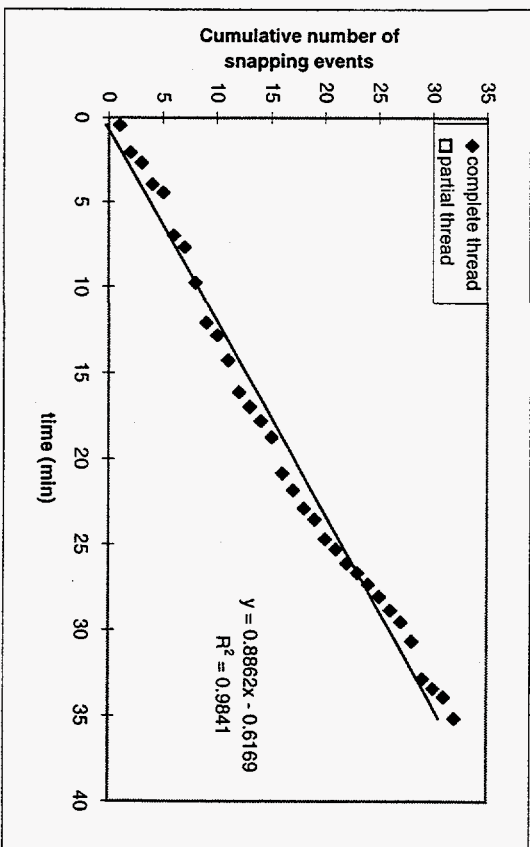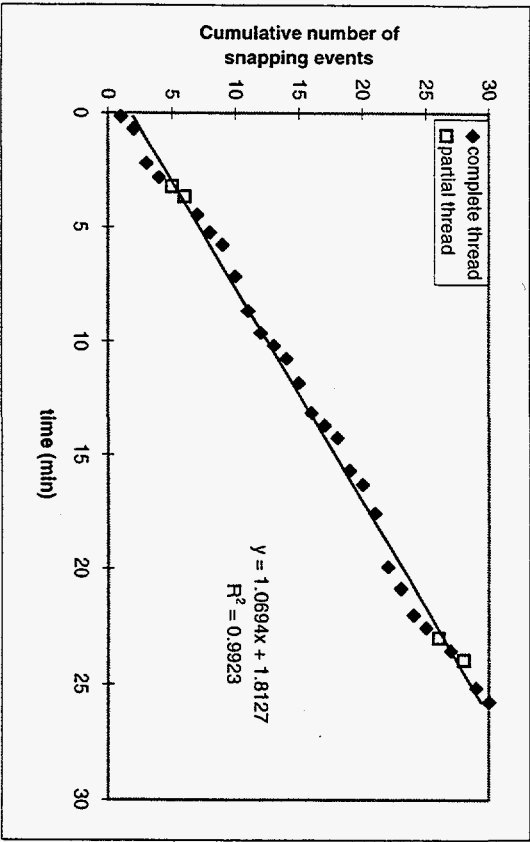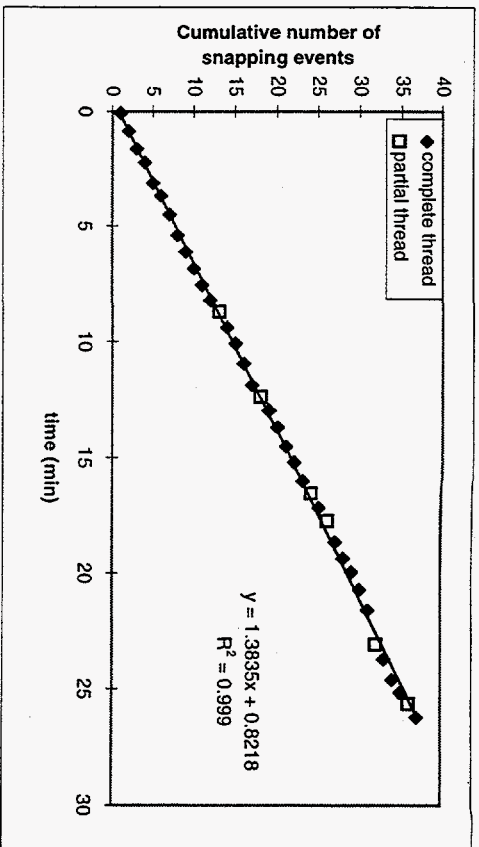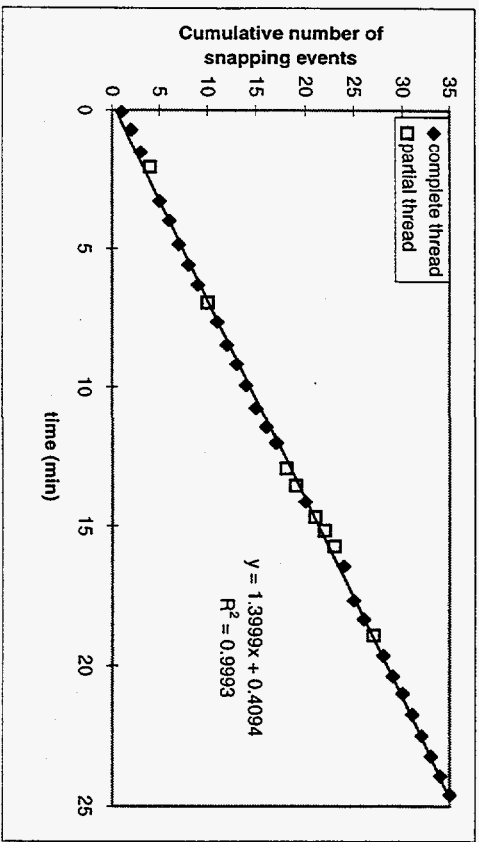
Figure 6.1.3.7: Frequency of thread-snapping, θ = 70°
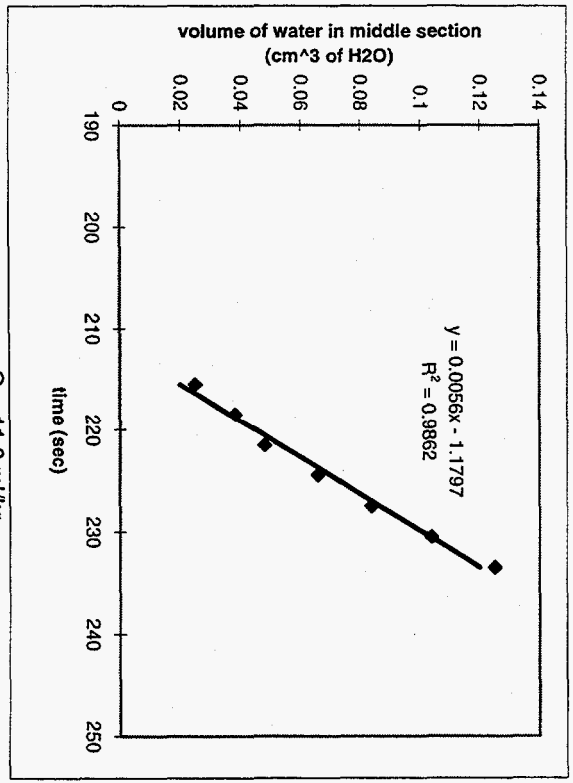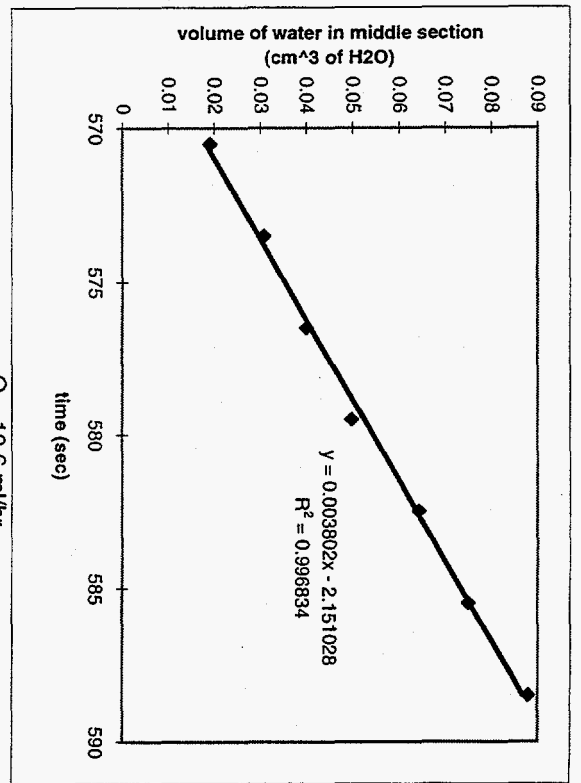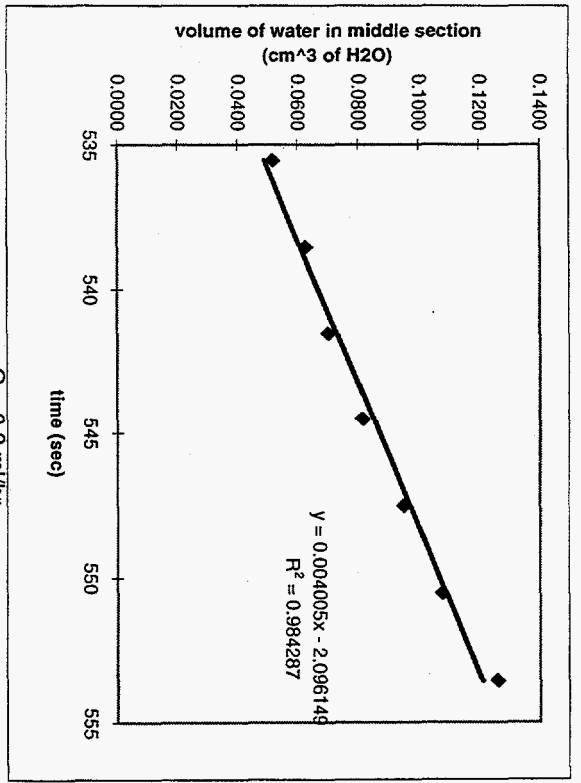
Figure 6.1.3.8: Change in volume of the thread entering the middle section over time (Q_{in}), $\theta = 58°$
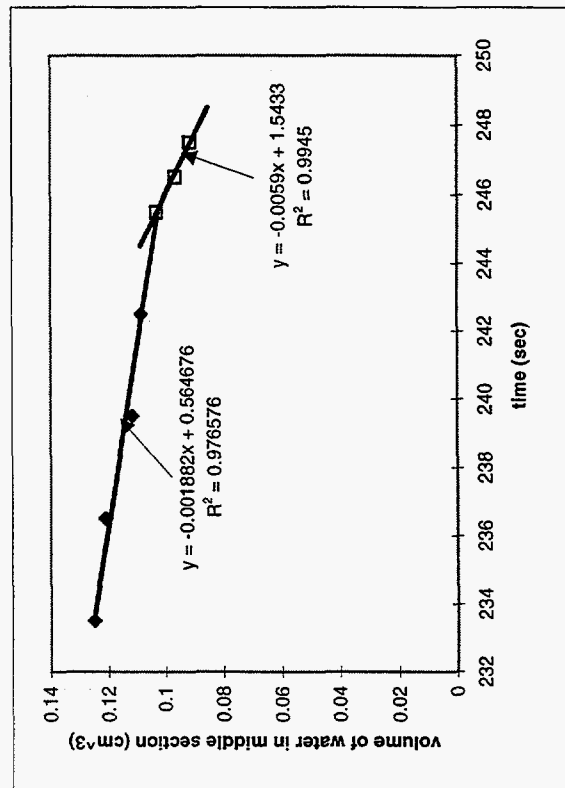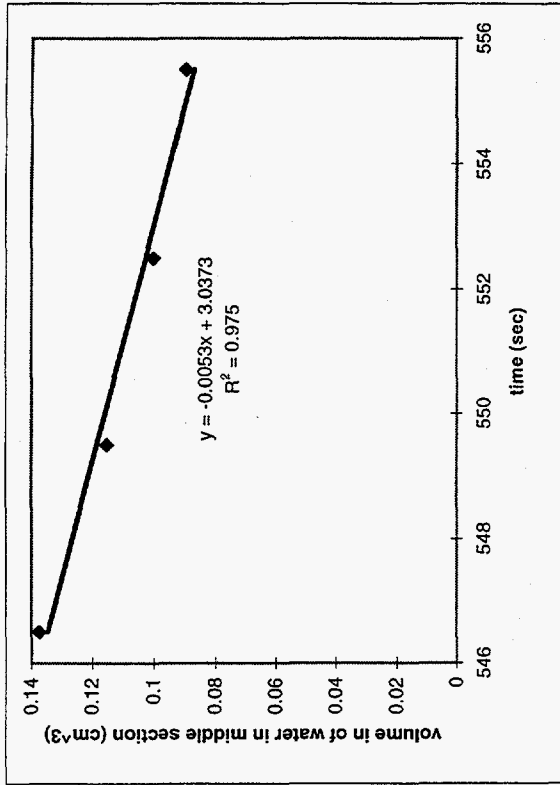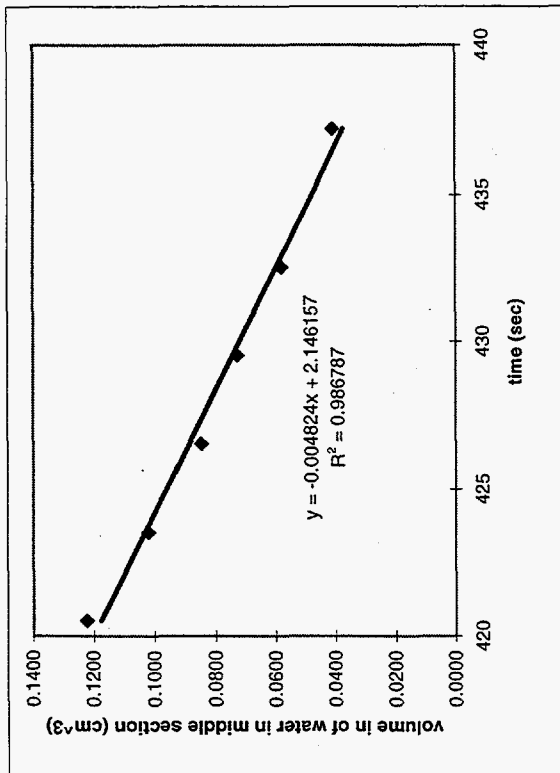
Figure 6.1.3.9: Change in storage of the water in the middle section for one thread at each flow rate, $\theta = 58°$

top of middle section

t1 →

Qin

change in the volume
of water (dV) over time (t)

t2 →

bottom of middle section

Qout = 0

Qin = dV/dt
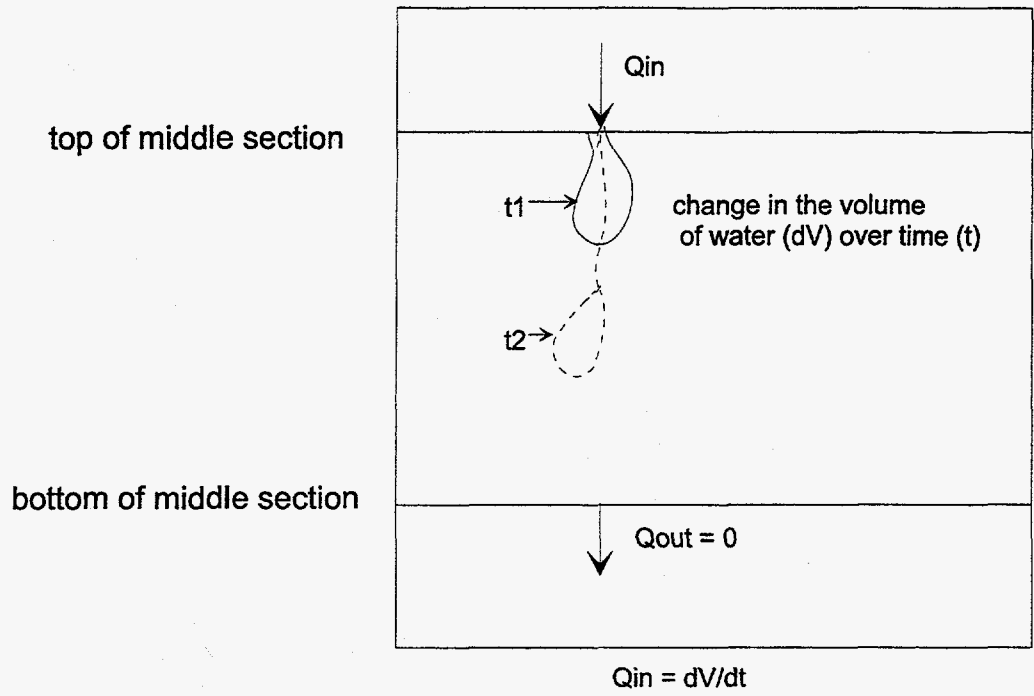
(a) Flow rate of thread entering the middle section

top of middle section

Qin

change in the volume
of water (dV) over time (t)

t3

t4

bottom of middle section

Qout

dV/dt = Qin - Qout
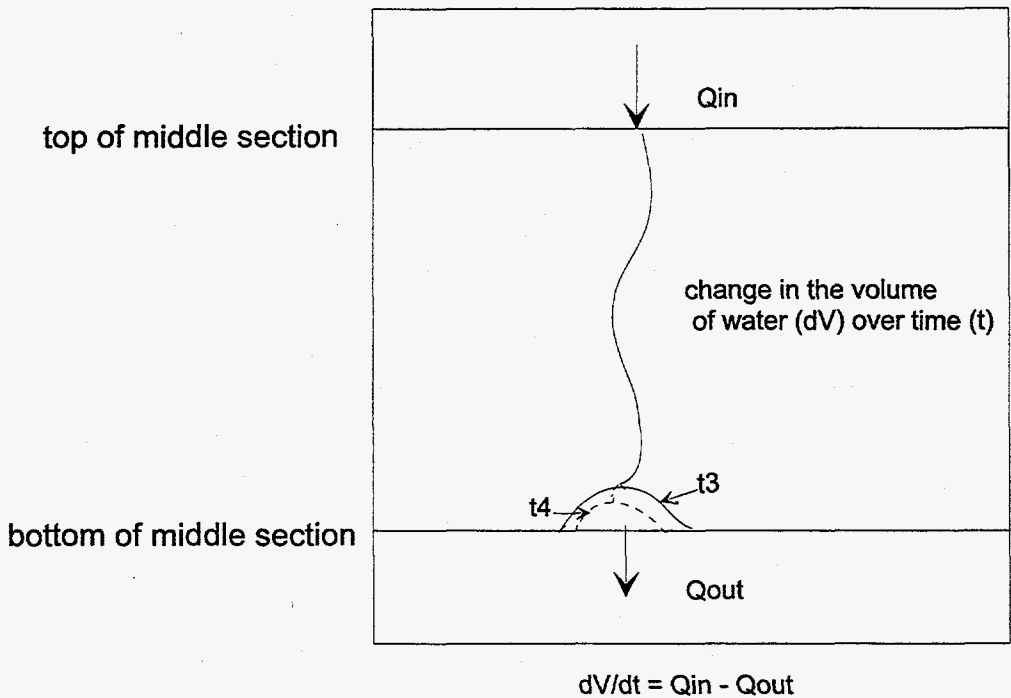
(b) Mass balance across the middle plates used to calculate the drainage flow rate

Figure 6.1.3.10: Definitions of the flow rates measured for
the thread entering and draining from the middle section

6.1.4 Seepage in rock-replica combination

(J. T. Geller, lead author)

While transparent replicas provide an accurate reproduction of the fracture surface topography, they do not reproduce the surface chemistry or matrix permeability of the real rock. A flow cell with one half rock and one half transparent replica may provide a useful compromise, allowing visualization of the flow in the fracture and a realistic fracture aperture field with the rock properties. In particular, flow behavior in fractures in the vesicular basalt, with its higher matrix permeability and extremely rough surface, may not be well-represented by flow through an impermeable fracture replica.

An epoxy replica was made from one side of a fractured vesicular basalt sample, from the SDA, 76-2 borehole, at approximately 19.5 m bls. Figure 6.1.4.1(a) is a photograph of the silicone replica mold and the fracture. Due to its orientation, (approximately 40° from the core axis) this fracture was probably created during core-drilling of the sample and is not a natural fracture. The silicone pulled away from most of the vesicles intersecting the fracture plane, however a few knobs were torn off when removing the mold from the rock. The replica was mated with the second half of the rock that had not been contaminated with silicone and water was delivered to the fracture with a capillary siphon connected to a beaker of water, shown in Figure 6.1.4.1(b). The water level in the beaker was 2 cm below the top of the fracture. The assembly was oriented such that the fracture was inclined at a 50° angle measured from horizontal. Water was periodically added to the beaker to maintain a constant water level, and this volume was recorded. A piece of filter paper was placed between the rock and replica on the down-gradient end of the fracture to collect water flowing from the fracture. The rock sat on a petri dish to collect any water flowing through the rock matrix. The water-beaker and filter siphons were covered with plastic to reduce evaporation losses. The rock was initially air-dry and the fracture surface was not treated in any way.

The record of cumulative water additions and fracture and rock matrix outflow during the course of this experiment is plotted in Figure 6.1.4.2. During one week, 75 mL of water were imbibed into the rock, but no water reached the outlet. The movement of clear water through the replica was not visible, however the top half of the fracture appeared wet. Over the next 24 hours, 6 mL were imbibed into the rock, and no water flowed out the bottom. The angle of the fracture was raised to 70°. Several hours later,

60

6.1.4 Seepage in rock-replica combination

isolated liquid segments were visible through the replica. The volume of water imbibed into the fracture over the next 24 hours greatly increased by 38 mL, but still no water reached the outlet. Under these conditions, the water migrated through the rock matrix and evaporated out the core wall. Water staining was observed on the core walls near the fracture surface. The replica was removed and the fracture surface appeared saturated with water ponding in the vesicles. The outside edges of the fracture surface were dry.

To prevent evaporation of water out the sides of the fracture, the core wall was covered with a latex membrane, the replica was repositioned on the fracture surface, and the fracture inclination angle was 66° measured from horizontal. About ten hours later, water began to flow out the bottom of the fracture, but the flow paths in the plane of the fracture could not be seen through the replica. The core walls under the latex membrane were wet. Over the next week, the volume of liquid flowing through the fracture and through the rock matrix was monitored daily.

The values in Figure 6.1.6.3 should be interpreted relative to the sample pore volume. This, as well as matrix permeability will be measured, however an estimate of the pore volume is 300 mL, based on estimates of the bulk volume of the rock sample from its outside dimensions (730 cm^3) and a porosity of 0.4. It is not known what fraction of the total porosity is actually connected. Until the point at which the sample was covered by latex, evaporation losses were significant. A minimum bulk water-saturation value of 47% of the pore space is estimated from the accumulated water additions from the point at which the sample was covered by latex, minus the accumulated volume of water out the fracture and rock. This shows that fracture flow did occur before the rock matrix was fully saturated. For the non-vertical angle of inclination, gravity drove water into the rock matrix. Less matrix flow is expected at higher angles of inclination.

The replica of the vesicular basalt proved to be of limited use for flow visualization for the non-vertical fracture inclination and vesicular rock matrix. This is because the openings between the rock and the replica, or apertures, must be saturated with water in order to see a change in light transmission and reflectivity that permits discrimination between the water-occupied and air-occupied regions. Some of the apertures did fill when the fracture was inclined at its highest angle of 70°. However, once the angle was slightly reduced, fracture flow occurred for partial saturation of the rock-replica apertures. This experiment should be repeated for near-vertical inclinations of the fracture, as well as some

6.1.4 Seepage in rock-replica combination

control on matrix saturation. Rock-replica combinations for flow visualization should be more useful in fractures occurring in dense basalt having very low matrix permeability. Finally, after experimentation in the rock samples, measurement of the fracture topography and aperture distribution using light attenuation through the replicas of the fracture surfaces may provide parameters that can be used to characterize flow in the fractures themselves.
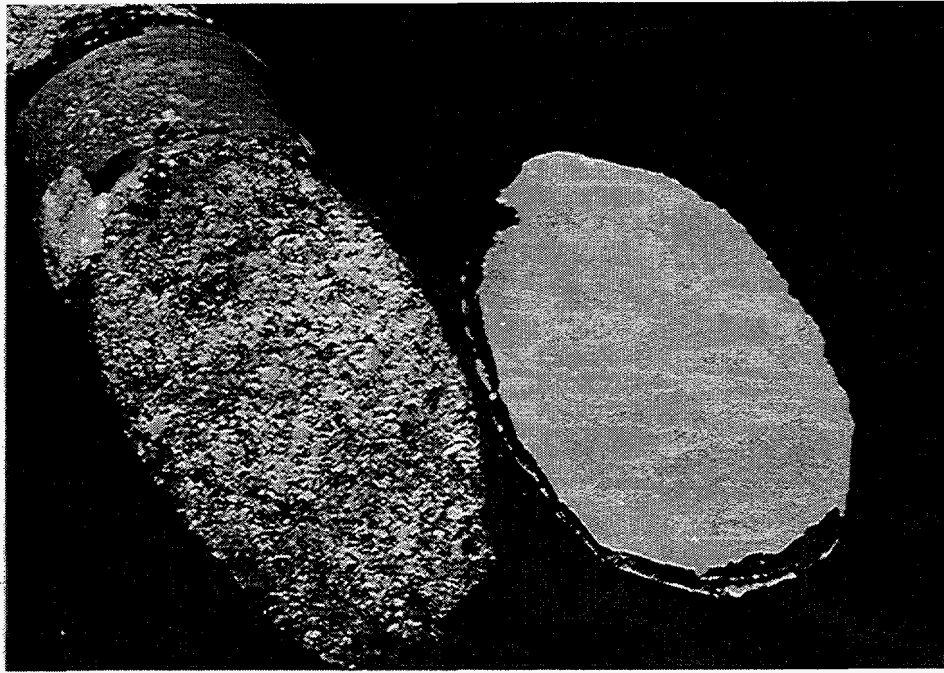
(a)
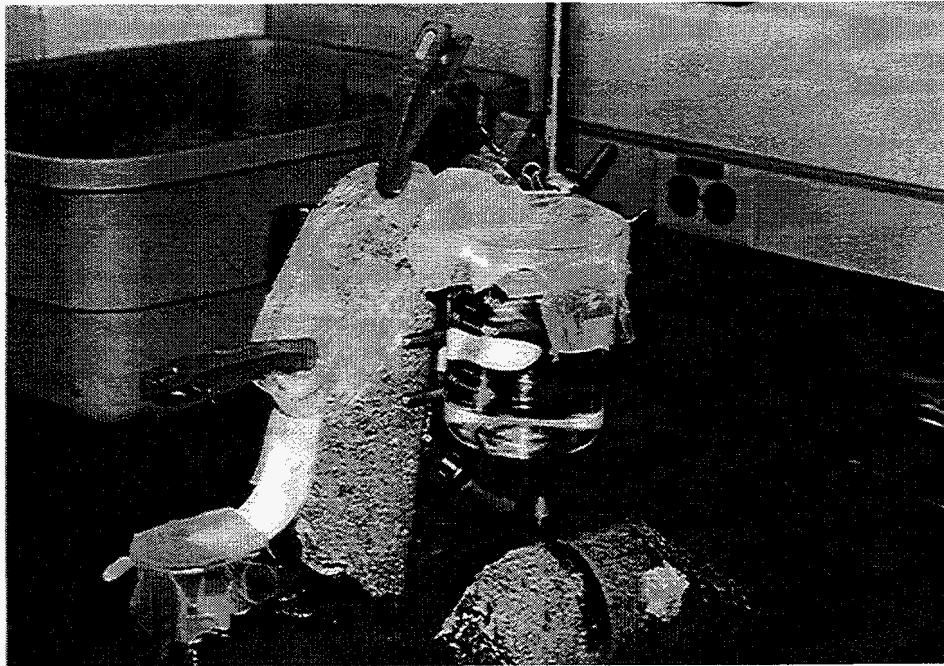
(b)

Figure 6.1.4.1 Rock-replica experimental set-up (a) epoxy cast and fracture surface (b) rock-replica arrangment with capillary siphon from glass beaker to deliver water to fracture, filter paper at bottom to collect water flowing through fracture.
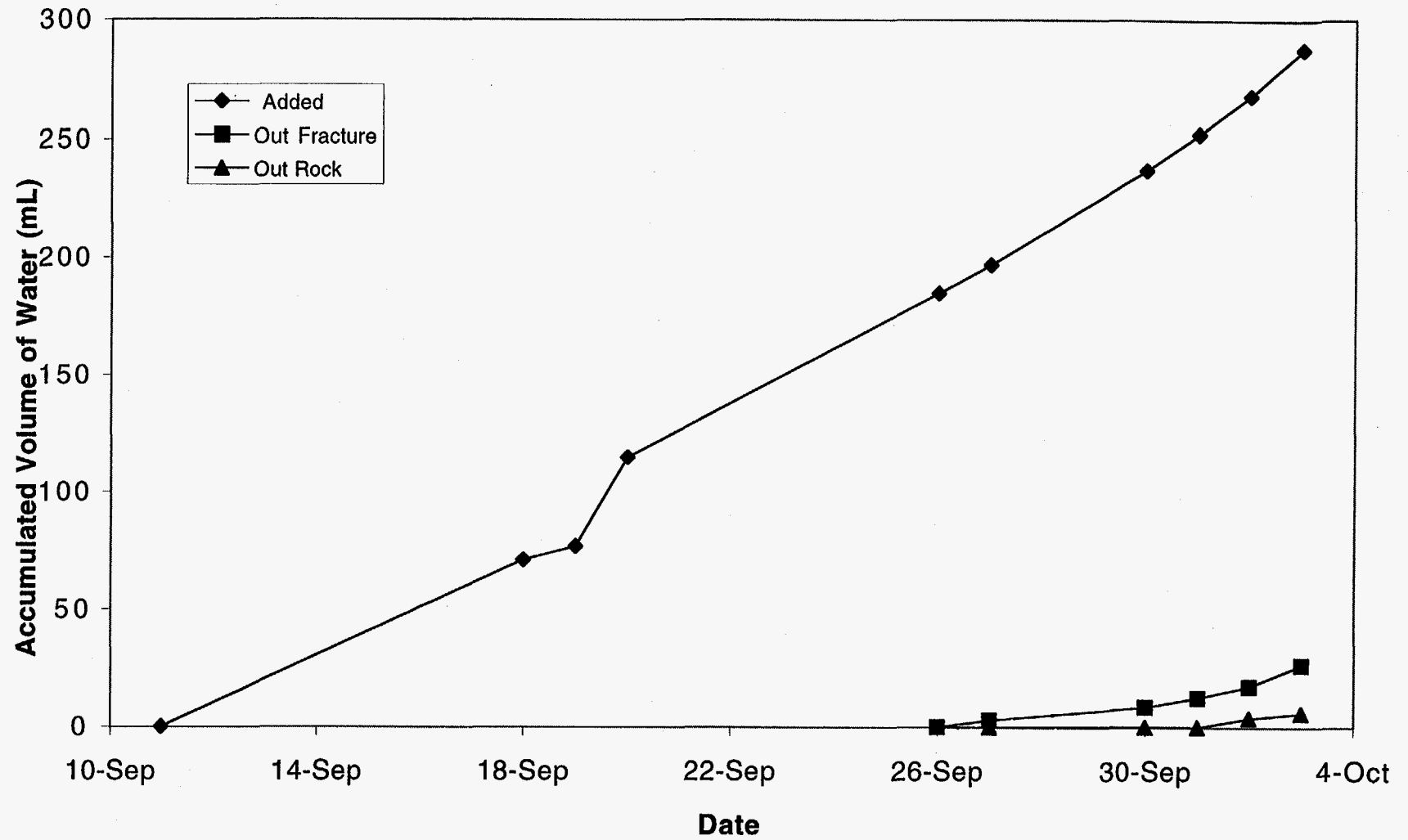
Figure 6.1.4.2   Water flow through fractured basalt w/ replica

6.2. NAPL Infiltration into a Partially Saturated Rock Fracture

(G. Su and J. T. Geller, lead authors)

Flow visualization experiments of the infiltration of non-aqueous phase liquids (NAPLs) in a single fracture were conducted using an epoxy replica of a natural rough-walled granite fracture. These experiments were conducted to qualitatively investigate NAPL migration behavior in the presence of residual water and to provide a basis for designing future experiments. The physical and chemical properties of selected NAPLs are listed in Table 6.2.1. The NAPLs used in the preliminary experiments reported here are n-dodecane and trichloro-trifluoroethane (Freon 113). These two liquids were chosen because of their contrast in density, viscosity and vapor pressure. n-Dodecane is less dense and more viscous than water and has a relatively low vapor pressure, while Freon 113 is denser and less viscous than water and has a high vapor pressure. Additionally, n-dodecane has negative spreading coefficient, while Freon 113 has a positive spreading coefficient. NAPLs with positive spreading coefficients have been observed to spontaneously spread along the air-water interface, which will greatly reduce the volume of trapped NAPL as well as its residence time, thereby allowing a NAPL to migrate a much greater distance (Blunt et al., 1994). This spreading is expected to greatly enhance mass transfer of NAPL components to the aqueous and vapor phases by increasing the surface area of contact between the fluid phases. The spreading coefficients calculated in Table 6.2.1 show that a range of spreading behavior can be expected for common NAPL contaminants. Generally speaking, the rigorous application of spreading coefficients is difficult, because the air-water surface tension changes as it is exposed to contamination. In the specific case of the following experiments, the presence of dye in both the water and NAPL should affect the spreading coefficients. Other NAPLs that are chemically compatible with the epoxy replicas and will be used in future experiments include n-octane, carbon tetrachloride and tetrachloroethene (PCE).

General

The fracture replica, assembly and data acquisition are as described in Section 6.1.1. The replica assembly was inclined to an angle of 70° from the horizontal. The water was dyed with 0.4% Liquitint and the NAPLs were dyed with Automate Red B (Morton Thiokol, Inc., Chicago, IL). After introducing water into the fracture as in Section 6.1.1, and flow channels developed over several days, the water supply was discontinued and the fracture was allowed to drain to residual saturation at atmospheric pressure. Three mL of NAPL were manually injected through the grooves in the endcap (Figure 6.1.1.3) with a syringe. In the first experiment, conducted with n-dodecane, the n-dodecane took 24 hours to attain residual saturation. Subsequently, water was delivered to the fracture to observe the effect on the residual n-dodecane. In the second experiment with Freon 113, the NAPL quickly volatilized and there was no residual NAPL. A repeat of the Freon 113 injection with the fracture sides sealed had no effect on the rapid volatilization of the NAPL.

Following is a narrative of the specific procedures of each experiment and our observations.

Experiment with n-dodecane as the NAPL

The residual water saturation was established by introducing water to the fracture as in Section 6.1.1 for h_w = 3.8 cm, where h_w is the elevation of the fracture inlet relative to the point of atmospheric pressure in the Mariotte bottle (see Figure 6.1.1.1). Two flow channels formed in the middle of the fracture. Water supply to the fracture was discontinued after three days, and the fracture drained for about 2.5 hours. The resultant water distribution is shown in Figure 6.2.1 (a).

On Day #1 of the experiment, 3 mL of n-dodecane was injected manually into the grooves of the ceramic end-cap in a repetitive pattern at three points along the inlet plate, the left edge, middle, and right edge, over a period of approximately 14 minutes. After approximately 1.5 minutes, the n-dodecane entered the fracture from the left side of the

endcap in a region where there was no residual water (Figure 6.2.2(a)). Two minutes after injection, n-dodecane flowed through the middle of the fracture and coated the left outer edge of the continuous region of residual water near the inlet (Figure 6.2.2(b)). Three minutes after injecting the n-dodecane, it began to flow from the right edge of the endcap and flowed along the right edge of the continuous region of residual water (Figure 6.2.2(c)).

The left n-dodecane channel completely formed in an initially air filled region after about 3.5 minutes. This channel has similar features to the types of channels of flowing water, described in Section 6.1.1. Broader regions of n-dodecane are connected by thinner threads. Intermittent flow also occurred frequently in these flow channels and at a faster rate than what was observed for flowing water. A film of n-dodecane spread around the flow path and appeared pink on the epoxy replica. The formation of this film indicates the strong wettability of the epoxy to n-dodecane.

The n-dodecane which flowed from the middle of the fracture inlet did not form a complete flow channel as it became entrapped in the residual water (Figure 6.2.3(a)). Most of the n-dodecane in the middle accumulated along the air-water interfaces near the top of the fracture. A small portion of it also migrated about half way down the original left water channel, where it become entrapped by the residual water.

The right n-dodecane channel formed along the right edge of the large region of residual water near the inlet and then began to flow through a dry region located immediately to the right of the original right-hand water channel for a distance of about 10 cm. The n-dodecane then entered the original water channel and continued to flow along this path until it became entrapped by small segments of residual water near the bottom of the fracture (Figure 6.2.3(b)). As n-dodecane accumulated in these residual regions, it then began to drain out of the fracture. A film of n-dodecane quickly spread around this flow path and the liquid flowed in an intermittent manner.

The n-dodecane initially appeared to bypass the regions of ponded residual water near the top, but after approximately an hour after it was injected, the n-dodecane began

to displace some of this residual water. A small slug of water flowed through the original left water channel as it was displaced by the n-dodecane. Figure 6.2.4 is a comparison of the water and n-dodecane distributions during various stages of the experiment. The n-dodecane was allowed to drain overnight and reach residual saturation.

By Day #2, a film of n-dodecane had spread throughout much of the fracture. Some water near the inlet was displaced by n-dodecane (Figure 6.2.5(a)). The n-dodecane which had been entrapped in the residual water near the bottom of the fracture had also drained out of the fracture overnight (Figure 6.2.5(b)).

The point of atmospheric pressure in the Mariotte bottle was set to 4.8 cm above the fracture inlet elevation to deliver water to the fracture. After approximately 4 minutes, water broke through on the left side of the inlet edge and proceeded through the original the left water channel. As the water encountered the residual n-dodecane, it flowed around the n-dodecane blobs. The resultant water/n-dodecane mixture had water interspersed with small blobs of n-dodecane inside and along the edges of the water (Figure 6.2.6). After approximately 30 minutes, water also began to flow through the original right-hand flow channel. The water only flowed a short distance through this channel, at which point a slug of water broke off and was trapped one third of the way down from the top of the fracture. At the end of the day, the Mariotte bottle was lowered by 1.8 cm and water continued to flow through the fracture several days.

On Day #3 of the experiment, some of the residual n-dodecane entrapped near the top of the fracture had been displaced by the water (Figure 6.2.7). Three days later (Day #6) much more of the residual NAPL had either been displaced by the water or had drained out of the fracture. A region of residual n-dodecane at the top left of the fracture which was not in contact with the flowing water was no longer present after three days. The vapor pressure of n-dodecane is quite low, which suggests that the disappearance of the n-dodecane in this region was probably the result of it draining out and not volatilization. The amount of residual n-dodecane on Day #6 did not change significantly from Day #3, except for a small portion of n-dodecane that was displaced in the region

immediately below the middle of the inlet. Figure 6.2.8 is a comparison of the water/n-dodecane distribution at various times and days after water was reintroduced into the fracture.

Experiment with Freon 113 as NAPL

The fracture replica from the previous experiment was disassembled and cleaned. To remove staining by the red dye, it was soaked in a Liqui-Nox® solution, followed by an application of Clorox® bleach, then additional soaking, rinsed in distilled water and wiped with methanol. After most of the red dye had been removed, the fracture was reassembled as before. Water was introduced to the fracture at $h_w = 4.8$ cm. One channel formed from the left side of the ceramic endcap. A channel has not formed in this area of the fracture in previous experiments. This may be the result of differences in the way the fracture was reassembled, in the fracture/endcap coupling, or surface chemistry changes. Water supply to the fracture was discontinued after three days, after which the water was allowed to drain for approximately two hours. Figure 6.2.1(b) is the water distribution in the fracture after drainage.

Freon 113 was then introduced into the fracture in the same manner as the n-dodecane over a period of approximately 7 minutes. The Freon broke through almost immediately from left side of endcap where it was injected first (Figure 6.2.9(a)). About 30 seconds later a channel on the right side broke through, corresponding to the time when the Freon 113 was first injected on that side (Figure 6.2.9(b)). The left channel took about 5.25 minutes to reach the outlet of the fracture, and the other channel took a total of approximately 4.5 minutes to reach the outlet of the fracture. The left channel took longer to reach the outlet of the fracture even though it started to form first because the Freon 113 became entrapped in residual segments of water near the bottom of the fracture before it drained out. A third channel located immediately to the right of the second channel began to form 4.5 minutes after the experiment began (Figure 6.2.9(c)). This channel reached the outlet approximately 1 minute later.

The appearance of Freon 113 flowing through the fracture was much different than what was observed using water or n-dodecane. Instead of forming continuous or partially continuous channels, the Freon 113 generally proceeded in an unsteady manner similar to guppies swimming in water. Droplets of Freon 113 with short tails quickly migrated through the fracture, occasionally becoming trapped at one or two points along the flow path. The coalescence of a flowing droplet of Freon with a trapped one typically caused the resulting drop to drain down the rest of the path. This observation suggests that gravity affected the capacity of the fracture to retain Freon 113. The high vapor pressure of Freon 113 resulted in the rapid volatilization of thin threads along the flow channel, preventing the formation of continuous or a partially continuous channels that occurred for flowing water.

A portion of the residual water at the top of the fracture was displaced by the Freon 113. The displaced water moved along a path approximately 1 cm to the right of the original water channel. After about 7 minutes, the displaced water was trapped in its new position in the fracture, shown in Figure 6.2.10. The Freon 113 also became entrapped near the bottom middle of the fracture where the fracture is slightly rougher and tighter. Some of the Freon 113 was diverted to the right along the sealed micro-fracture intersecting the open fracture plane near the bottom of the fracture before it drained out of it. This feature occurs in the original rock fracture and its effect on the fracture surface topography is reproduced in the replica.

The Freon 113 quickly spread as a film across the replica surface due to its strong affinity for the epoxy. This film of Freon 113 quickly evaporated due to the high vapor pressure of Freon 113. About 10 minutes after the experiment started, the film of Freon 113 in the middle of the fracture began to volatilize very rapidly. Figure 6.2.11 is a series of photographs at different times during the experiment which shows this rapid volatilization. The Freon 113 continued to flow through the fracture for approximately 20 minutes after the initial injection. Approximately an hour and a half after the initial injection, nearly all of the Freon 113 had volatilized.

Freon 113 was injected a second time (3 mL over 3 minutes) with the fracture sides sealed to see if this inhibited the rate of volatilization. The rate of volatilization did not noticeably change with the sides sealed. The region in the middle of the fracture again volatilized the fastest as was seen in the previous experiment. It appears that the top and bottom of the fracture may be providing the major air pathway that induces volatilization.

Summary

Our general observation is that residual water can enhance NAPL entrapment as well as divert the flow of NAPLs, resulting in a more disperse distribution than in a dry fracture. The presence of residual water enhanced the entrapment of n-dodecane as it migrated through the fracture, relative to regions where there was no water. Residual water also increased the entrapment of Freon 113, however, due to its high vapor pressure, residual blobs of Freon 113 volatilized relatively quickly. Freon 113 is a relatively common groundwater contaminant due to its widespread use, and there are likely to be situations where it does not readily evaporate as it migrates through the vadose zone. An example of these conditions is the penetration of Freon 113 into regions of locally ponded water where the presence of water-Freon interfaces retards the volatilization of Freon 113. Both the n-dodecane and Freon 113 formed flow channels which bypassed the water-saturated regions. Here, the degree of fracture roughness also appeared to affect NAPL trapping, which increased in rougher and tighter areas of the fracture.

The n-dodecane and Freon 113 proceeded in an unsteady manner through the flow channels that formed. The unsteady flow behavior observed when n-dodecane was used as the infiltrating liquid appeared similar to the intermittent flow of water described in Section 6.1.1. The unsteady flow behavior of Freon 113 was probably the result of the high vapor pressure of this liquid; however, the density and low viscosity could also be a factor in controlling this flow behavior.

In small aperture regions of the fracture, large capillary forces give rise to complex distributions of the liquid-liquid-vapor interfaces. In the initially air-dry fracture replica, flowing water gets trapped in the tighter regions of the fracture, in accordance with the aperture distribution measured in Section 6.1.3. As the NAPL enters the fracture, it is diverted from the tighter regions occupied by the residual water, flows along the water/air/solid contact and as a result gets trapped along water-air interfaces, as well as in small aperture regions that the flowing water did not encounter. After a period of time, some of the residual water is displaced by the NAPL adjacent to it since the NAPL has a stronger affinity for the epoxy surface than water. The NAPL also spreads as a film along the dry fracture surface. Subsequent water infiltration further complicates the distribution of liquid-liquid-vapor interfaces as it flows and becomes trapped along NAPL-air interfaces.

The infiltration behavior will differ in a strongly water-wetting media, as compared to the epoxy, which is of intermediate wettability to water (Geller et al., 1996). On dry surfaces, the flow of NAPLs may be similar on an epoxy compared to a strongly water-wetting surface, with the exception of the NAPL film spreading on the epoxy. In a strongly water wetting media, the viscous and gravity forces that may drive NAPLs into water-occupied regions are countered by capillary forces, resulting in a weaker net driving force for NAPL invasion of water-occupied regions. However, the complex co-mingling of the phases observed in the epoxy replica could occur in a sequence of water-NAPL-water infiltration events in a strongly water-wetted media. The NAPL could become trapped along the water-air interfaces created in the first infiltration event, as well as small aperture regions that the water did not flow through. If water in the third infiltration event is diverted to NAPL-filled apertures, capillary forces would eventually drive water into the smallest apertures.

The flow visualization experiments can help understand how the nature of entrapment of NAPLs in partially saturated fractures will affect abiotic and biotic degradation of the contaminant. Mass transfer from the NAPL to the aqueous and vapor

phases and locations where micro-organisms can thrive and potentially degrade the contaminant should be strongly dependent upon the distribution of all phase interfaces (liquid, vapor and solid).

74

Liquid	Density[c] (kg m^{-3})	Viscosity[c] (kPa s)	Liquid/water surface tension (mN m^{-1})	Air/liquid surface tension (mN m^{-1})	Spreading Coeff.[l] (mN m-1)	Vapor Pressure (mm Hg)	Solubility in water (mg L^{-1})	Reacts w/ epoxy?
Water	997	0.890	-	72		17.6 (20°C)	-	no
LNAPLs								
n-dodecane	745	1.378	52.8[f]	24.91[c]	-5.71	0.12	0.0037	no
n-octane	700 (20°C)	0.547 (20°C)	50.8[i]	21.1	0.1	14	0.66	no
iso-octane (2,2,4 trimethylpentane)	690 (20°C)	0.504 (20°C)	50.1[h]	18.8 (20°C)	3.1	49	2.4	not tested
hexane	687 (20°C)	0.2985	51.1[j]	18.4[j]	2.5	156[k]	9.6[k]	not tested
Kerosene[e] (C$_8$-C$_{16}$)	800 (15°)	1.152 (21°C)	47-49 (20°C)	23-32 (20°C)	n.a.	n.a.	n.a.	no
o-Xylene	880	0.81	36	30 (20°C)	6	6.6[i]	175	not tested
Toluene[b]	870	0.59	36	29	7	28.57[i]	540	yes
DNAPLs								
Freon 113 (trichloro-trifluoroethane)	1560[e]	0.711 (20°C)	37[g]	17.75[c] (20°C)	17.75	334	200	no
TCE	1460	0.59	35	28.8[c]	8.2	74[i]	1100	yes
TCA[b] (1,1,1 trichloroethane)	1310	0.83	45	25	2	123	720	yes
Carbon Tetrachloride	1584[c]	1.038[c] (15°C)	45[i]	26.15[c] / 27.04[j]	0.85 / -0.04	90[i]	757[i]	no
PCE[b] (tetrachloroethene)	1630	0.89	47.5	31.74[j]	-6.5	18.47	140	no

Table 6.2.1. Properties of selected NAPLs[a]

a. Values are at 25°C and atmospheric pressure unless otherwise noted, b.-k. References for data in table available upon request. l. Calculated from the difference of the air-water surface tension and the sum of the air-NAPL and water-NAPL surface tensions

(a)

(b)

(c)

aperture (mm)

0.013
0.039
0.063
0.09
0.13
0.15
0.21
0.30
0.39
0.50
0.86
1.30

5 cm
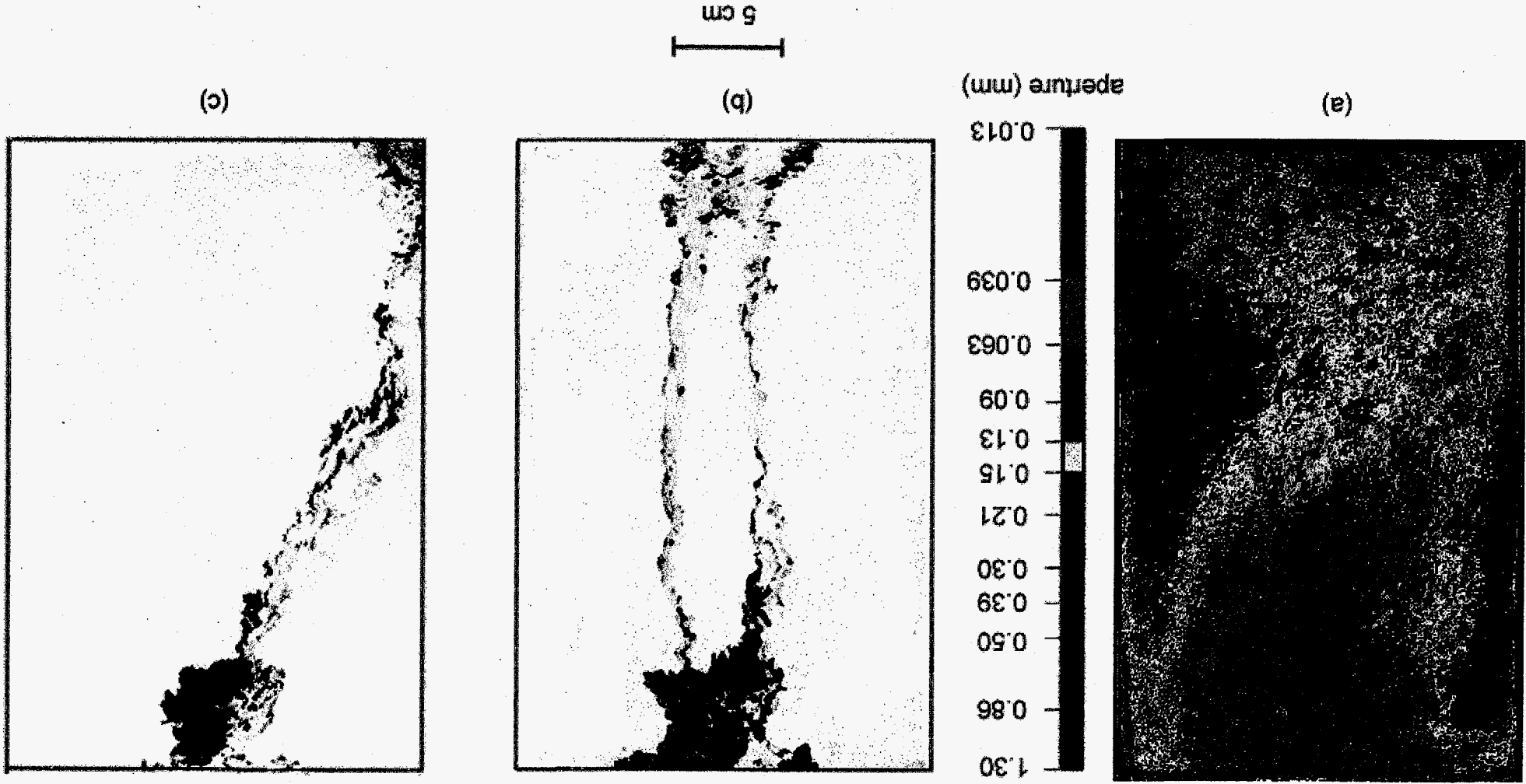
Figure 6.2.1: (a) aperture map
(b) residual water distribution before injecting n-dodecane
(c) residual water distribution before injecting Freon 113

Figure 6.2.2: (a) n-dodecane (red) entering left side of fracture
(b) n-dodecane entering the middle of the fracture
(c) formation of the n-dodecane channel on the right side

5 cm

(a)

(b)

(c)

(a) close-up of top half of fracture

├──┤
2 cm
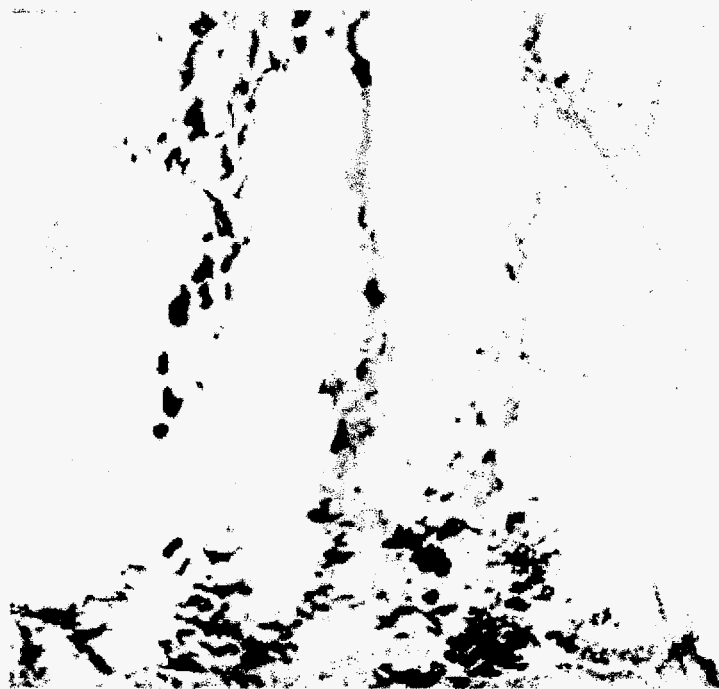
(b) close-up of bottom half of fracture

Figure 6.2.3: n-dodecane entrapped in residual water
6/19/96
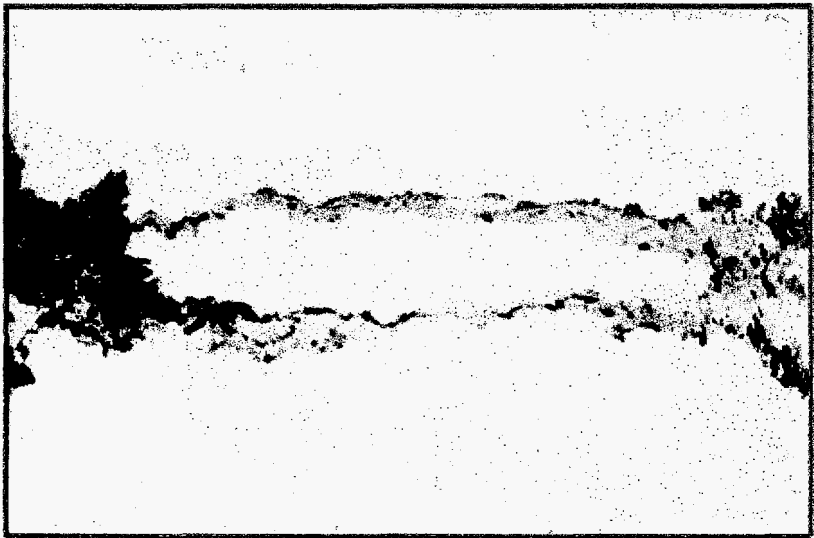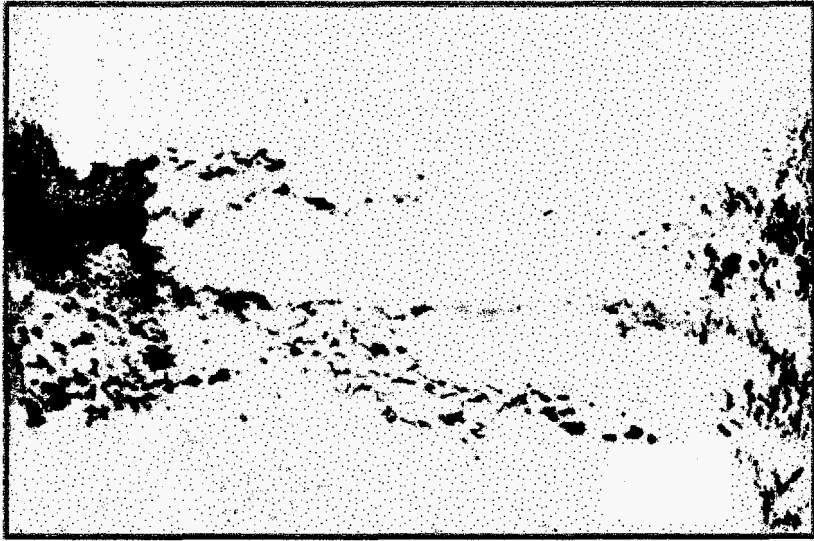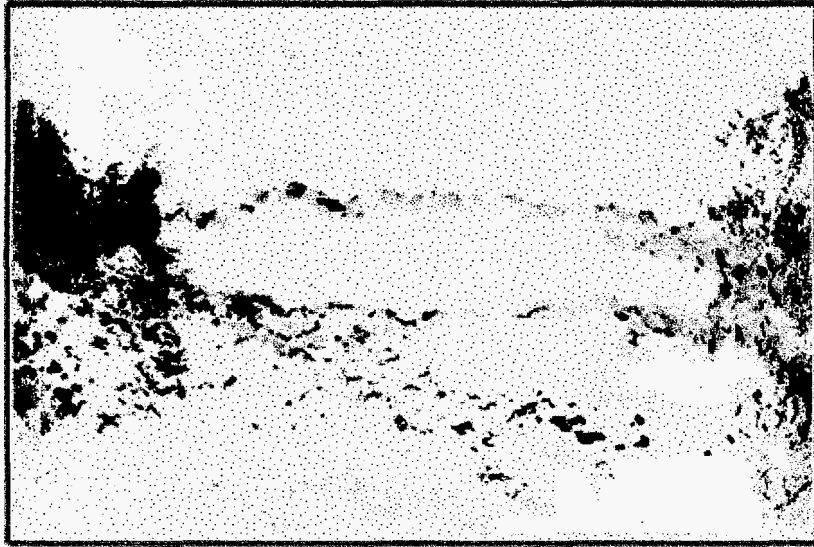
Figure 6.2.4: (a) at residual water saturation
(b) 2 hours after injecting n-dodecane
(c) 19 hours after injecting n-dodecane

5 cm

(a)

(b)

(c)

(a) close-up of top half of fracture

$\vdash\!\!\!-\!\!\!-\!\!\!-\!\!\dashv$
2 cm
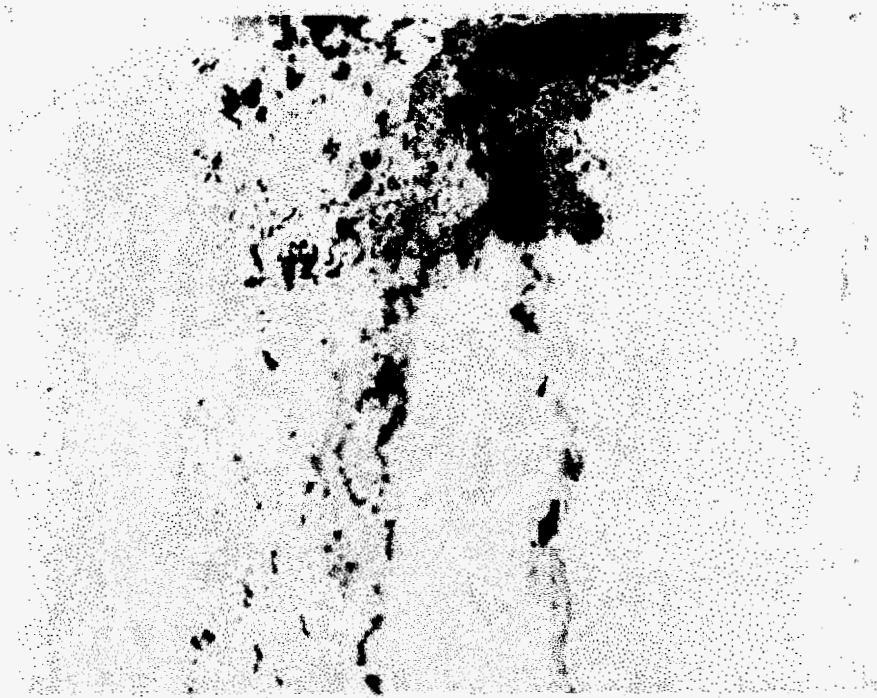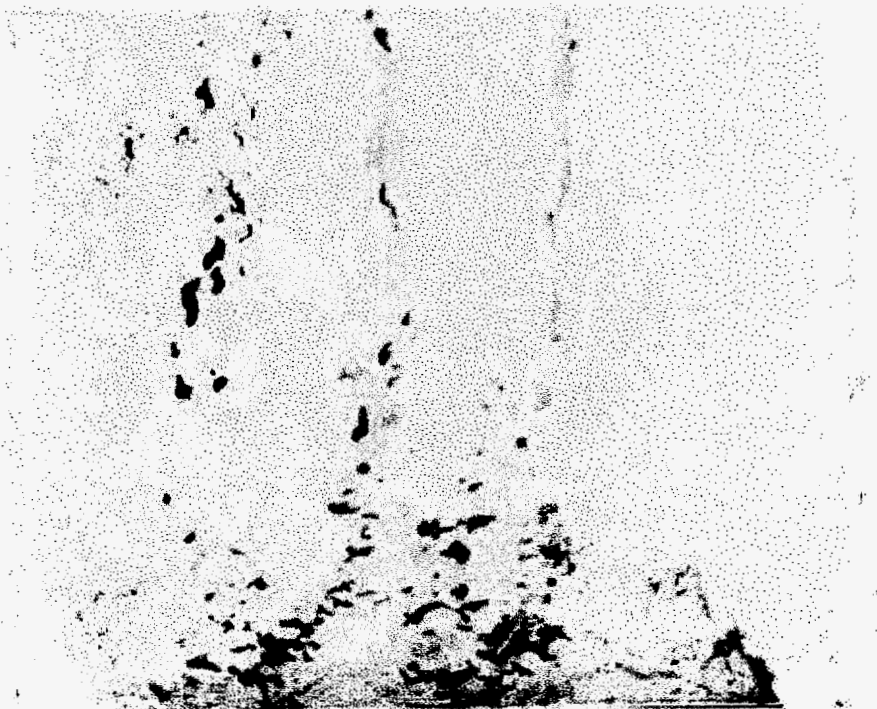
(b) close-up of bottom half of fracture

Figure 6.2.5: n-dodecane at residual saturation
6/20/96
9:00

(a) close-up of top half of the fracture

|⊢————⊣|
2 cm
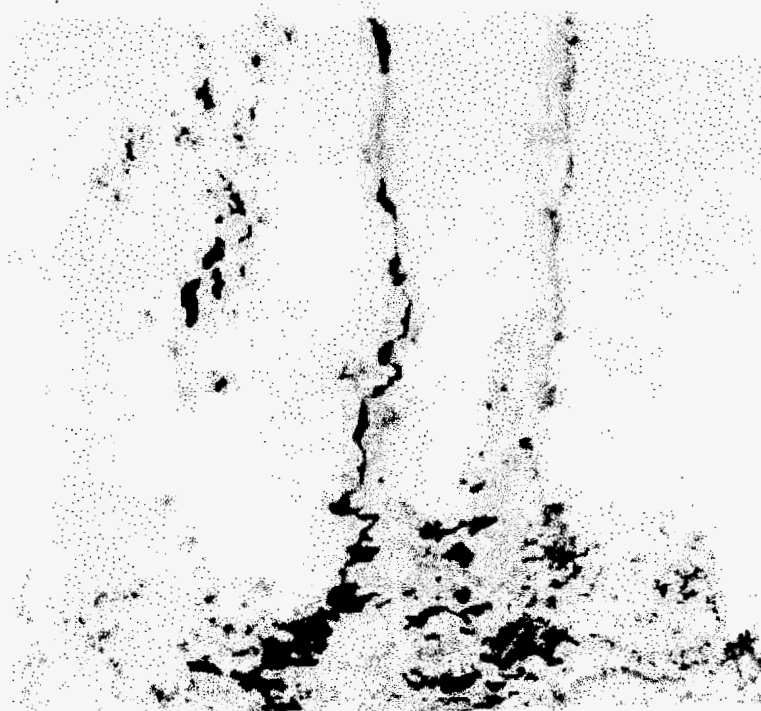
(b) close-up of bottom half of the fracture

Figure 6.2.6: water and n-dodecane distribution 1 hour after
re-introducing water into the fracture
6/20/96
10:42

(a) close up of top half of fracture

2 cm
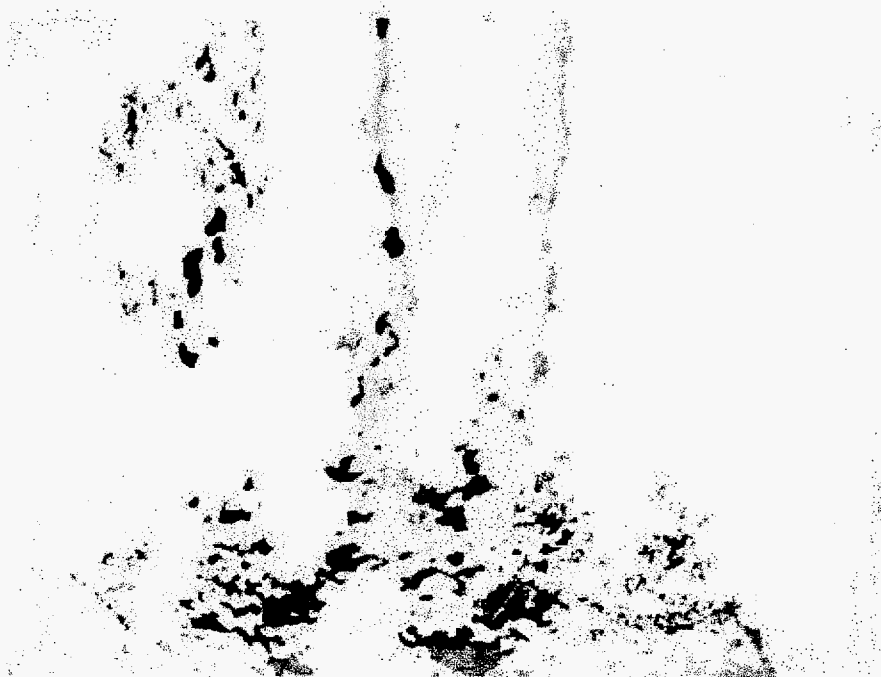
(b) close up of bottom half of fracture

Figure 6.2.7: water and n-dodecane distribution 24 hours after
re-introducing water into the fracture
6/21/96
9:00

81

6/21/96
9:00

6/24/96
11:06

5 cm
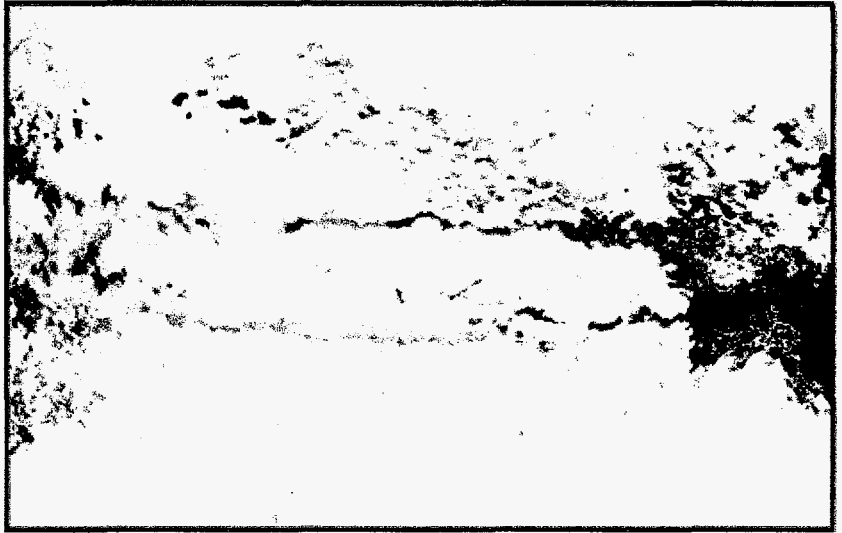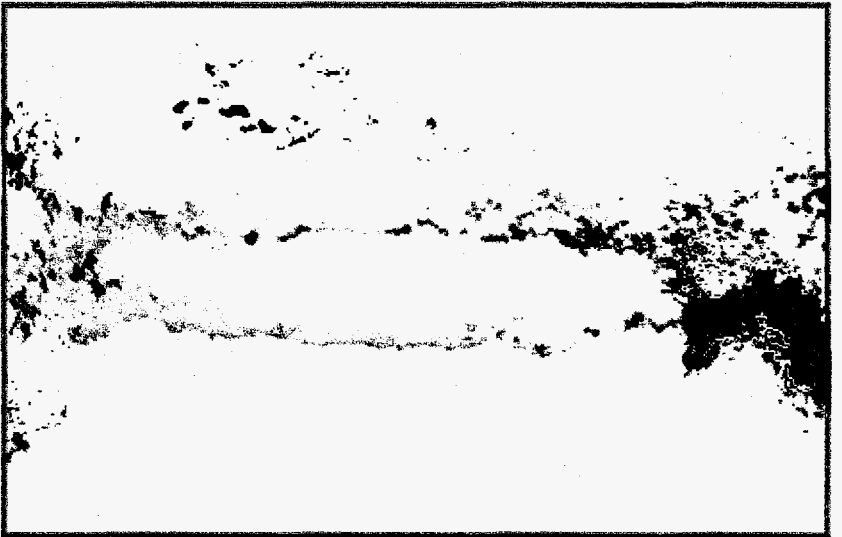
6/25/96
13:30
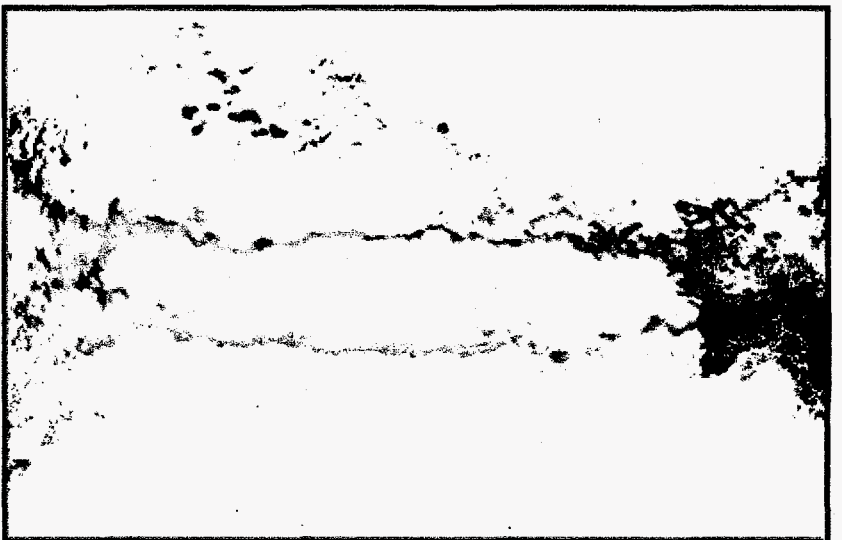
Figure 6.2.8: water and n-dodecane distribution at different days after
water was re-introduced
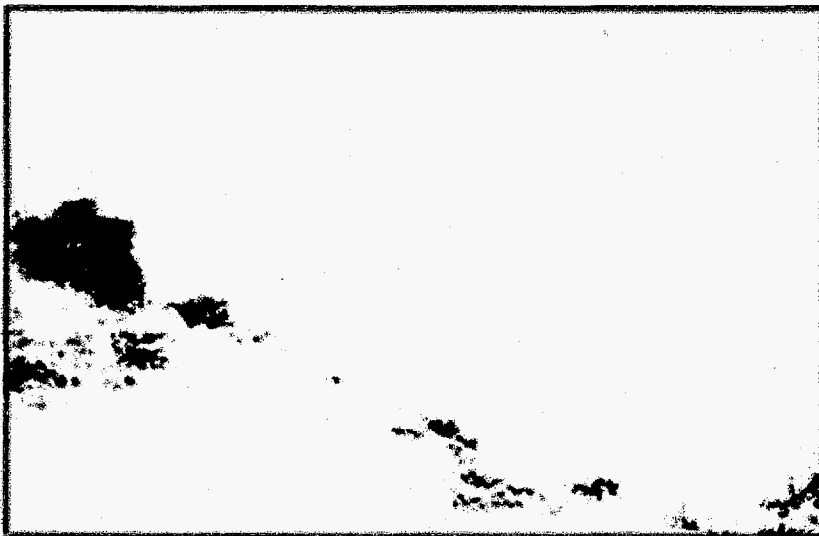
Figure 6.2.9: (a) formation of left Freon 113 channel
(b) formation of 2nd Freon 113 channel
(c) formation of 3rd Freon 113 channel

5 cm

(a)

(b)

(c)

(a)

(b)

location of displaced water
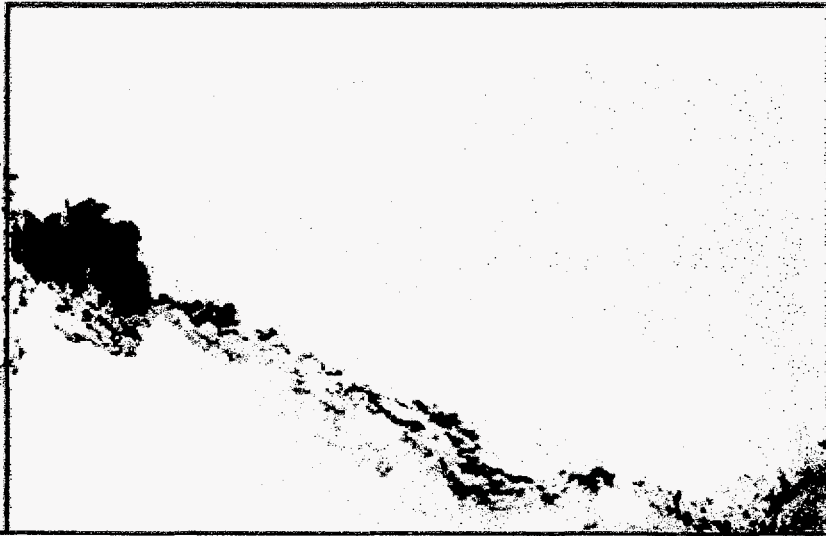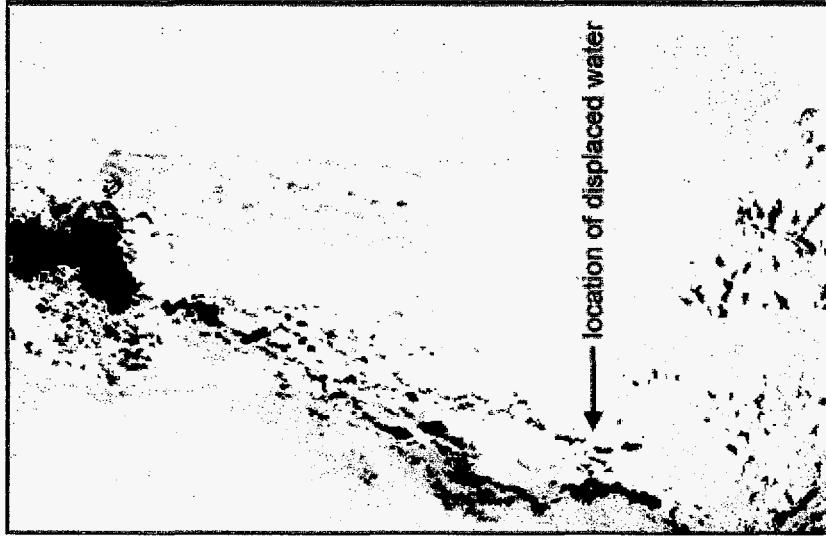
5 cm

Figure 6.2.10: Displacement of residual water by Freon 113
(a) at residual saturation
(b) after displacement

(a) 10.0 min.

(b) 11.75 min.

(c) 15.25 min.

(d) 20.0 min.

Figure 6.2.11: Volatilization of Freon 113 (bright areas) at
various times after injecting Freon 113

7. Multi-Phase Flow Simulation

(K. Pruess, lead author)

Numerical simulations were performed to study water seepage patterns in unsaturated fractures. The purpose of this work was (a) to examine whether multiphase flow in fractures can be described with standard macro-scale continuum concepts, as embodied in Richards' equation (see below), and (b) to investigate space-and-time scaling relationships which may aid in relating laboratory and field scale phenomena. This work is an outgrowth of studies begun under the Yucca Mountain project, and existing simulation tools were used. Below we summarize the approach taken and main results obtained, and discuss issues for future theoretical work. A detailed account of these studies is available in a report (Pruess, 1996a).

Modeling Approach and Results

Natural rock fractures are expected to encompass a vast variety of aperture distributions. The present work focuses on "small" fractures in hard rocks, such as tuffs, basalts, granites, or graywackes. These fractures are modeled as "two-dimensional heterogeneous porous media" (Pruess and Tsang, 1990). Aspects of fracture aperture distributions that are believed to be essential for replicating natural features include (a) the presence of asperity contacts, where the fracture walls touch, (b) a more or less gradual change towards larger apertures away from the asperities, (c) small-scale fracture wall roughness, and (d) finite-size spatial correlation length among apertures. Synthetic aperture distributions with these features were generated by computer, using geostatistical concepts. Fig. 7.1 shows a space-discretized two-dimensional heterogeneous field of "permeability modifiers" ζ_{ij} consisting of $100 \times 100 = 10,000$ blocks of 0.2×0.2 m^2 each. These are used in a finite difference simulation of flow, in which permeability in each block is taken as $k_{ij} = \zeta_{ij} \times k_{ref}$. The reference (background) permeability is chosen in the range of $k_{ref} = 10^{-9}$ -10^{-7} m^2, and strength of capillary pressure is scaled consistently according to $P_{cap} \rightarrow P_{cap}' = P_{cap}/\sqrt{(\zeta_{ij})}$ (Leverett, 1941). Matrix permeability has been neglected in these studies.

Water seepage was simulated by means of our TOUGH2 general-purpose simulation program (Pruess, 1991). The EOS9 fluid property module was used which implements Richards' equation for saturated-unsaturated flow,

$$\frac{\partial}{\partial t}\theta = \text{div}[K\nabla h] \qquad (1).$$

Here t is time, θ is specific moisture content, K is hydraulic conductivity, and h is hydraulic head. The flow simulations were carried out by injecting water at various time-independent rates at the

7. Multi-Phase Flow Simulation

top of the fracture shown in Fig. 7.1. Lateral boundaries were "no flow," and at the bottom a unit head gradient boundary condition was imposed to allow free gravity drainage.

Fig. 7.2 shows seepage patterns obtained for injection over different 1 m intervals, corresponding to five neighboring grid blocks, centered at distances of, respectively, 6.5, 8.5, 10.5, and 12.5 m from the left boundary of the fracture. The seeps are quite different in appearance but share common features. Flow generally proceeds in narrow vertical or sub-vertical fingers. Several flow paths can develop from localized injection. These can either merge again or remain separate as water continues to migrate downward. Perched water bodies develop at asperity contacts which are associated with significant effects of bypassing and lateral displacements. Breakthrough times at 19.5 m depth vary from 14.40 to 24.19 hours, corresponding to average velocities of seep advancement from 0.81 to 1.35 m/hr (see Table 7.1). Lateral displacement over the 19.5 m vertical migration distance varies from -7.5 m to + 1.0 m.

Table 7.1 Simulated results for seeps in heterogeneous fracture.

Seep	# 1	# 2	# 3	# 4
Injection point distance (m)	6.5	8.5	10.5	12.5
Breakthrough time at 19.5 m depth (hours)	16.25	14.40	24.19	15.75
Average seep velocity (m/hr)	1.20	1.35	0.81	1.24
Lateral displacement at breakthrough (m)†	-3.5	-5.5	-7.5	+1.0

† positive when displacement is to the right of the injection point, negative otherwise

Seepage patterns resulting from different injection rates are shown in Fig. 7.3. As injection rates are increased by successive factors of 10, from 10^{-4} kg/s to 10^{-1} kg/s, water saturations generally become larger. There are also striking changes in appearance. Increasing the injection rate tends to diminish lateral fingering flow, while lateral branching again becomes stronger when injection rate is increased beyond 10^{-2} kg/s. This indicates that heterogeneous unsaturated media tend to behave most strongly heterogeneous at large and small water saturations, while behaving less heterogeneous at intermediate water saturations.

7. Multi-Phase Flow Simulation

Behavior under Space and Time Scaling

In connection with waste isolation problems, an assessment of water seepage in heterogeneous fractures is often required for space and time scales far larger than what is accessible through laboratory experimentation and field observation. It is of interest, therefore, to examine the dependence of seepage behavior on the space and time scales involved (Geller and Pruess, 1995; Pruess, 1996b). This was done by considering the behavior of Richards' equation, Eq. (1), under the following simultaneous scaling of space and time coordinates.

$$
\begin{aligned}
t &\rightarrow t' = \lambda_t \cdot t \\
x &\rightarrow x' = \lambda_x \cdot x \\
z &\rightarrow z' = \lambda_z \cdot z
\end{aligned}
\qquad (2).
$$

A classical analysis of scaling behavior of unsaturated flow systems was presented by Miller and Miller (1956). They used a microscopic (pore level) approach to evaluate the conditions for which dynamic similarity would hold, and considered the simultaneous scaling of space and time scales, and constitutive properties (viscosity and surface tension of the fluid, strength of capillary pressure, hydraulic conductivity). For flow systems differing by a common length scale factor, they found that dynamic similitude is only possible when strength of capillary pressure (or surface tension of the fluid) is scaled as well. In contrast to Miller and Miller, we are interested in approximate scaling invariance between macroscopic systems, which is less demanding and may hold under less restrictive conditions than true pore-level invariance. Also, in order that results relevant to water flow at ambient conditions may be obtained, we restrict ourselves to space-and-time scaling alone, and do not allow scaling of the constitutive properties of the fluid or the porous medium.

Our analysis showed that, strictly speaking, it is not possible to achieve scaling invariance simultaneously for vertical flows under (capillary) pressure and gravity forces. However, an approximate scaling invariance may still hold when liquids percolate downward in (sub-)vertical fractures. Downward flow will then be primarily driven by gravity, and capillary and pressure effects on vertical flows may be small. Seepage patterns should be approximately invariant when space and time coordinates are scaled in such a fashion that

$$
\lambda_t = \lambda_x^2 = \lambda_z
\qquad (3).
$$

Thus, the vertical length scale and the time scale need to be stretched by the square of the horizontal scale factor. The approximate scaling invariance of Eq. (3) is expected to break down

7. Multi-Phase Flow Simulation

when scaling down to "sufficiently" small systems, where capillary effects on vertical flow are no longer negligible relative to gravity effects.

A number of numerical simulation experiments have been performed to test the approximate scaling invariance postulated in Eq. (3). We applied scale factors of $\lambda_x = 5$ and $1/5$, respectively, simultaneously scaling spatial dimensions and time according to Eq. (3). The spatial scaling changes the 20 m x 20 m heterogeneous fracture of Fig. 7.1 into 100 m x 500 m ($\lambda_x = 5$) and 4 m x 0.8 m ($\lambda_x = 1/5$), respectively. Source (injection) rates were scaled consistently by $\lambda_t/\lambda_x\lambda_z = 1/\lambda_x$. Upscaling by a factor $\lambda_x = 5$ produces seepage patterns that are so close to the original that for the resolution shown in Fig. 7.2 they would be indistinguishable in all cases. The almost exact mimicking of even small-scale details in saturation distributions between the original and the scaled system demonstrates the excellent validity of the approximate scaling relationship Eq. (3) for this

Table 7.2. Scaling behavior of simulated seeps.

Seep	# 1	# 2	# 3	# 4
Upscaling by $\lambda_x = 5.0$				
Breakthrough time at 487.5 m depth (days)	15.87	14.84	24.95	16.53
Average seepage velocity (m/hr)	1.28	1.37	0.81	1.23
Downscaling by $\lambda_x = 0.2$				
Breakthrough time at 0.78 m depth (min)	55.67	51.95	71.65	58.14
Average seepage velocity (m/hr)	0.84	0.90	0.65	0.80

case. This is further confirmed by a comparison of the average seepage velocities, see Tables 7.1 and 7.2. A different picture emerges for downscaling by a factor of $\lambda_x = 1/5$, see Fig. 7.4. Comparison with Fig. 7.2 shows that, while overall seepage patterns are similar, there are very visible and significant differences. Regions of large water saturation tend to be more extensive in the downscaled system, and overall water saturations tend to be larger. This leads to seepage velocities that are typically 30 % slower (see Table 7.2). It is evident that capillary effects on vertical flow have become significant for the small-scale system shown in Fig. 7.4, so that the scaling relationship Eq. (3) is a rather poor approximation in this case.

89

Conclusions

We have simulated water seepage in unsaturated vertical fractures, which were conceptualized as two-dimensional heterogeneous porous media. Our process description employed conventional macro-scale concepts, which were presumed to be applicable on the grid block scale of order 0.2 m. The seepage patterns seen in our numerical studies show many of the same features that have been seen in our laboratory experiments, and have been inferred for naturally fractured systems in thick unsaturated zones, including flow fingering, bypassing, and ponding. However, our simulations do not produce intermittent flows or cyclic variations in seepage patterns, which were prominently encountered in the laboratory experiments. It is not known at present whether the absence of such phenomena in the simulations is due to the numerical methods and approximations used, or whether it reflects a fundamental limitation in the physical phenomena accounted for by the simulator.

The examples studied suggest that localized infiltration can give rise to a variety of behavior, from localized seeps to broad plumes with dispersed flow at some depth beneath the infiltration region. Field experiments have shown that flow focusing or funneling is also possible for seepage in partially saturated heterogeneous media. The exploration of heterogeneity conditions for which spatially-distributed infiltration could give rise to highly localized preferential flows is of considerable practical interest, as such flows could provide fast paths for the migration of solutes.

An approximate invariance of seepage under simultaneous space-and-time scaling was theoretically derived. The validity and limitations of this invariance were demonstrated through numerical simulations, and through analyses of capillary- and gravity-driven flows. This scaling invariance is believed to be useful in relating laboratory and field scale phenomena.

Future numerical studies should investigate different types of heterogeneity structures and a variety of boundary and source conditions, including non-uniform, localized infiltration at time-varying rates. Two- and three-phase behavior involving nonaqueous phase liquids (NAPLs) should be studied. Of interest is also the interaction between seeps, and between fractures and matrix rock.
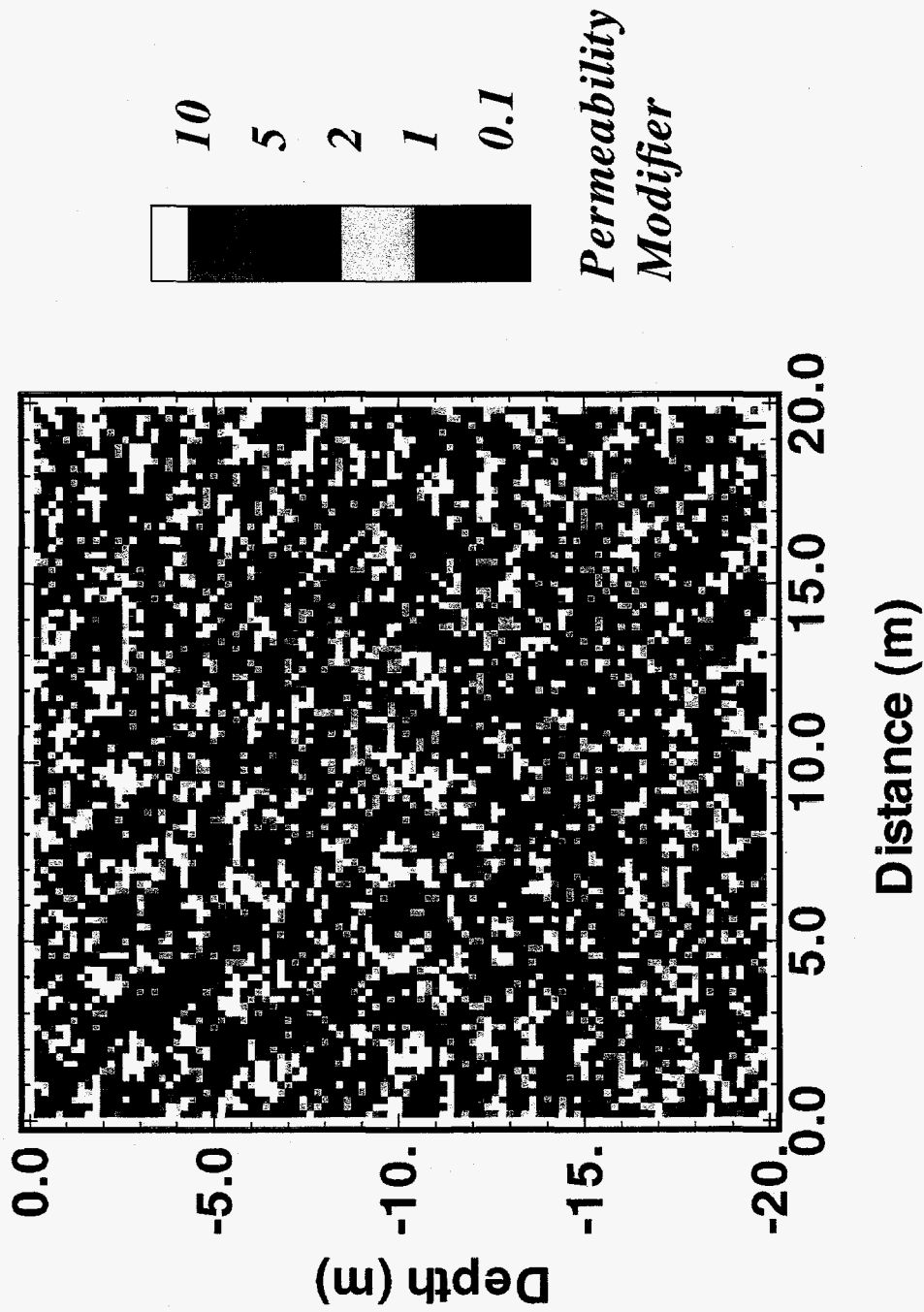
Figure 7.1. Permeability modifiers for synthetic heterogeneous fracture.
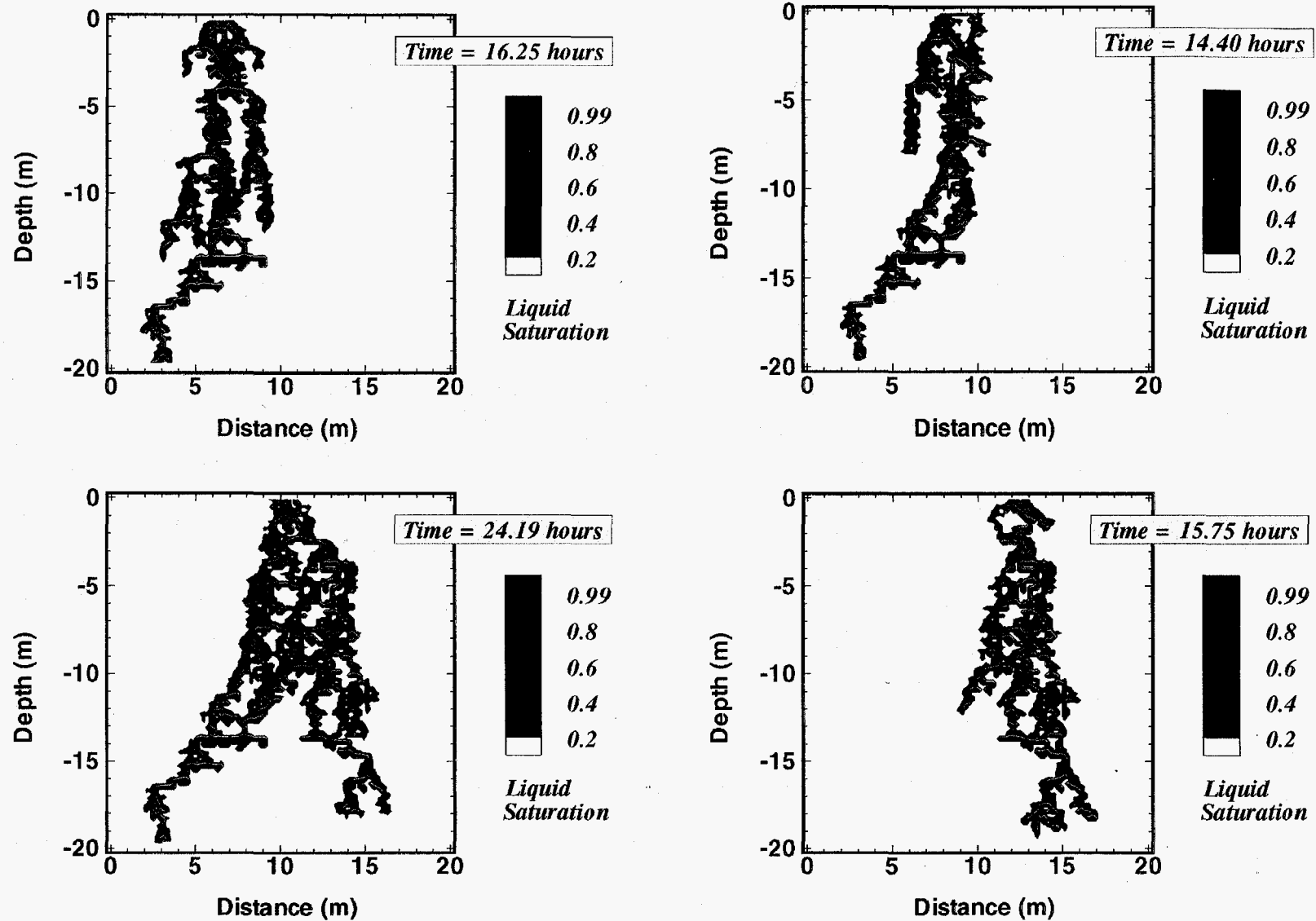
Figure 7.2. Liquid seeps shown at the time of breakthrough at a depth of 19.5 m. Water is injected at a constant rate of 10^{-3} kg/s over a 1 m interval at the top of the fracture. The injection interval is centered at different distances from the left boundary, namely, 6.5 m (top left), 8.5 m (top right), 10.5 m (bottom left), and 12.5 m (bottom right). Reference permeability is 10^{-9} m^2.
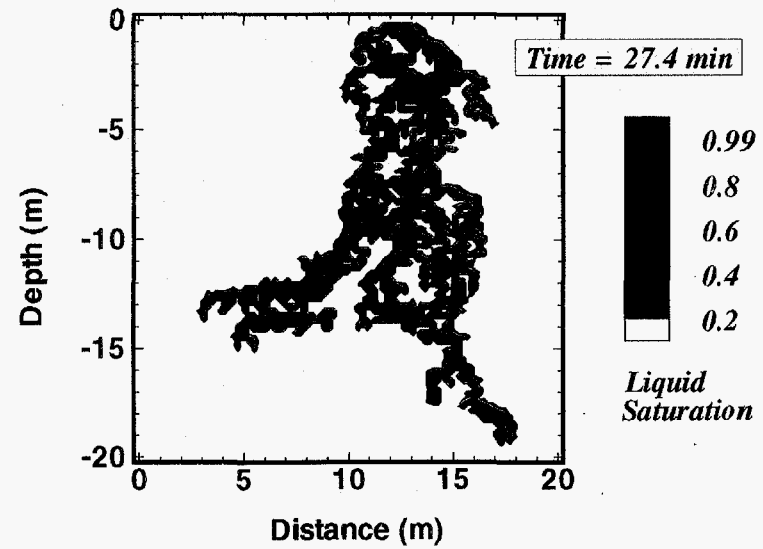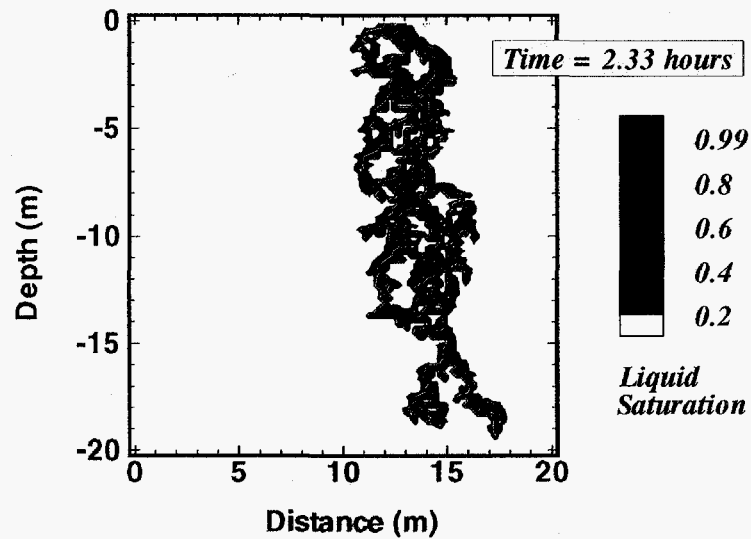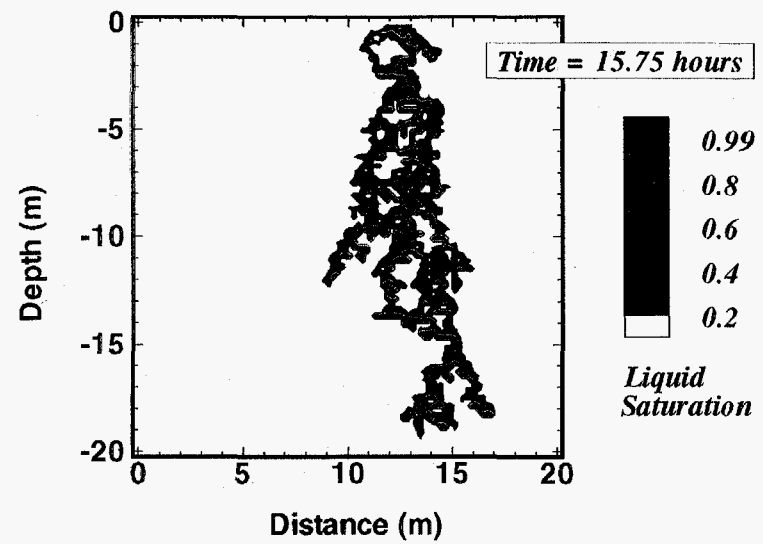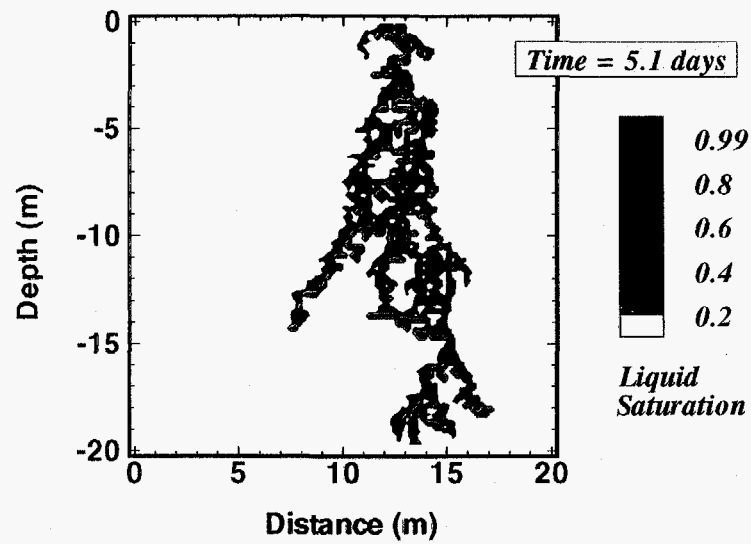
Figure 7.3. Liquid seeps at time of breakthrough at 19.5 m depth for injection at four different rates over a 1 m interval at the top, centered at 12.5 m. Injection rates are 10^{-4} kg/s (top left), 10^{-3} kg/s (top right), 10^{-2} kg/s (bottom left), and 10^{-1} kg/s (bottom right). Reference permeability is 10^{-9} m^2.
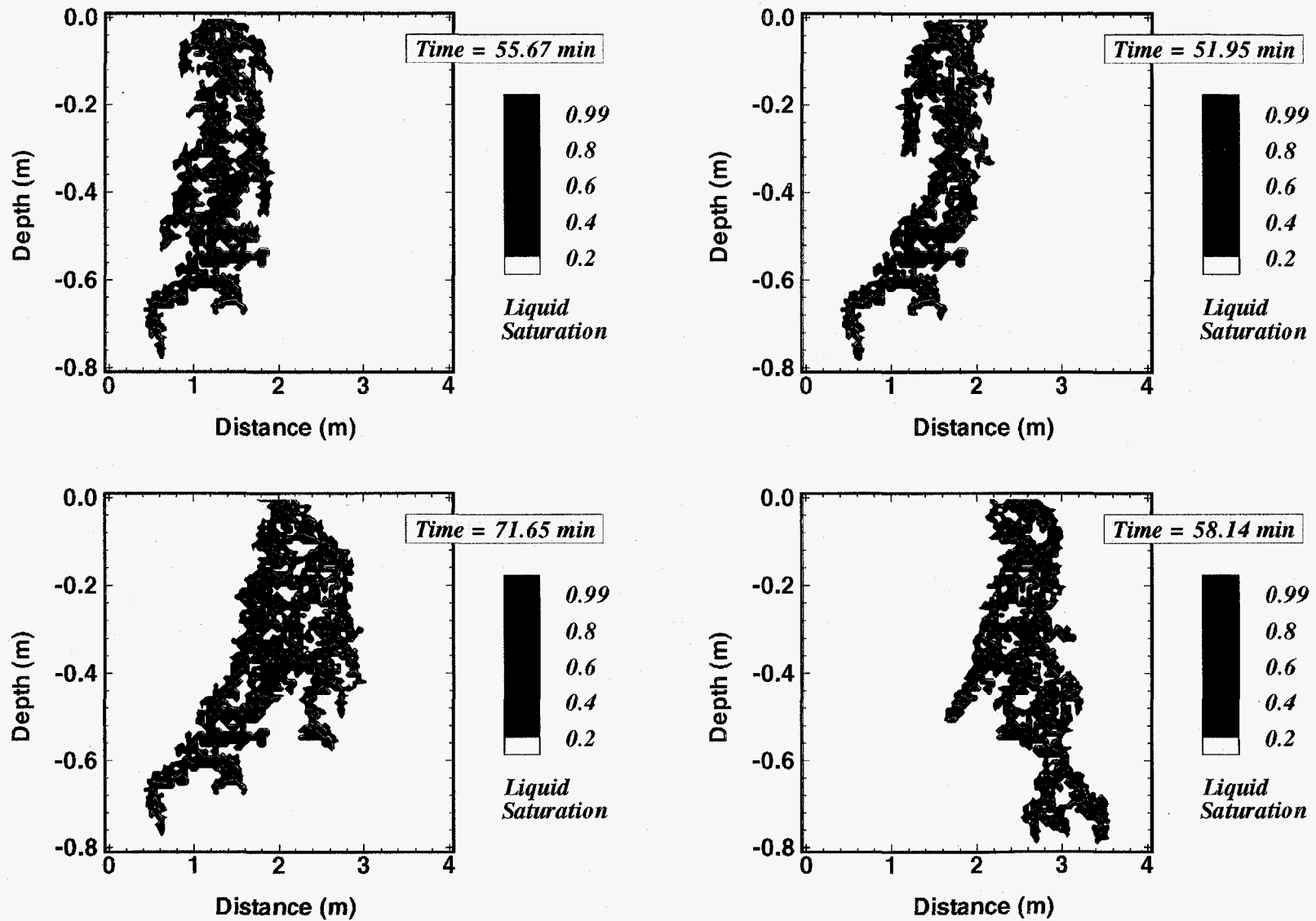
Figure 7.4. Liquid seeps shown at the time of breakthrough at a depth of 0.78 m. Water is injected at a constant rate of 0.2×10^{-3} kg/s over a 0.2 m interval at the top of the fracture. The injection interval is centered at different distances from the left boundary, namely, 1.3 m (top left), 1.7 m (top right), 2.1 m (bottom left), and 2.5 m (bottom right). Reference permeability is 10^{-9} m^2.

8. Biotransformation of volatile NAPL organic contaminants in fractured-rock
(H-Y. Holman, M. S. Conrad and J. C. Hunter-Cevera, lead authors)

The FY96 VOC (volatile NAPL organic contaminant) biotransformation study focused on preparing for the long-term geocosm experiments. This involved (1) improvement and applications of relevant microbial ecology techniques to study the endolithic (rock-inhabiting) microorganisms inside fractured basalt; (2) determining if the endolithic microorganisms can transform volatile organic contaminants (VOCs); and (3) design and construction of a geocosm device that will be used in the future to examine natural processes that would control the kinetics of VOC biotransformation in a fractured-basalt system. To gain insight into the properties of the microbial ecosystem that may exist around the fractured basalt, we also applied efforts (1) and (2) to study microorganisms that inhabit in the sediment interbed. Results from these efforts will be used to set the stage for the geocosm experiments that will take place in FY97 and 98.

Since "aseptic" fractured basalt and sediment interbed were not available before the end of FY96, we used two samples of fractured-basalt, one dense and one vesicular, from the USGS core library (see Section 5.2). They were from Box Canyon, a pristine environment and had never been exposed to VOCs. The sediment interbed samples, on the other hand, were from the SDA of the RWMC and have been exposed to VOCs in the past (see Section 4.1.2).

8.1 Study of microbial ecosystems in fractured basalt

The objective is to establish and implement experimental methods that will be used (1) to test for the presence of microbial life inside cracks, fractures, and in the pore space inside the basalt, and (2) to relate the distribution of the microbes to the basalt characteristics including the mineral composition and grain size. The first objective is achieved by conducting three different experiments: the printing-off cultivation

experiment, the washing-off cultivation experiment, and the moisture stimulation experiment. The second objective can be achieved by using the scanning electron microscopy-energy dispersive X-ray (SEM-EDAX) system to study samples from the cultivation and the stimulation experiments. This effort has just been initiated and will not be described in this report.

The physical characteristics of the two fractured basalt cores used in this study are shown in the following Table.

Core	Depth (m)	Rock type	Gravimetric moisture (% by wt. of dry rock)
1	8.74	Dense basalt	1.18
2	11.61	Vesicular	3.22

Their chemical composition and hydraulic properties have not yet been determined.

Since both cores were neither sampled using the protocol developed by F.S. Colwell of INEL (Colwell et. al., 1992) nor kept under sterile environment in the USGS core library, it is highly likely that they were contaminated with newly arrived non-rock-inhabiting microorganisms. Prior to the study of microbial ecosystems in these samples, at least the airborne non-rock-inhabiting microorganisms were removed by rinsing the rock surface with sterile distilled water as described by Hirsch et al. (1995). This procedure assumes that these non-native microorganisms arrived and colonized the rock by outfall from the air and do not adhere very tightly to the rock matrix.

After rinsing off, 1 mm thin-sections were cut from each rock cores (under sterile environment) for studying the form and arrangement of microorganisms inside the rock as well as their response to moisture. Figure 8.1.1a is a photograph of the typical smooth surface of the 1-mm thin-sections prepared from the fractured dense basalt. Figure 8.1.1b

shows the rough surface of those from vesicular basalt, which has many pits and pore spaces.

Figure 8.1.1. Photographs of the surface of the 1-mm thin-sections prepared from (a) fractured dense basalt, (b) vesicular basalt.

(a)
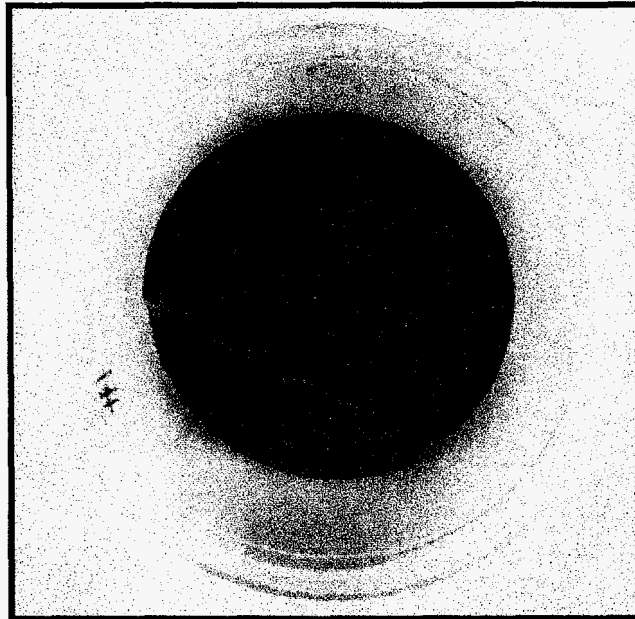
(b)
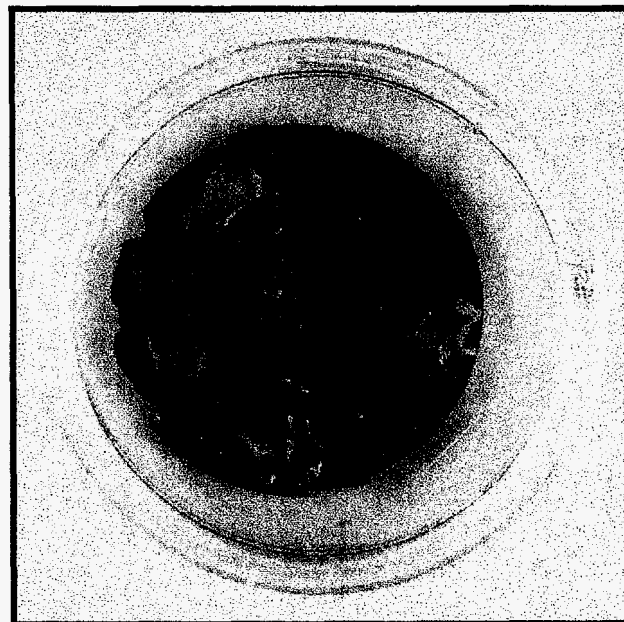
8.1.1 Printing-off cultivation experiment

A modified 2.2% agar technique (Hirsch et al.,1995) was used to reveal the surface distribution and diversity of cultivable microorganisms on the dense basalt and vesicular rocks,. An oligotrophic agar PYGV was prepared from 2.2% Bacto Agar, 0.25 g/L each of Bacto Peptone, Bacto Yeast Extract, glucose, and mixed with a vitamin mixture and mineral salt according to Staley (1968). The medium was poured into sterile petri dishes to form 1-cm thick agar disc. Immediately, the thin-section of basalt was transferred upside down onto the agar and pressed against it for 1 minute while avoiding dislocation. Then a pair of sterile and pointed chopsticks was used to lift the thin section from the agar. The now "inoculated" agar disc was put in the dark and incubated at room temperature ($\approx$ 21°C).

After incubation for 10 days at room temperature (21 ±1°C), colonies were observed on the agar disc. Comparative observations suggest that the distribution and diversity of cultivable microbial consortia inside the dense basalt were significantly different from those inside the vesicular material. The disc that received the "inoculation" from the thin section of the dense basalt, as shown in Figure 8.1.1.1a, had only two colonies and they were chasmoendolithic (i.e., living in and along fractures connected with the surface). The agar disc that received the "inoculation" from thin section of the vesicular basalt, shown in Figure 8.1.1.1b, had developed diversed colonies that are either chasmoendolithic or cryptoendolithic (i.e., lived in fractures connected with the surface as well as in pore space with or without direct connection with the surface). To evaluate their community structure, samples were taken from these colonies, subjected to serial dilution and were further purified by sequential isolation on the nutrient plates until colonies of a single species were obtained. Their identifications are still underway using systems based on colony and cellular morphology, BIOLOG and fatty acid methyl ester (FAME) analysis. Preliminary results of some characteristics of the microbial community in dense and vesicular basalt are shown in Table 8.1.1.1. Figure 8.1.1.2 and 8.1.1.3 are photographs of some distinct colonies isolated from the dense and the vesicular basalt.

Table 8.1.1.1 Preliminary results of some macroscopic characteristics of the microbial community in basalt

(a) Dense basalt

Characteristics	Distinct	Colony I.D.
	1	2
Shape	circular	circular
Size (cm)	0.1	0.35
Chromogenesis	cream	white
Opacity	opaque	opaque
Elevation	raised	raised
Surface	smooth	smooth
Edge	entire	entire

(b) Vesicular basalt

Characteristics	Distinct Colony I.D.									
	1	2	3	4	5	6	7	8	9	10
Shape	circular	circular	irregular	circular	circular	circular	circular	circular	circular	circular
Size (cm)	0.2	0.2	0.6	0.2	0.2	0.2	0.8	0.8	1.0	1.5
Chromogenesis	cream	white	cream	white	red	orange	white	yellow-organge	white	white
Opacity	opaque	translu-cent	translu-cent	opaque	opaque	opaque	transpar-ent (opaque	opaque	translu-cent	transpar-ent (opaque

Figure 8.1.1.1. Photographs of colony growth on the agar disc that received the "inoculation" from a thin section of the (a) dense basalt, (b) vesicular basalt.

(a)
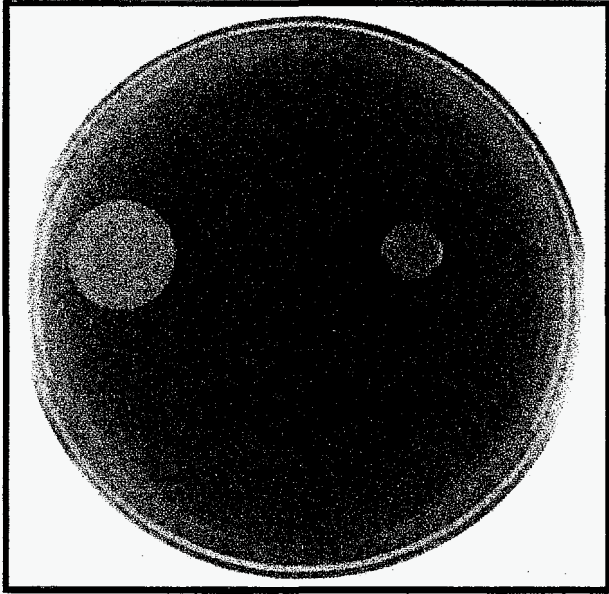
(b)
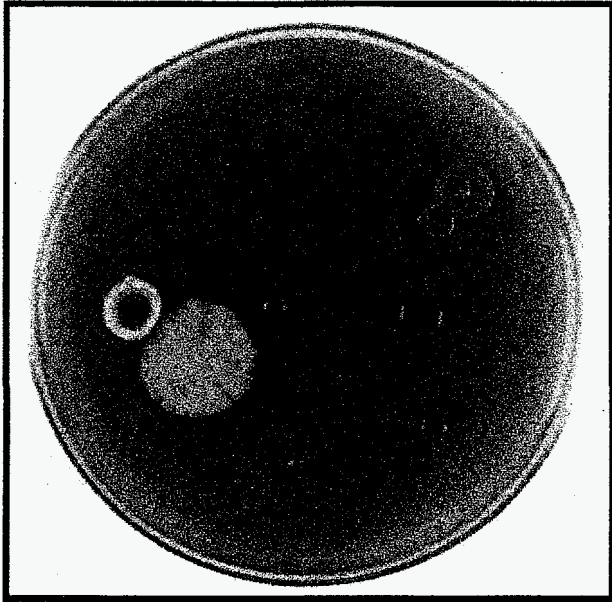
Figure 8.1.1.2. Micrographs of some distinct colonies isolated from the dense basalt (20x).

(a) Distinct colony type 1

(b) Distinct colony type 2
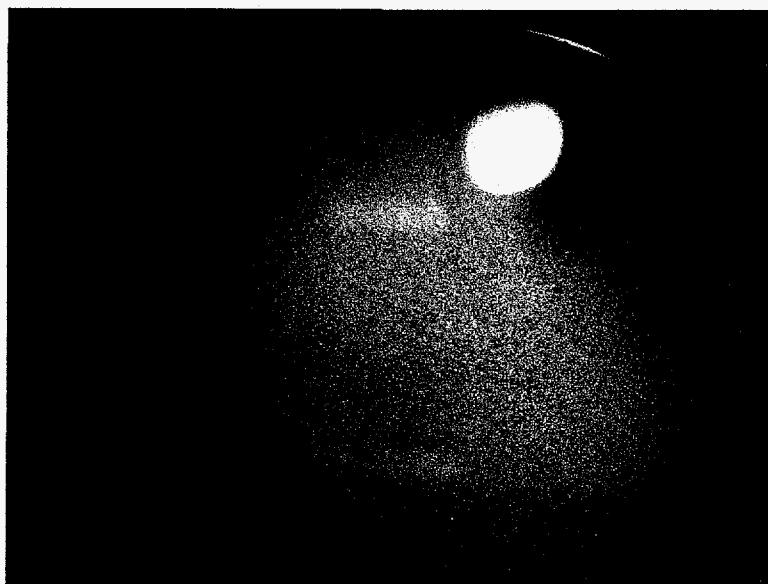
Figure 8.1.1.3a. Micrographs of some distinct colonies isolated from the vesicular basalt (20x).

(a) Distinct colony type 1
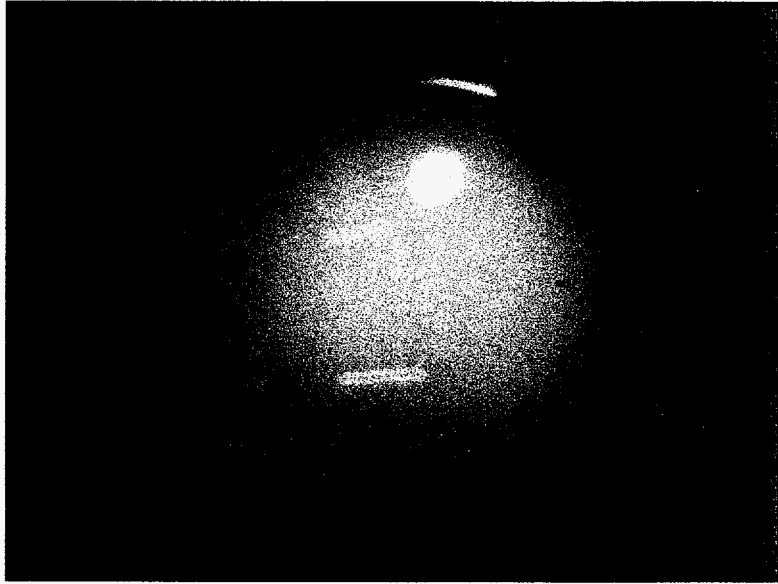
(b) Distinct colony type 2
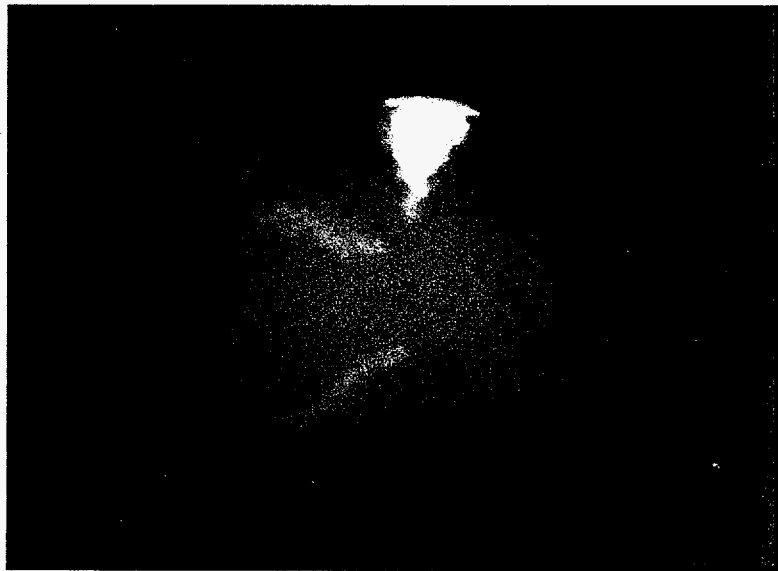
Figure 8.1.1.3b. Micrographs of some distinct colonies isolated from the vesicular basalt (20x).

(a) Distinct colony type 5
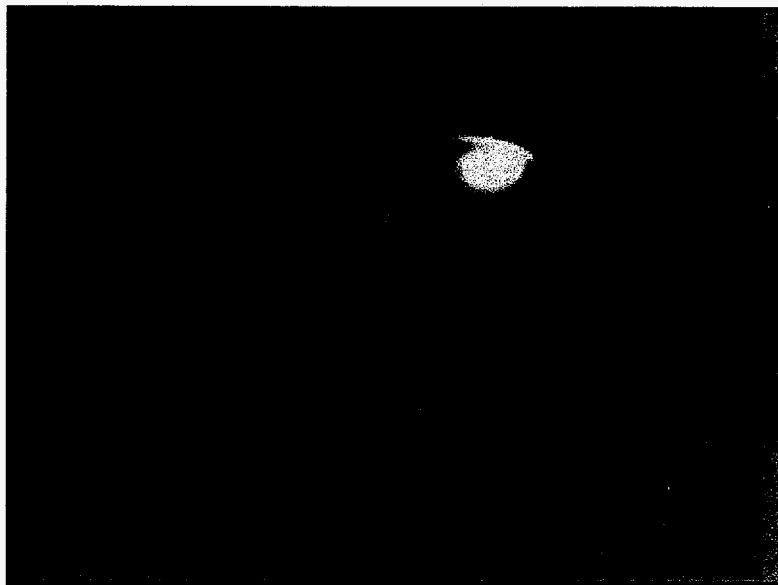
(b) Distinct colony type 9
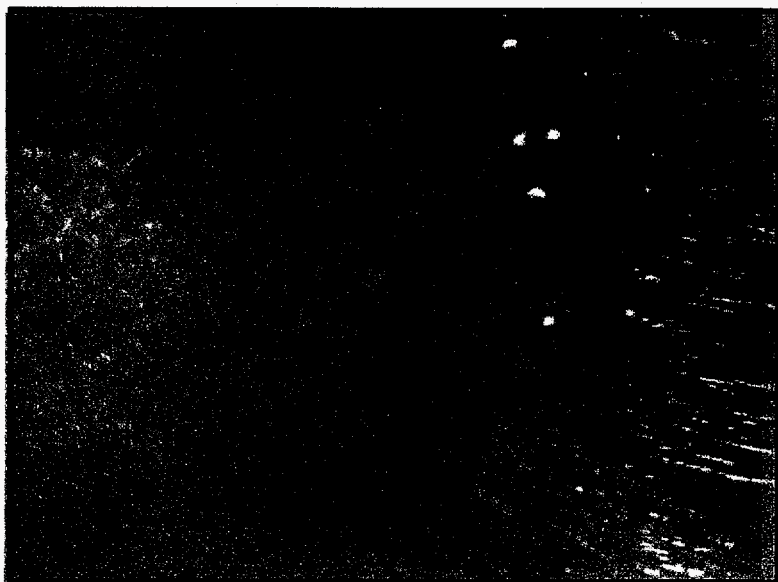
8.1.2 Washing-off cultivation experiment

Techniques by Weirich and Schweisfurth (1985) were used in this experiment to obtain endolithic microorganisms from the same thin-sections for direct microscopy and characterization. Solution of 0.1% sodium pyrophosphate was used to wash off microorganisms from inside cracks, fractures, and in the pore space of the dense and vesicular basalt specimens. The rinse was collected and the microorganisms were further diluted and plated on nutrient-poor 'PYGV' agar media that was prepared according to Hirsch et al. (1995). Since endolithic microorganisms grow very slowly, colony forming units (cfus) were counted every 2, 4, and 8 weeks. The colony forming unit at the end of the 8th week was 7.5×10^1 / cm^2 for the dense and 1×10^5 / cm^2 for the vesicular basalt. To evaluate the community structure of these endolithic microbes, samples were taken from these colonies and were subjected to the same purification procedure and identification systems as described in Section 8.1.1.

Metabolically active endolithic microorganisms dispersed in the 0.1% sodium pyrophosphate solution were observed by means of the acridine orange (AO) and the fluorescein isothiocyanate (FITC) staining techniques. The AO stains the DNA inside the cells and assumes that living cells take up small quantities of the dye and appear green; dead cells absorb large quantities of the dye and appear yellow (Paul and Clark, 1989). The amine-reactive FITC binds to proteins on the surface of the bacteria cells and can be made fluoresce when exposed to ultraviolet light. However, our results from both staining techniques were not satisfactory. We are now in the process of improving our staining procedure. We also plan to use a fluorescent redox dye, 5-cyano-2,3-ditolyl tetrazolium (CTC), as described by Rodriguez et al. (1992).

8.1.3 Microbial growth stimulation by moisture

In vadose zone, the environmental condition inside the fractured basalt can be quite extreme with significant changes in water activity, nutrient supply or even in temperature. As a starting point, we have designed a series of experiments to quickly measure if the growth of endolithic microbes is sensitive to the relative humidity of the air. The experimental design is based on two assumptions. First, the microbial distribution and the mineral properties along the positive surface of the thin-section of basalt, as illustrated in Figure 8.1.3.1, are similar to those along the corresponding negative surface. At the macroscopic level, as demonstrated by Figure 8.1.3.2, the similarities of the distribution of microbial colonies inocculated from the positve and the negative surfaces of the section have proved the first assumption to be valid. The second assumption is that the microbial communities on both sides of the thin-section would response to the change of atmospheric moisture in a similar manner. This assumption will be tested in the early part of FY97.

Figure 8.1.3.3 shows schematically the set-up for the ongoing moisture stimulation experiment. Thin-sections of the dense and vesicular basalt were placed asceptically into sterile incubation tubes that were made from 3-inch diameter Plexiglas columns. At t = 0, sterile air saturated with water vapor was introduced at a rate of 0.1 mL/min into tubes that house the positive side of the thin-sections. Tubes that house the negative side of the thin-sections received only sterile ambient air without the enrichment of water vapor. The positive and the corresponding negative thin-sections are removed periodically. Their surface will be stained and examined directly under microscope for the distribution of metabolically active microorganisms. Results from this effort will be used as reference to the development of the range of "environmental" conditions for the future long-term geocosm experiment.

Figure 8.1.3.1 A schematic illustration of the positive and negative surface of the thin-section of a basalt sample

Positive surface
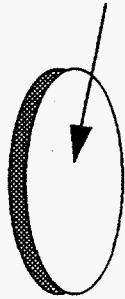
Negative surface
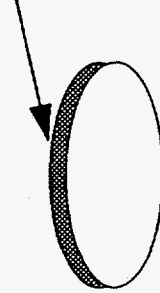
Figure 8.1.3.2. Photographs of colony growth on the agar disc that received the "inoculation" from (a) the positive, and (b) negative surface of the thin section of the vesicular basalt.

(a)
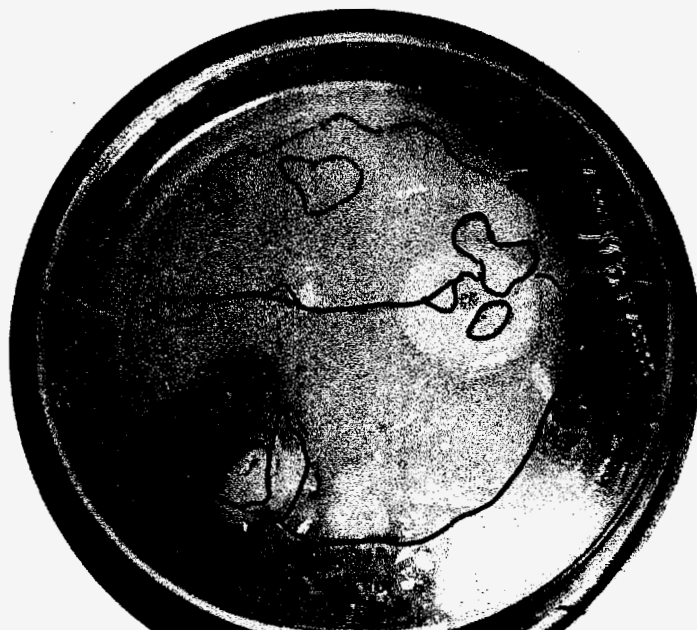
(b)
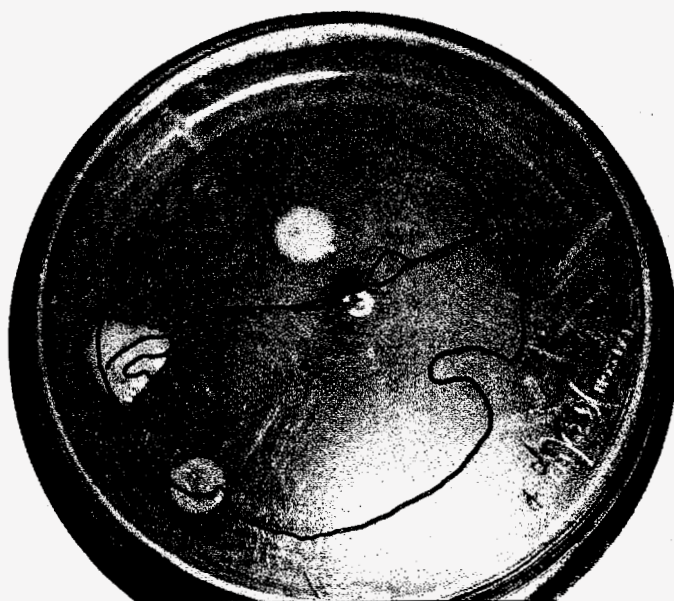
Figure 8.1.3.3 A schematic diagram of the moisture stimulation experiment.

(a) Without moisture stimulation

Filter-sterile
ambient air

Inlet

Outlet

Positive surface of
the basalt thin-section

(b) With moisture stimulation

Filter-sterile
100%RH air

Inlet

Outlet

Negative surface of
the basalt thin-section
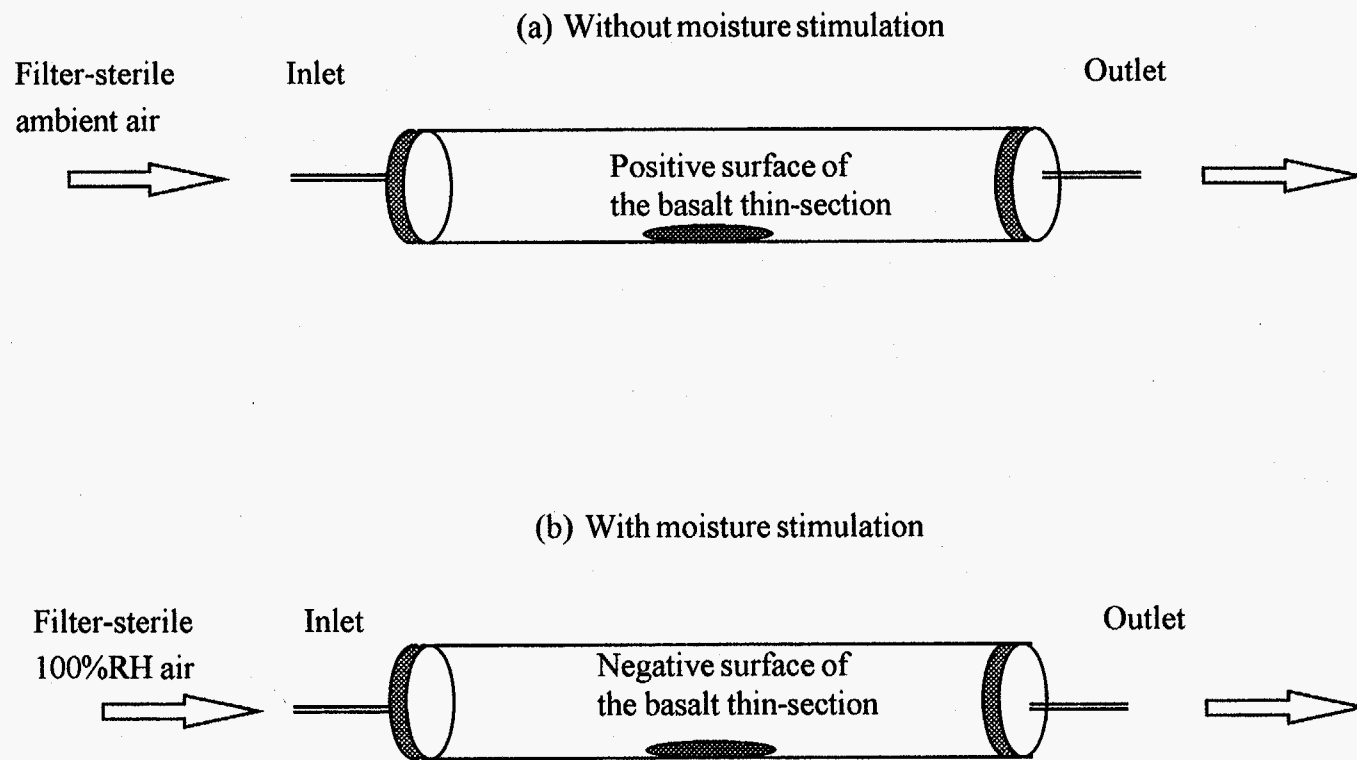
8.2 Study of microbial ecosystems in the sediment interbed

We have not analyzed the chemical compositions of the sediment interbed but will do so in the future. To evaluate the community structure of the microbes in the sediment interbed, 10 grams of the sediment from each sample were first suspended in 95 mL of 0.1% sodium pyrophosphate solution. This was followed by various degrees of dilution. Microorganisms in the suspension were subjected to the similar purification procedure and identification systems as described in Section 8.1.1. Preliminary results of some of the microbial community characteristics are shown in Table 8.2.1.

Table 8.2.2. Preliminary results of some characteristics of the microbial communities
in the sediment interbed

Depth (ft)	Sampling date	Sediment texture, color	% moisture by dry wt.	# cfu/g dry wt.	# of distinct colony types
10	12/15/95	Gravel, dark grey	0.46	3.0×10^5	4
15	12/15/95	Very coarse, dark grey	0.46	ND	NA
20	12/15/95	Very fine, dark brown	0.49	ND	NA
25	12/15/95	Very fine, dark brown	0.59	ND	NA
30	12/15/95	Very fine, dark brown	0.39	ND	NA
34	12/15/95	Very fine, Rusty	2.27	6.5×10^6	6
40	12/15/95	Very fine, dark brown	0.49	ND	NA
45	12/15/95	Very fine, dark brown	0.48	ND	NA
95	01/12/96	Very fine, dark brown	1.84	ND	NA
102	01/15/96	Very fine, dark brown	0.49	ND	NA
105	01/15/96	Very fine, dark brown	0.68	ND	NA
106	01/15/96	Very fine, dark brown	0.90	ND	NA
111	01/15/96	Fine, light brown	1.21	ND	NA
113	02/22/96	Gravel, Dark grey	0.58	ND	NA
124	02/23/96	Very coarse, dark brown	0.44	ND	NA
127	02/26/96	Very coarse, dark brown	0.49	ND	NA
184	02/27/96	Very fine, Rusty	2.90	1.1×10^4	1
189	02/27/96	Very fine, Rusty	2.70	1.1×10^3	1
576	03/04/96	Very fine, Rusty	11.28	7.0×10^5	11
596	03/04/96	Coarse, Rusty	6.80	8.0×10^5	8

8.3 Biotransformation and mineralization of VOCs

We have just started to construct the microcosm experiment to determine if microorganisms inside the fractured basalt and the sediment interbed can biotransform (incompletely biodegrade) and/or mineralize (completely biodegrade) toluene and trichloroethylene. Toluene is selected to model the biotransformation/mineralization driven by the primary substrate utilization mechanisms; trichloroethylene is selected to model the biotransformation/mineralization of a secondary substrate in the presence of methane as a primary substrate. Under appropriate biogeochemical conditions, both toluene and trichloroethylene can be degraded aerobically and anaerobically. In this effort, we examined only the aerobic biodegradation of VOCs since all our subsurface geological materials have been exposed to air for months.

8.3.1 Biotransformation and mineralization of toluene

Aerobic biotransformation and mineralization of toluene have been widely documented and studied in soil and aquifer. The likely processes involved in oxidizing toluene aerobically through primary metabolism are shown below (Cerniglia, 1984).

CH₃

Toluene

CH₃
,H
OH
OH
H
(+)-cis-2,3-dihydroxy-
2,3-Dihydrotoluene

CH₂OH

Benzyl alcohol

CHO

Benzyl aldehyde

CH₃
OH
OH

3-Methylcatechol

COOH

Benzoic acid

Ring Fission

OH
OH

Catechol

Ring fission

Ortho fission   Meta fission

COOH   CHO
COOH   COOH

cis,cis-muconic   OH
acid   2-hydroxymuconic
semialdehyde

H₂O + CO₂   H₂O + CO₂

113
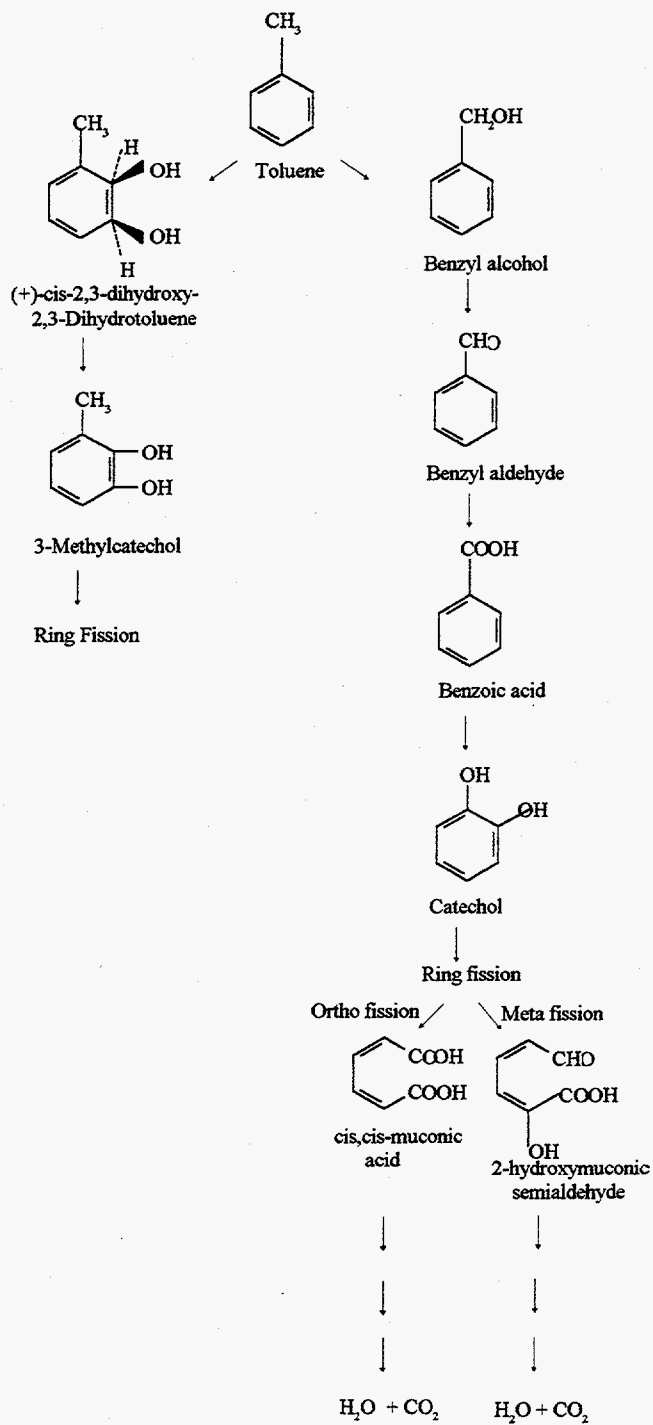
Figure 8.3.1.1 shows schematically the set-up of the ongoing microcosm experiment that we have designed to measure the degradation of toluene. The main part of the microcosm is a 500 mL septa-jar wide-mouth container (Fisher Scientific). Inside the container are: a scintillation vial with 2.5 mL of 1 N NaOH solution, a scintillation vial with an amount of diluted hydrogen peroxide solution to maintain an aerobic atmosphere, and 10 grams of the basalt chips (or sediment interbed, depending on the experiment) coated with 40 ppm of aqueous ^{14}C-labeled toluene. If the microorganisms can degrade toluene completely, $^{14}CO_2$ will be liberated and picked up by the NaOH in the vial. During the experiment NaOH will be removed periodically for counting. If the microorganisms can only partly degrade toluene, the concentration of ^{14}C-labeled toluene will decrease and will be determined by analyzing the amount of ^{14}C-labeled toluene at the end of the experiment.

8.3.2 Biotransformation and mineralization of TCE

Although TCE is generally considered more recalcitrant than toluene in aerobic environment, it still can undergo biodegradation. The likely processes involved in oxidizing TCE aerobically through co-metabolism in the presence of methane are (Henry and Grbic-Galic,1994):

Methane oxidation:

$$CH_4 \xrightarrow[\substack{NADH, O_2 \quad H_2O, NAD^+}]{E_1} CH_3OH \xrightarrow[\substack{X \quad XH}]{E_2} H_2CO \xrightarrow[\substack{NAD^+ \quad NADH}]{E_3} HCOOH \xrightarrow[\substack{NAD^+ \quad NADH}]{E_4} CO_2$$

(Cell assimilation from H_2CO)

TCE epoxidation:

$$CCl_2=CHCl \xrightarrow[\substack{NADH, O_2 \quad H_2O, NAD^+}]{E_1} Cl_2C\overset{O}{-}CHCl \xrightarrow{1,2} \begin{matrix}CO, HCOO^-,\\ Cl_2HC\text{-}COO^-,\\ OHC\text{-}COO^-\end{matrix} \xrightarrow{3,4} \begin{matrix}Cl^-\\ CO_2\\ H_2O\end{matrix}$$
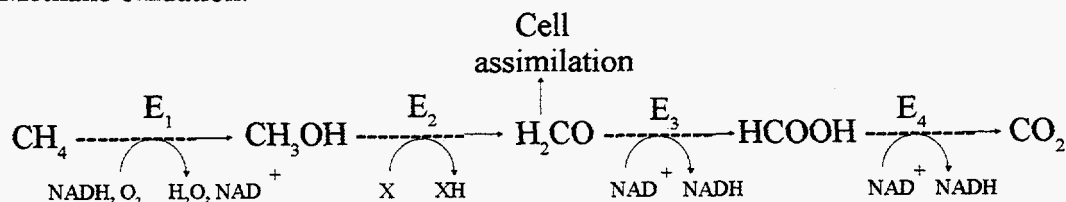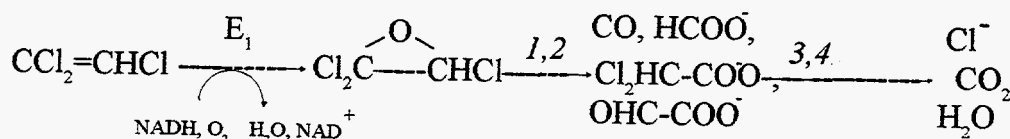
1 = extruded from cells; 2 = abiotic hydrolysis;
3 = methanotrophic degradation
4 = heterotrophic degradation

114

where

E_1 = methane monooxygenase (MMO)
E_2 = methanol dehydrogenase or alcohol oxidase
E_3 = formaldehyde dehydrogenase
E_4 = formate dehydrogenase
NAD = nicotinamide adenine dinucleotide
$NADH$ = rediuced nicotinamide adenine dinucleotide
X = a proton and electron carrier

The set-up of the ongoing microcosm experiment for TCE is basically the same as that for toluene except for the following: the subsurface materials are coated with 40 ppm of aqueous ^{14}C-labeled TCE and the air inside the container has approximately 0.5% of methane at the beginning of the experiment.

Figure 8.3.1.1 A schematic diagram of batch microcosm experiment that we designed to measure the degradation of volatile organic hydrocarbons

Microsyringe with interchangeable connector for VOC analysis or oxygen concentration monitoring

Syringe

Air out

Return air

500 ml septa-jar wide-mouth container

1 N NaOH solution

Dilute hydrogen peroxide solution

Basalt chips or sediment interbed with ^{14}C-labeled VOCs
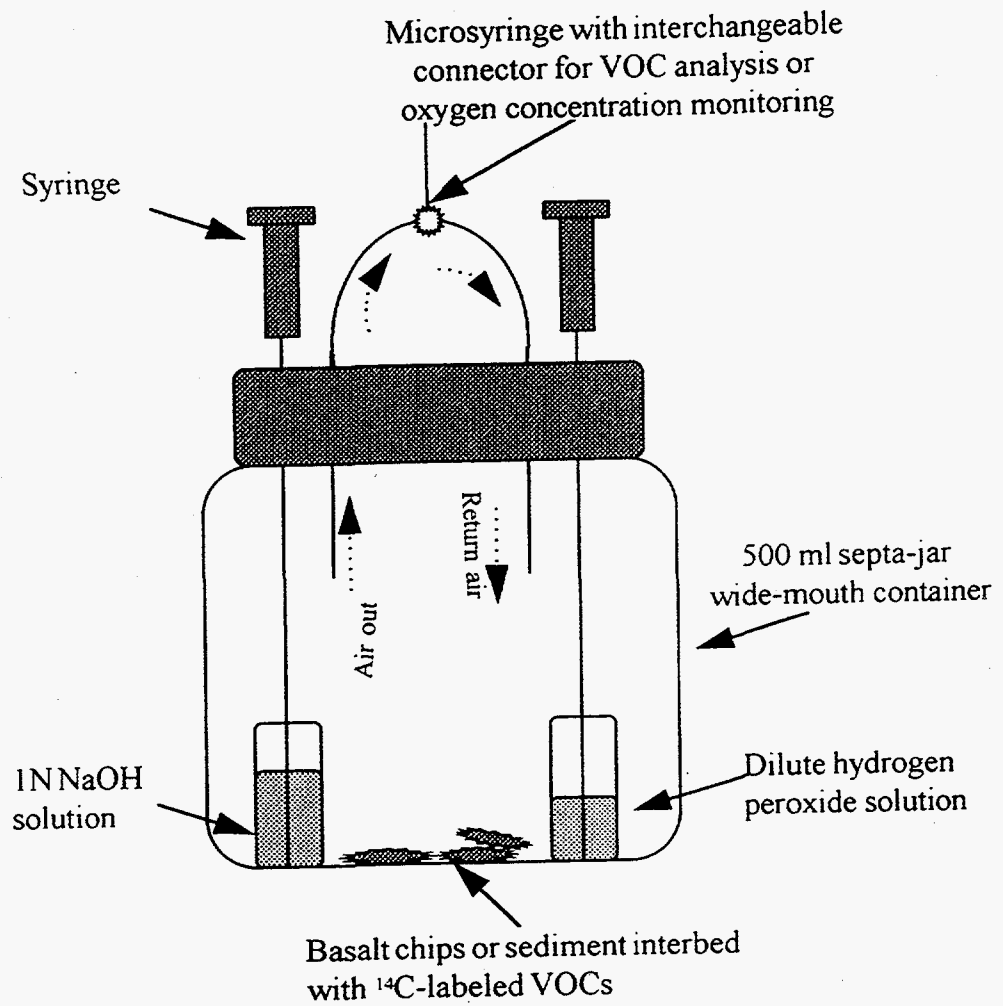
8.4 Design and construction of the geocosm model

A geocosm experimental protocol has been developed for determining the important kinetic parameters controlling the *in situ* biotransformation of toluene and trichloroethylene. Figure 8.4.1 is a schematic of the model designed and under construction for a single basalt sample. Once this single-unit model is tested to be a viable experimental setup, we would expand it to a multiple-unit system.

The model is built on the concept behind the flexible wall permeameter and the associated pressure control mechanism. The main components of the geocosm model are the flexwall cell, the interface units and the pressure controllers that will be used to control the flow in our basalt specimen. The basalt specimen is sealed in a viton jacket and placed inside the flexwall cell that will be filled with water. For each experimental stage, pressure of the water inside the flexwall cell will be controlled to simulate the external stress state on the basalt specimen due to the surrounding subsurface materials. The interface units, with the proper manipulation of the pressure controls, function as our flow delivery system. Fluid inside the interface units can be water, nonaqueous phase liquid or vapor phase, depending on our experimental conditions. The system is now being used.

Figure 8.4.1 A schematic diagram of the model designed and under construction for the future geocosm experiment.

Pressure control # 1

Pressure control # 2

Sampling
(to GC/HALL, GC/MS, or fiber optics)

Pressure control # 3

Air

H_2O

Air

H_2O

Air vent # 1

Metered valve

Air

H_2O

A: Air with 100%RH
B: Diluted primary substrate
C: Diluted secondary substrate

H_2O

Rock Sample

Interface unit # 1

Interface unit # 2

Filter-sterile dry air

VOC trap

Exhaust gas

Metered valve

A   B   C

Inlet/Outlet Pressure Transducer

Air vent # 2

Sampling
(to GC/HALL, GC/MS, or fiber optics)

$^{14}CO_2$ traps

8.5 Isotope Studies

(M. S. Conrad, lead author)

One of the goals of this project is to develop techniques for field monitoring of the processes observed in the laboratory experiments. One approach we are utilizing for this purpose is to measure the isotopic composition of byproducts of microbial metabolic processes that can be detected in soil gas (e.g., CO_2) or groundwater (e.g., dissolved inorganic carbon compounds or DIC) at contaminated sites. The reason for monitoring the isotopic composition of these potential metabolic byproducts, rather than just their abundance, is that there other processes, such as root respiration or dissolution of soil carbonates, that can produce these compounds in the subsurface. In addition, microbes have other substrates besides contaminants that they can utilize, such as endogenous soil organic matter. Compounds manufactured from petroleum hydrocarbons, however, typically have low carbon isotope ratios ($\delta^{13}C^1$) relative to other subsurface carbon sources. In areas contaminated with petroleum hydrocarbons, several researchers have noted shifts towards lower $\delta^{13}C$ values for soil gas CO_2 and/or groundwater DIC in the vicinity of the contamination (Aggarwal and Hinchee, 1991; Ostendorf and Kampbell, 1991) which have been attributed to aerobic metabolism of hydrocarbons.

The utility of stable isotope data is limited, however, by a lack of knowledge about the effects of bacterial metabolic activity on the stable isotopic compositions of substrates and byproducts. Most physical, chemical, or biologic processes cause shifts in the isotopic compositions of the materials. The magnitudes of these fractionation effects for processes such as

---

[1] Stable isotope ratios are reported relative to internationally-accepted reference materials (Vienna PeeDee Belemnite or VPDB for carbon, Vienna Standard Mean Ocean Water or VSMOW for hydrogen). The ratios are given using the per mil notation, where (for carbon):

$$\delta^{13}C_{VPDB} = \left(\frac{\left(^{13}C / _{12}C\right)_{sample} - \left(^{13}C / _{12}C\right)_{VPDB}}{\left(^{13}C / _{12}C\right)_{VPDB}} \right) \times 1000$$

8.5 Isotope Studies

carbonate dissolution or plant respiration have been carefully determined by researchers working in other fields (i.e., botany, oceanography). The importance of microbial processes in natural systems has only recently been realized, and, as a result, little work has been done in this area. Without understanding the fractionation effects caused by microbial metabolic processes, especially in areas where strongly fractionating processes such as methanogenesis are occurring (Conrad et al., 1995; Revesz et al., 1995; Landmeyer et al., 1996), it will not be possible to use isotope data to quantify contributions to soil gas CO_2 or groundwater DIC isotopic signatures derived from microbial metabolism of contaminants.

As part of this project, we will be tracking the isotope ratios of contaminants and metabolic byproducts during the laboratory experiments. The purpose of this work is to determine the magnitude of fractionation effects caused by microbial activity observed during the experiments. These data will be compared to measurements of field samples collected from the TAN-33 drill hole (the site where the rock samples for the geocosm studies were collected). In anticipation of this work, a method for analyzing the isotope ratios of the contaminants has been developed and the isotopic ratios of some of the compounds to be used were measured. In addition, a series of experiments to determine the effects on the isotope ratios of the compounds resulting from physical processes such as volatilization and dissolution in water have been started.

8.5.1 Determination of isotope ratios of potential substrates

Analyses were made of the isotope ratios of five compounds that will be used for this project (Table 8.5.1). Measured amounts of the compound to be analyzed (2-4 µl, depending on the expected yield of CO_2) were injected into an evacuated vaporization chamber on a vacuum line. The gas was then passed through a CuO furnace at 900°C in order to oxidize the sample. CO_2 from this reaction was trapped cryogenically and the yield measured using a pressure transducer.

H_2O was trapped in a glass tube with Zn metal and reacted at 500°C to produce H_2 gas (following the method outlined by Venneman and O'Neil, 1993). The hydrogen and carbon isotope ratios of the gases were analyzed using the VG Prism Series II isotope ratio mass spectrometer at the Center for Isotope Geochemistry at LBNL. Each compound was analyzed two or three times. The isotope ratios of replicate analyses were within ±0.2‰ for $\delta^{13}C$ and ±5‰ for δD.

Three hydrocarbon compounds were analyzed. The carbon and hydrogen isotope ratios of these compounds were within the range of values typical for petroleum hydrocarbon compounds (Deines, 1980). The carbon isotope ratios of two chlorinated compounds were also analyzed. These had significantly lower $\delta^{13}C$ values than the hydrocarbon compounds. Van Warmerdam et al. (1995) analyzed the carbon isotope ratios of PCE and found a range of $\delta^{13}C$ values between -23.2 and -37.2‰ (depending on the manufacturer). Our value for PCE falls within this range. The $\delta^{13}C$ value for carbon tetrachloride (-45.2‰) is somewhat lower than would be expected for compounds manufactured from petroleum hydrocarbons, but may be a reflection of the method used produce the carbon tetrachloride. The difference in the carbon isotope ratios of the hydrocarbon compounds and chlorinated compounds should make it possible to use differences in the carbon isotope ratios of degradation byproducts (e.g., CO_2, CH_4) to determine contributions from the different compounds in experiments with mixed substrates.

In addition to the five compounds discussed above, analyses of the $\delta^{13}C$ value of trichlorotrifluoroethane (Freon 113) were also attempted. Production of carbon-oxygen-fluorine compounds during combustion of these samples prevented accurate analyses of the carbon isotope ratios. Further work will be done to develop a suitable analytical method for fluorinated hydrocarbon compounds.

8.5 Isotope Studies

Table 8.5.1   Isotope compositions of potential substrates

Compound	Chemical Formula	$\delta^{13}C_{VPDB}$ (‰)	δD_{VSMOW} (‰)
1. Toluene	$C_6H_5CH_3$	-27.2	-82
2. Iso-Octane	$CH_3[CH_2]_6CH_3$	-27.9	-128
3. n-Dodecane	$CH_3[CH_2]_{10}CH_3$	-32.3	-76
4. Carbon tetrachloride	CCl_4	-45.2	-
5. Perchloroethylene (PCE)	$Cl_2C=CCl_2$	-35.9	-

8.5.2 Effects of physical processes on isotope ratios of substrates

Very little prior work has been done to determine the fractionating effects of physical processes (e.g., vaporization, dissolution in water) on the isotope ratios of the organic compounds that will be used for this project. Balabane and Létolle (1985) measured shifts in the δD and $\delta^{13}C$ values of three organic compounds (anethole, toluene and benzene) during volatilization and distillation of the compounds. They found that the δD and $\delta^{13}C$ ratios of the volatilized hydrocarbon compounds were significantly higher than the δD and $\delta^{13}C$ ratios of the liquid fraction. The method they used, however, consisted of volatilizing the liquid in a vacuum at elevated temperatures (100°C) and condensing the vapor phase in a distillation column (at ~5°C). As we will be working neither in a vacuum nor with such extreme temperature gradients, we designed some experiments to test whether similar isotopic fractionation effects would occur under the conditions in which we will be working (vaporization into air at room temperatures). These experiments are being carried out with both the pure phase and with the compound dissolved in water to test what fractionation effects, if any, result from dissolution and exsolution of the compounds from water.

8.5 Isotope Studies

Table 8.5.2 Data from toluene volatilization experiments (initial $\delta^{13}C$ of toluene = -27.2‰).

Starting conditions	Time (hrs)	Yield (μmoles CO_2 per 10 cc)	$\delta^{13}C_{VPDB}$ (‰)
1. Toluene in vacuum	0.5	31.9	-27.3
	2.0	101.0	-27.2
2. Toluene in CO_2-free air	1.0	8.8	-28.8
	2.5	12.0	-28.0
	16.7	67.5	-27.8
	90.0	129.4	-27.6
3. Toluene dissolved in water (initial concentration = 0.4%)	1.2	10.3	-28.2
	19.0	71.9	-27.9
4. Toluene dissolved in water (initial concentration = 0.1%)	17.0	14.0	-27.5

To date, experiments have been carried out with toluene (Table 8.5.2). In a vacuum, there is no measurable fractionation between the $\delta^{13}C$ ratio of the vapor phase and the liquid phase (even when the vapor phase is not yet saturated). In air, the toluene vapors have slightly lower $\delta^{13}C$ values (by ~0.5‰) than the liquid. The results for toluene dissolved in water are similar, however, there is not yet enough data to determine whether there is any difference or not. These results are preliminary, but they do indicate that the large shifts towards higher $\delta^{13}C$ values observed by Balabane and Létolle (1985) do not apply under these conditions.

9. Plans for FY97

In accordance with our original project proposal (Pruess and Hunter-Cevera, 1995), we plan to carry out the following tasks in FY97.

- Task 1.1 Continuation of phenomenological studies in abiotic systems

  Following our experiments with water seepage in a cast of a relatively smooth granite fracture conducted in FY96, we will perform similar experiments of LNAPL (n-dodecane) and DNAPL (CCl_4) to test for the differences of liquid density, viscosity and wettability on seepage patterns. Seepage of NAPL into a water-saturated fracture replica will also be studied, as well as the effect of vacuum venting on residual water and NAPL saturations.

- Task 1.2 Phenomenological flow studies in biotic system

  Efforts will focus on an open geocosm, which will allow the direct observation of flow behavior and the development of biological activity. Water, supplemented with soil extract is trickled over an inclined, open fracture surface under a transparent enclosure while the liquid distribution is photographically monitored. After the experiment, the fracture surface will undergo biological and mineralogical characterization. A NAPL contaminant will be introduced to observe its effect on flow and biological activity. The first experiment will be conducted with a dense basalt fracture sample. If successful, the design will be developed to allow sampling and analysis of the liquid and vapor phases to monitor biological activity.

- Task 2.1 Two-fluid phase flow dynamics experiments

  We will pursue options to obtain larger fracture samples from vesicular and dense basalt from INEL to fabricate 20 cm x 30 cm fracture casts, as well as working with the smaller samples from 3" diameter core that we obtained in FY96. This will provide us with a range of fracture geometries from relatively smooth to very rough which will allow us to test the variability of seepage behavior as a function of fracture geometry. Seepage of water, LNAPL and DNAPL into dry and water-saturated fractures will be studied for low and high angles of inclination and inlet pressures ranging from negative to positive. Similar studies will be conducted in glass plate cells of defined aperture sequences to investigate the parameters controlling non-steady flow behavior.

- Task 3.1 Test geocosm models

- Task 3.2 Effects of water content of rock on toluene and TCE biodegradation

9. Plans for FY97

- Task 3.3 Monitoring of biotic and abiotic transformations with isotopic ratios

  Within this task we will continue the measurement of isotopic fractionation effects caused by vaporization and dissolution of organic compounds, including making measurements of gas phase samples collected from Tasks 1.1 and 2.1. Methods for for monitoring samples collected from experiments in Task 3.2 will be developed and implemented. Soil gas and groundwater samples will be collected and analyzed from TAN-33 drillhole at the INEL.

- Task 4. Preliminary testing of conceptual models with data from Task 1

  Observations and data obtained from the Task 1 experiments will be interpreted and analysed, using basic concepts of multiphase fluid behavior in porous media. This involves an analysis of fluid distributions and flows, as governed by gravity, capillary and viscous forces, effects of surface tension pehnomena, and the geometric characterization of fracture apertures, wall roughness and matrix rock. Limited numerical simulation studies will be conducted to investigate flow mechanisms, and to explore stochastic behavior on different scales.

- Annual Report

10. Acknowledgment

11. Glossary

Acronyms

DNAPL	dense non-aqueous phase liquid
DoD	Department of Defense
DOE	Department of Energy
EPA	Environmental Protection Agency
ESRP	Eastern Snake River Plain
GCMS	gas chromatography mass spectrometer
INEL	Idaho National Engineering Laboratory
LANL	Los Alamos National Laboratory
LNAPL	light non-aqueous phase liquid
MDAL	Material Disposal Areal L
NAPL	non-aqueous phase liquid
OCVZ	Organic Chemicals in the Vadose Zone
PCE	perchloroethene
RWMC	Radioactive Waste management Complex
SDA	Surface Disposal Area
TAN	Test Area North
TCA	trichloroethane
TCE	trichloroethene
TSF	Technical Support Facility
USGS	United States Geological Society
VOC	volatile organic chemical
VVE	vacuum vapor extraction

11. Glossary

Symbols

A	cross-sectional area for flow
b	aperture
dt_{ave}	time between each snapping event
dt_{form}	time for thread formation
dt_{drain}	time for thread to drain into lower section
g	acceleration of gravity
h_w	elevation difference between point of atmospheric pressure in inlet reservoir and fracture inlet
K	saturated hydraulic conductivity
k	permeability
$k_{r,w}$	relative permeability of wetting phase
P_c	capillary pressure
P_{nw}	non-wetting phase pressure
P_w	water pressure
Q	flow rate
T	transmissivity
t	time
V	volume
w_t	thread width at top of middle section
Z_1	elevation of atmospheric pressure in inlet reservoir
Z_2	elevation of fracture inlet
$\delta^{13}C$	ratio of ^{13}C to ^{12}C in per mil notation (see footnote 1 in section 8.5)
ϕ	fracture inclination
φ	specific moisture content
λ	scaling factor
μ	viscosity
θ	contact angle
ρ	fluid density
σ	surface tension
ζ	permeability modifier

12. References

Aggarwal, P. K. and R. E. Hinchee., Monitoring in situ biodegradation of hydrocarbons using stable carbon isotopes, *Environ. Sci. Tech.*, 25, 1178-1180, 1991.

Amy, P.S., Haldeman, D. L., Ringelberg, D., Hall, D. H., and Russell, C., Comparison of identification systems for bacteria isolated from water and endolithic habitats within deep subsurface, *Appl. Environ. Microbiol.* 58, 3367-3373, 1992.

Balabane, M. and R. Létolle, Inverse overall isotope fractionation effect through distillation of some aromatic molecules (anethole, benzene and toluene), *Chem. Geol.* 52, 391-396, 1985.

Blunt, M., D. Zhou and D. Fenwick, Three phase flow and gravity drainage in porous media, submitted to *Transport in Porous Media*, May, 1994.

Bradford, S. A. and F. J. Leij, Fractional wettability effects on two-and three-fluid capillary pressure-saturation relations, *Journal of Contaminant Hydrology*, 20, 89-109, 1995a.

Cerniglia, C. E., Microbial transformation of aromatic hydrocarbons. In *Petroleum microbiology,* Ed. R. M. Atlas, Macmillan publishing company, 99-128, 1984.

Colwell, F.S., G. J. Stormberg, T. J. Phelps, S.A. Birnbaum, J. Mckinley, S.A. Rawson, C. Veverka, S. Goodwin, P.E. Long, B.F. Russell, T. Garland, D. Thompson, P. Skinner, and S. Grover, Innovative techniques for collection of saturated and unsaturated subsurface basalts and sediments for microbiological characterization. *J. of Microbiological Methods*, 15:279-292, 1992.

Conrad, M.E., P.F. Daley, M.F. Fischer, B.B. Buchanan, T. Leighton and M. Kashgarian, Carbon isotope evidence for intrinsic bioremediation of petroleum hydrocarbons, *LBNL Report 37989*, 1995.

Costerton, J. W., Overview of microbial biofilms, *J. Ind. Microbiol.*, 15, 137-140, 1995.

Deines, P., The isotopic composition of reduced organic carbon, in *Handbook of Environmental Geochemistry VI,* ed. by Fritz, P. and J.-Ch fontes, 329-406, Elsevier, Amsterdam, 1980.

Dullien, F. A. L., Two-phase flow in porous media, *Chem. Eng. Technol.,* Vol. 11, 407-424, 1988.

Faybishenko, B. A., Earth Sciences Division, E. O. Lawrence Berkeley National Laboratory, personnal communication, 1996.

12. References

Geller, J. and K. Pruess. On Water Infiltration in Rough-Walled Fractures. Proceedings, Sixth Annual International High-Level Radioactive Waste Management Conference, Las Vegas, NV, pp. 23 - 25, American Nuclear Society, La Grange Park, IL, May 1995.

Geller, J. T., G. Su and K. Pruess, Preliminary Studies of Water Seepage Through Rough-Walled Fractures, Earnest Orlando Lawrence Berkeley National Laboratory, Berkeley, California, Report No. LBNL-38810, July, 1996.

Gentier, S. Morphologie et Comportement Hydromecanique d'une Fracture Naturelle Dans un Granite sous Contrainte Normale, Doctoral Thesis, Universite d'Orleans, 1986.

Glass R. J. and Nicholl M. J., Quantitative Visualization of Entrapped Phase Dissolution Within a Horizontal Flowing Fracture, *Geophysical Research Letters*, 22, No. 11, 1413-1416, 1995.

Henry, S.M. and D. Grbic-Galic, Biodegradation of trichlorothylene in methanotrophic systems and implications fro process applications. In *Biological degradation and bioremediation of toxic chemicals*, Ed. G.R. Chaudhry, Dioscorides Press, Portland, Oregon, 314-344, 1994.

Herrick, J.B., Madsen, E.L, Batt, C.A. and Ghiorse, W. C., Polymerase Chain Reaction Amplification Of Naphthalene-Catabolic And 16s, Rrna Gene Sequences From Indigenous Sediment Bacteria, *Applied And Environmental Microbiology*, 59 , No. 3, pp. 687-694,1993.

Hirsch, P., Eckhardt F.E.W. and R.J. Palmer Jr., Methods for the study of rock-inhabiting microorganisms - A mini review. *J. Microb. methods*, 23: 143-167, 1995.

Knutson, C. F., K. A. McCormick, R. P. Smith, W. R. Hackett, J. P. O'Brien and J.C. Crocker, FY89 Report: RWMC Vadose Zone Basalt Characterization, Informal Report EGG-WM-8949, 1990.

Landmeyer, J.E., D.A. Vroblesky and F.H. Chapelle, Stable carbon isotope evidence of biodegradation zonation in a shallow jet-fuel contaminated aquifer. *Environ. Sci. Tech.*, 30, 1120-1128, 1996.

Leverett, M. C., Capillary Behavior in Porous Solids, *Trans. Soc. Pet. Eng. AIME*, 142, 152-169, 1941.

Lodman, D., S. Dunstan, W. Downs, J. Sondrup, D. Miyasaki, K. Galloway and K. Izbicki, Treatability Study Report for the Organic Contamination inthe Vadose Zone, OU 7-08, Idaho National Engineering Laboratory, EG&G Idaho, Inc., Idaho Falls, Idaho, Report No. EGG-ER-11121, May, 1994.

12. References

Long, J. C. S., C. Doughty and B. Faybishenko, Analog Site for Fracture Rock Characterization, Annual Report FY 1995, E. O. Lawrence Berkeley National Laboratory, Berkeley California, LBL-38095, October 1995.

Miller, E.E. and R.D. Miller, Physical Theory for Capillary Flow Phenomena, *J. Appl. Phys.*, Vol. 27, No. 4, pp. 324 - 332, 1956.

Nicholl, M. J., R. J. Glass, and S. W. Wheatcraft, Gravity-driven infiltration instability in initially dry nonhorizontal fractures, *Water Resour. Res., 30*, No. 9, pp. 2533-2546, 1994.

Ostendorf, D. W. and D. H. Kampbell, Biodegradation of hydrocarbon vapors in the unsaturated zone, *Water Resources Res.*, 27, 453-462, 1991.

Paul, E. A. and F. E. Clark, *Soil Microbiology and Biochemistry*, Academic Press, Inc., 275pp., 1989.

Pedersen K., The Deep Subterranean Biosphere, *Earth-Science Reviews, 34*, No. 4, pp. 243-260, 1993.

Persoff, P. and K. Pruess, Two-phase flow visualization and relative permeability measurement in natural rough-walled rock fractures, *Water Resour. Res., 31*, 1175-1186, 1995a.

Persoff, P. and K. Pruess, Two-Phase Flow Experiments in Natural Rock Fractures from Yucca Mountain, LBL -37716, September, 1995b.

Persoff, P. and Pruess, K., Flow visualization and relative permeability measurements in rough-walled fractures, in *Proceedings of the Fourth International High-Level Radioactive Waste Management Conference*, Las Vegas, Nevada, April 26-30, 1993, vol. 2, pp. 2007-2019, American Society of Civil Engineers, New York, 1993.

Pruess, K., Analysis of flow processes during TCE infiltration in heterogeneous soils at the Savannah River site, Aiken, South Carolina, LBL-32418, June 1992.

Pruess, K. TOUGH2 - A General Purpose Numerical Simulator for Multiphase Fluid and Heat Flow, Report No. LBL-29400, Lawrence Berkeley Laboratory, Berkeley, CA, May 1991.

Pruess, K. Numerical Simulation Experiments on Water Seepage in Heterogeneous, Unsaturated Rock Fractures. Lawrence Berkeley National Laboratory Report LBL-38883, submitted to *J. Contam. Hydrology*, May 1996a.

Pruess, K. Effective Parameters, Effective Processes: From Porous Flow Physics to In Situ Remediation Technology. in: H. Kobus, B. Barczewski, H.P. Koschitzky (eds.), *Groundwater and Subsurface Remediation,* Springer, Berlin, Heidelberg, New York, pp. 183 - 193, 1996b.

12. References

Pruess, K., and Y. W. Tsang. On Two-Phase Relative Permeability and Capillary Pressure of Rough-Walled Rock Fractures, *Water Resour. Res.*, Vol. 26, No. 9, pp. 1915-1926, September 1990.

Record of Decision, Declaration for the Technical Support Facility Injection Well (TSF-05) and Surrounding Groundwater Contamination (TSF-23) and Miscellaneous No Action Sites Final Remediation Action, Operable Unit 1-07B, Waste Area Group 1, Idaho National Engineering Laboratory, Idaho Falls, Idaho, August 4, 1995.

Revesz, K., T. B. Coplen, M. J. Baedecker and P. D. Glynn, Methane production and consumption monitored by stable H and C isotope ratios at a crude oil spill site, Bemidji, Minnesota, *App. Geochem.*, 10, 505-516, 1995.

Rodriguez G.G., Phipps D., Ishiguro K. and H. F. Ridgway, Use of a fluorescent redox probe for direct visualization of actively respiring bacteria. *Appl. Environ. Microbiol.* 58(6): 1801-1807, 1992.

Sorenson, Jr., K. S., A. H. Wylie and T. R. Wood, Test Area North Hydrogeologic Studies Test Plan Operable Unit 1-07B, Idaho National Engineering Laboratory, Report No. INEL-96/0105, March, 1996.

Staley, J.T., *Prosthecomicrobium* and *Ancalomicrobium:* new prosthecate freshwater bacteria. *J. Bacteriol.* 95: 1921-1942, 1968.

Su, G., Water infiltration and intermittent flow in rough-walled fractures, M.S. Thesis, University of California at Berkeley, May 1995.

Van Warmerdam, E.M., S.K. Frape, R. Aravena, R.J. Drimmie, H. Flatt, and J.A. Cherry, Stable chlorine and carbon isotope measurements of selected chlorinated organic solvents, *App. Geochem. 10*, 547-552, 1995.

Venneman, T.W. and J.R. O'Neil, A simple and inexpensive method of hydrogen isotope and water analyses of minerals and rocks based on zinc reagent, *Chem. Geol. 103*, 227-234, 1993.

Vogel, T. M., Natural bioremediation of chlorinated solvents, in: *Handbook of bioremediation,* pp.201-225, Lewis Publishers, Boca Raton, Florida. 1994.

Weirich, G., and R. Schweisfurth, Extraction and culture of microorganisms from rock. *Geomicrobiol. J.* 4:1-20, 1985.

Appendix A. Sample Acquisition Report

William T. Stringfellow
Renaissance Consulting Group
1008 The Alameda
Berkeley, CA 94707

Phone: (510) 528-6792   **Fax: (510) 528-7159**

To: Jill Geller and Hoi-Ying Holman,
From: William Stringfellow
Subject: INEL sampling trip.
Date: October 24, 1996
cc: J. Hunter-Ceverra

Drilling at the Test Area North site was conducted using Reich T-650-W drilling rig. A well was drilled to 200 feet and then cores of vadose zone rock were collected between 200 and 225 feet, where the water table began.

The first core was collected on October 9, 1996. This sample was not collected using aseptic techniques.. The top of this core was at 200 feet. The bottom 4 feet of core was lost (sedimentary interbed) and 2.8 feet of rock was recovered. This core was turned over to Jill Geller on October 10, 1996.

Aseptic cores were collected on the afternoon of October 15, 1996 using sterile split core sampler and immediately placed in an argon atmosphere. Aseptic cores were collected using microsphere tracers for sample integrity analysis. In this technique, microspheres (Fluoresbrite™ Carboxylate YG 1.0 micron Microspheres, Lot 465662, diameter 0.923 microns ± 0.028, Polysciences Inc., Warrington, PA) are put in a plastic bag and mounted at the bottom of the split sampler. As the drill enters the core, the bag breaks and the microspheres are distributed down the core as the drill enters the rock. I arrived on the site and processed the samples the following day. Intact core sections were transferred using aseptic technique into autoclaved anaerobe bags inside a glove bag containing an argon atmosphere. Only core section 5 was too large to fit in one bag. This core was split using an hydraulic press into two sections (section 5-A and 5-B). All intact core sections recovered from the 218 to 223 foot and 213.5 to 218 foot cores were collected.

Additionally, intact core sections were also collected from 209 feet and 212.5 feet (in the vadose zone) and approximately 258 feet (in the aquifer). These cores were not collected using aseptic techniques, but I thought they would be of use for studies where native bacteria were not of concern. There core were also placed in anaerobe bags for protection, but were not gassed with argon.

Samples were double bagged, packed in ammunition cans, and placed in coolers for transport. Samples were refrigerated or iced before and during transport.

Attached are drilling logs for the hole from which your samples were collected. Core samples are marked in the log as LBNL # 1-9. I have also attached the following information that has been requested by Jennie and Hoi-Ying:

1)   Procedure for analysis of microspheres.

2)   Some water quality data from water drawn from under the site. This data was taken from environmental reports INEL-95/0255(95) and EGG-2679(93).

134

The samples are identified as follows:

Sample Number	Approximate Depth at Top of Core Section (feet)	Collection procedure
1	221.5	aseptic, microspheres
2	219.8	aseptic, microspheres
3	218.0	aseptic, microspheres
4	217.5	aseptic, microspheres
5-A	215.5	aseptic, microspheres
5-B	216.5	aseptic, microspheres
6	213.5	aseptic, microspheres
7 (saturated zone)	between 258 to 263	not aseptic
8	212.5	not aseptic
9	209.0	not aseptic

FORM EG&G-3025
Rev 25-88?

DRILLING CORE LOG

Date: 09 OCT 96 / 14 OCT 96

Geologist: C. F. Hegley

Core Length: 2.8 + 2.7 = 5.5 (ft.)

Borehole: TAN-33

Sample No.:

Cored Interval: 200 3.24 ___ To

204 3.75 Bottom

Depth Below Land Surface (ft.)	Core Diagram	Description
200–207 (diagram)	Lost core (sediment) Fracture Lost core (sediment)	200-201.4 - Gray aphanitic vesicular basalt, vesicled range from 1mm to 5 cm. 201.4 to 202.8 - vesicles decrease in size and number. TAN silty sand on the base of the core. 204-207.5 - Dense gray phaneritic basalt, clay in fractures. Rubble at 207-207.5. lost ≈1' of core

Remarks: _____

To: Will Stringfellow
510-642-7483
5 pages
From: Kick Colwell

FORM EG&G-3025
Rev 09-88!

DRILLING CORE LOG

Date: 10/15/96

Geologist: T. Woosley

Core Length: 5 _____ (ft.)

Borehole: Jan-33

Sample No.: _____

Cored Interval: 207.5 _____ Top

212.5 _____ Bottom

Depth Below Land Surface (ft.)	Core Diagram	Description
207.5 208 209 210 211 212 Lost	LBC #8	Massive gray aphanitic Basalt w/ clay filled fractures Fractured massive gray basalt w/ clay filled fractures and occasional vesicles ranging from 1mm-1cm. 212.0-212.5 ft lost

Remarks: radcon surveyed clean

JCAM E3&G-JC26
Rev 05-88

DRILLING CORE LOG

Date: __10/15/96__

Geologist: __T. Woosley__

Core Length: __1.0__ _____(ft.)

Borehole: __Jun-33__

Sample No : _____

Cored Interval: __212.5__ _____Top

__213.5__ _____Bottom

Depth Below Land Surface (ft.)	Core Diagram	Description
212.5 213	LBC #3	Highly Fractured Dark Gray Vesicular Basalt w/ clay filled fractures

Remarks: __Radcon surveyed clean__

FORM EG&G-0026
Rev. 05-681

DRILLING CORE LOG

Date: 10/15/96

Geologist: T. Woosley

Core Length: 4.5   (ft.)

Borehole: Tan-33

Sample No.:

Cored Interval: 213.5 _____ Top
                218.0 _____ Bottom

Depth Below Land Surface (ft.)	Core Diagram	Description
215.5	⊂BC #6	Highly Fractured Vesicular gray basalt w/ clay fill in fractures
214		215.5 Red silty, sandy thin welded interbed (1 inch thick)
215		
216	⊂BC 5A	
217	⊂BC 5B	217.2 - 217.3 Brown Silty Clay interbed (1 inch thick)
	⊂BC #4	217.9 - 218.0 Tan welded ash bed (1 inch thick) w/ reddish silty clay thinly spread over bottom of core piece
218		

Remarks: Radcon surveyed clean

FORM EG&G-3326
Rev 05-981

DRILLING CORE LOG

Date: __10/15/96 - 16 Oct 96__

Geologist: __T. Woosley__

Core Length: __5 + 0_____ (ft.)

Borehole: __Tan-33__

Sample No.: _____

Cored Interval: __218.0 / 223__
__223.0 / 228__ Bott

Depth Below Land Surface (ft.)	Core Diagram	Description
218	LBC Sample #3	218.7-219.7 loss of interbed material
219	Loss	Red Silty Sand interbed
220	LBC #2	Gray vesicular basalt
		219.6-220.3 loss of interbed material (new 10/15/96)
		220.6-221.3 loss of interbed material
221	Loss	Red Silty Sand interbed
222	.5 = LBC #1	Gray vesicular aphanitic porphyritic basalt w/ clay filled fractures.
223		223-228 - no core recovered.
LOST CORE (sand)		sand (very fine, tan unconsolidated) on the bit

Remarks: __Radcon survey clean__

__LBC - Lawrence Berkley lab samples c/o Will Stringfellow__

140

MICROSPHERE ANALYSIS PROCEDURE (Rev 1)

1. Obtain a sample of core (1 g) or a sample labeled "microspheres" or "tracers" and place in a test tube with an equivalent amount (by wt) of 0.1% sodium pyrophosphate, resulting in a 1:2 solution.

2. Vigorously vortex the solution for 2 min, then let it settle for 2 min. Be consistent in the manner that you use to vortex the sample.

3. Etch three 1 cm^2 circles onto a glass slide and label the slide with the appropriate sample number and dilution. Pipette 10 µl of the supernatant (partially clarified liquid at the top) from the tube to each of the three 1 cm^2 circles on the slide. Spread the slurry within each of the circles and allow the smears to air dry. Hasten drying by placing the slide in a warm spot.

4. View the slides under epiillumination using a 40x objective and 10x ocular using a filter set that maximizes observation of YG microspheres. Count the number of microspheres in each of the 1 cm^2 circles (replicates of each other) and record data.

5. If the smear contains too many microspheres to count easily, then estimate the number in a single field of view and then dilute the original slurry (be sure to remix the original slurry in the first step of the dilution) to an appropriate degree such that you will count about 200-300 microspheres in each circle. Repeat steps 2, 3 and 4 with the diluted sample.

6. If too few microspheres are present, after we discuss this, you will want to concentrate the microspheres in the original sample to estimate the number of microspheres per g. Remove as much of the original slurry as possible without collecting sediment from the bottom. Record this amount and place in a centrifuge tube. Balance the centrifuge with another tube that weighs the same as the sample and then centrifuge for 15 minutes. Pipette off as much of the supernatant as possible (record this amount) without disturbing the pellet and vortex the remaining liquid in the tube so that it resuspends the pellet of microspheres and sediment. Repeat steps 3 and 4. This slide should contain a higher number of microspheres as they have been concentrated.

7. Calculations for determining the number of spheres/g of rock:

spheres/g = # spheres counted/cm^2 x 1.0 cm^2/0.01 ml x 1/dilution of original rock

Example: You count 10 microspheres within one 1 cm2 circle. One g of original rocks was mixed with 1.0 ml of 0.1% sodium pyrophosphate.

10 spheres/cm^2 x 1.0 cm^2/0.01 ml x 2 ml total vol/1 g = 2000 spheres/g

Checklist:
- Be sure that you are using the correct filter set for the counts.
- Be certain that you're using the 40x objective lens.
- Dilutions of the original rock in sodium pyrophosphate: if added 1 g of rock to 1 ml of sodium pyrophosphate then you diluted the original rock by 0.5, so you need to multiply by 2 to get the correct concentration of spheres in the original rock sample. In all cases take extra care in recording all dilutions or concentrations of the original sample so that the actual concentration of microspheres within the original sample can be calculated.
- Be sure fluorescence is working (use a test slide with spheres on it).

141

Table C-2. Detected nonradiological parameter results of the 1995 sampling.

Location	Parameter	Results (mg/L)	Flag	MCL/SMCL (mg/L)
CFA Distribution System	Alkalinity	120.00		NA
	Bicarbonate	150.00		NA
	Langlier Index	-0.140		NA
	Nitrogen, Nitrate-Nitrite	3.00		10
	Nitrogen, as Nitrate	3.00		10
	TDS	420.00	R[a]	500
	pH	7.60	R	6.5-8.5
	Calcium	68.00		NA
	Iron	0.110		0.3
	Sodium	18.00		20
	Zinc	0.016		5
	Trichloroethylene	0.001		0.005
	Total Trihalomethanes (TTHM)	0.003		0.100
CFA Well #2	Trichloroethylene	0.001		0.005
CPP Distribution System	Alkalinity	80.00		NA
	Bicarbonate	97.00		NA
	Langlier Index	-0.180		NA
	Nitrogen, Nitrate-Nitrite	1.20		10
	Nitrogen, as Nitrate	1.20		10
	TDS	250.00		500
	pH	8.00		6.5-8.5
	Calcium	56.00		NA
	Iron	0.060		0.3
	Sodium	8.00		20
	Total Trihalomethanes (TTHM)	0.001		0.100
EBR-I Distribution System, EBR-601	Nitrogen, Nitrate-Nitrite	0.370		10
	Nitrogen, as Nitrate	0.370		10
	p-Dichlorobenzene	0.002		0.075
Gun Range Distribution System	Nitrogen, Nitrate-Nitrite	1.10		10
	Nitrate/Nitrite as N	1.10		10
Main Gate Distribution System, B27-603	1,1,1-Trichloroethane	0.0009		0.200
	Nitrogen as Nitrate	0.710		10
	Nitrogen, Nitrate-Nitrite	0.710		10
PBF Distribution System	Alkalinity	140.00		NA
	Bicarbonate	160.00		NA
	Langlier Index	0.380		NA
	Nitrogen, Nitrate-Nitrite	2.10		10
	Nitrogen, as Nitrate	2.10		10
	TDS	260.00		500
	pH	8.10		6.5-8.5
	Calcium	40.00		NA
	Iron	0.090		0.3
	Sodium	15.00		20
	Zinc	0.006		5
	Ethylbenzene	0.005		0.700
	Xylenes (total)	0.017		10.00
RWMC #1 Well, WMF-603	1,1,1-Trichloroethane	0.0006		0.200
	Carbon tetrachloride	0.004		0.005
	Trichloroethylene	0.001		0.005

Table C-2. (continued).

Location	Parameter	Results (mg/L)	Flag	MCL/SMCL (mg/L)
RWMC Distribution System, WMF-604	Alkalinity	140.00		NA
	Bicarbonate	170.00		NA
	Hardness (as $CaCO_3$)	120.00		NA
	Langlier Index	0.360		NA
	Nitrogen, Nitrate-Nitrite	0.740		10
	Nitrogen, as Nitrate	0.740		10
	TDS	220.00		500
	pH	7.90		6.5-8.5
	Calcium	46.00		NA
	Iron	0.030		0.3
	Sodium	8.10		20
	Zinc	0.061		5
	Carbon Tetrachloride	0.002		0.005
	Trichloroethylene	0.0009		0.005
TAN/CTF Distribution System, TAN-614	Alkalinity	140.00		NA
	Bicarbonate	170.00		NA
	Nitrogen, Nitrate-Nitrite	0.700		10
	Nitrogen, as Nitrate	0.700		10
	TDS	250.00		500
	pH	8.0		6.5-8.5
	Calcium	51.00		NA
	Iron	0.020		0.3
TAN/TSF #1 Well, TAN-612	Tetrachloroethylene	0.002		0.005
	Trichloroethylene	0.010		0.005
TAN/TSF #2 Well, TAN-613	Tetrachloroethylene	0.0006		0.005
	Trichloroethylene	0.002		0.005
TAN/TSF Distribution System	Alkalinity	160.00		NA
	Bicarbonate	190.00		NA
	Nitrogen, Nitrate-Nitrite	0.940		10
	Nitrogen, as Nitrate	0.940		10
	TDS	240.00		500
	pH	8.20		6.5-8.5
	Calcium	53.00		NA
	Sodium	6.80		20
	Zinc	0.010		5
	Tetrachloroethylene	0.0008		0.005
	Trichloroethylene	0.0028		0.005
TRA Distribution System	Alkalinity	180.00		NA
	Bicarbonate	220.00		NA
	Hardness (as $CaCO_3$)	130.00		NA
	Langlier Index	0.110		NA
	Nitrogen, Nitrate-Nitrite	1.10		10
	Nitrogen, as Nitrate	1.10		10
	TDS	220.00		500
	pH	8.80		6.5-8.5
	Calcium	52.00		NA
	Sodium	8.60		20
	Zinc	0.023		5

a. The result shown was failed during validation.

Table 3. (continued).

Well	Month Sampled	Specific Conductance µS/cm	Concentration (mg/L)	
			Cl⁻	Na⁺
RWMC Production Well	January	360	16	—
	February	360	—	—
	March	362	—	—
	April	360	15	—
	May	371	—	—
	June	370	—	—
	July	368	14	—
	August	371	—	—
	September	369	—	—
	October	370	14	8.5
	November	373	—	—
	December	373	—	—
92 perched	April	1080	89	—
Natural background[a] (of aquifer)	—	300–325	8–15	10

a. J. R. Pittman et al., *Hydrologic Conditions at the Idaho National Engineering Laboratory*, Idaho, 1982–1985 update, 89–4008, 1988.

— No sample taken

During October of 1993, analyses for stable Na–22 were performed (see Table 3). Water from some of the RWMC monitoring wells contained sodium concentrations higher than the background level of 10 mg/L. Sodium concentrations have fluctuated in water from these wells. One possible cause for these fluctuations is the method used to construct the wells. During construction, the wells were pressure–concreted to prevent water from cascading from perched zones down to the SRPA. The cement could contribute to higher sodium concentrations.

The chloride concentration (see Table 3) was above background levels also but well below the chloride secondary maximum contaminant level (MCL), which is 250 mg/L. These concentrations may be from the same process described for sodium. Both the chloride and sodium concentrations are comparable to previous concentrations of past years at these well locations.

Approximately 334,594 L of organic waste were disposed prior to 1970 at the RWMC.[20] These buried wastes included about 92,354 L of carbon tetrachloride, 147,615 L of lubricating oil, and about 94,625 L of other organic compounds, including trichloroethane, trichloroethylene, perchloroethylene, toluene, and benzene.